Atomistic simulations of materials: Methods for accurate potentials and realistic time scales

Thesis by

Pratyush Tiwary

In Partial Fulfillment of the Requirements

for the Degree of

Doctor of Philosophy

California Institute of Technology

Pasadena, California

2012

(Defended May 4, 2012)

Dedicated to my dearest *Nana-nani*, who never stopped believing in me

Acknowledgments

This thesis has been possible only because of friends, teachers, and mentors, and I would like to thank them. Firstly, my adviser Axel van de Walle who gave me the chance to come to this institution of my dreams. Then through the years, he stayed patient with me through my follies and taught me how to convert knowledge into useful algorithms.

My thesis committee members Professors Brent Fultz, Bill Goddard, Julia Greer, and Bill Johnson are to be thanked for carefully reading through this thesis, and also for being excellent teachers. Julia especially has been an amazing mentor for me, helping me get into the exciting field of Nanomechanics.

To my professors from India, the ones who taught me almost everything I know: Professors Nasim Hoda, Swapan Ghosh, Dhananjai Pandey, TA Abinandanan, GVS Sastry, RK Mandal, NK Mukhopadhyay, BN Sarma, and Ravi Aggarwal: I hope this thesis and the rest of my career lives up to the faith you put in me.

Chris Weinberger and Andrew Jennings helped me identify problems in Nanomechanics. Chris also helped a lot with Chapter 6 in this thesis. Blas Uberuaga invited me to Los Alamos, which led to some of the most helpful and memorable discussions. I thank Professors Niels Grønbech-Jensen and Mark Asta for several great discussions and collaboration.

My labmates Steve, Greg, Chirru, Qijun, Ljuba and Ligen are some of the smartest people I have ever known. It's been a pleasure knowing you and learning things from you. I hope we collaborate in the future too.

Caltech staff are perhaps the coolest staff anywhere on this planet. They eliminated red tape and were always ready with a smile; they made my transition to

this new country so much more pleasant - especially Daniel and Laura at ISP, Greg, Athena, and Liz at the Y, and Rosie and Christy, at the APMS Department.

My two closest friends, Shahzada and Nisheeth, *I know that you'll love me, when there's no one left to blame.* And to so many more friends I made at Caltech, mostly through the common addiction of climbing and (with Patrick) a shared repulsion for brushing teeth every night - especially Patrick, Hamik, Nick, Marc, Stephen and Sean - thanks for taking me to the great outdoors, and for sharing a rope! Aron for introduced me to marathons. And my old roommates Jerry, Sawyer, and Manuj: We had some very fun times (and pranks).

My $Nana-Nani$, for the infinite love you gave and still give me, and for nourishing me when I lost my mother at age 5: I dedicate this thesis to you.

I thank my Father, for showing me that Math is not really optional.

And Megan, for being my best friend, and making me a happier person.

Abstract

This thesis deals with achieving more realistic atomistic simulations of materials, by developing accurate and robust force-fields, and algorithms for practical time scales.

I develop a formalism for generating interatomic potentials for simulating atomistic phenomena occurring at energy scales ranging from lattice vibrations to crystal defects to high-energy collisions. This is done by fitting against an extensive database of *ab initio* results, as well as to experimental measurements for mixed oxide nuclear fuels. The applicability of these interactions to a variety of mixed environments beyond the fitting domain is also assessed. The employed formalism makes these potentials applicable across all interatomic distances without the need for any ambiguous splining to the well-established short-range Ziegler-Biersack-Littmark universal pair potential. We expect these to be reliable potentials for carrying out damage simulations (and molecular dynamics simulations in general) in nuclear fuels of varying compositions for all relevant atomic collision energies.

A hybrid stochastic and deterministic algorithm is proposed that while maintaining fully atomistic resolution, allows one to achieve milliseconds and longer time scales for several thousands of atoms. The method exploits the rare event nature of the dynamics like other such methods, but goes beyond them by (i) not having to pick a scheme for biasing the energy landscape, (ii) providing control on the accuracy of the boosted time scale, (iii) not assuming any harmonic transition state theory (HTST), and (iv) not having to identify collective coordinates or interesting degrees of freedom.

The method is validated by calculating diffusion constants for vacancy-mediated diffusion in iron metal at low temperatures, and comparing against brute-force high-temperature molecular dynamics. We also calculate diffusion constants for vacancy diffusion in tantalum metal, where we compare against low-temperature HTST as well. The robustness of the algorithm with respect to the only free parameter it involves is ascertained.

The method is then applied to perform tensile tests on gold nanopillars on strain rates as low as $10^2/s$, bringing out the perils of high strain-rate molecular dynamics calculations. We also calculate temperature and stress dependence of activation free energy for surface nucleation of dislocations in pristine gold nanopillars under realistic loads. While maintaining fully atomistic resolution, we reach the fraction-of-a-second time scale regime. It is found that the activation free energy depends significantly and nonlinearly on the driving force (stress or strain) and temperature, leading to very high activation entropies for surface dislocation nucleation.

Contents

List of Figures

List of Tables

Chapter 1

Introduction

1.1 Why do atomistic simulations of materials?

Computer simulations have become increasingly popular and rather ubiquitous over the last few decades due to advances in computer power, memory and storage. However, the corresponding increase in experimental prowess has been no less striking. Experiments now have the capability to probe materials at the finest length scales, and even achieving femtosecond resolution in the timescale. It remains much easier, and will probably always stay so, to measure through experiments than through simulations the tensile strength of an iron rod, or the freezing point of a bucket of water. Thus, the question may be asked: Why do atomistic simulations of materials?

The answer is multifold. While it might be easy to measure the freezing point at 1 atmosphere pressure, it becomes prohibitively expensive to do so at high pressures. In contrast, a computer does not self-destruct if one asks it to measure the freezing point at 1000 atmospheres. Thus, simulations are useful when the conditions of interest are difficult to achieve in laboratory. Secondly, in atomistic simulations, one has essentially infinite control over the specific configuration and geometry of the material. Within a relatively short time, one can *synthesize* and study an endless number of materials with precisely tailored geometries and atomic arrangements, that would be difficult and expensive to make in the laboratory. Thirdly, simulations provide an easier and more direct way to study atomic mechanisms - in spite of the afore-

mentioned advance in resolution in length and time scales in experiments, observing individual atoms still remains by definition a trivial task in atomistic simulations.

To paraphrase Robert Cahn (*The Coming of Materials Science*, 2001), atomistic simulations are specifically suited for the intermediate scale between the territory of the classical mechanic (few atoms) and the statistical mechanic (on the order of Avogadro's number of atoms). By repeatedly solving classical equations of motion between each pair of particles, one studies the evolution of the system under an imposed set of conditions. One can observe individual atoms, yet make predictions about the collective behavior of a million or more atoms. Increasingly powerful parallel computers are allowing one to push the limit of system sizes that can be considered by breaking down the material into individual chunks that are treated on separate computers. All that remains to be done is to keep track of the interface atoms between these chunks - a task that is not trivial by any means but nevertheless achievable through raw computing power.

With the size of nanoscale devices coming down further and further, there is thus scope for much optimism - one can hope to do experiments and fully atomistic simulations on materials with same number of atoms! Alas, but this is not yet routinely possible.

1.2 Limitations of atomistic simulations

In the previous section, we mentioned the convergence of length scales between atomistic simulations and (nanoscale) materials science. In spite of this development, two features (or requirements) of atomistic simulations severely restrict their usefulness: (i) need for reliable and accurate interatomic potentials and (ii) small time-steps, leading to very short accessible time scales.

Atomistic simulations involve solving Newton's law of motions for pairs of parti-

cles interacting under a given force field. Ideally, they require no other parametric input. However, to borrow from a Computer Science parlance, "*Garbage In, Garbage Out*" applies well here. If the given interatomic potential or force-field is inaccurate, the accuracy of the entire simulation becomes highly questionable. This calls for developing robust, transferable and accurate potentials that capture the Physics or Chemistry of interest accurately.

The time scale problem arises because a typical atomistic simulation uses time steps on the order of 10^{-15} sec, needed to (a) correctly capture the highest frequency atomic vibrations and (b) preserve the accuracy of the numerical integration schemes in such algorithms. Unlike in the length scale problem, time is essentially sequential in nature and thus not as easily amenable to brute-force parallelization. Due to such small time-steps, atomistic simulations of even a few thousand atoms are limited to at best a few nanoseconds of total simulation time. This means, for instance, that for 10% deformation in a tensile test, the slowest strain-rate achievable in simulations is around $10^7 - 10^8/s$, while experiments rarely go faster than $10^3/s$. Similarly, if one is interested in studying glasses, the slowest quench rate achievable through simulations is around $10^{12}K/s$, while experiments rarely go faster than quench rates of $10^6K/s$.

1.3 Objectives of this thesis

This thesis pertains to solving both the problems mentioned in the previous section. We develop methods for designing accurate interatomic potentials and for achieving realistic time scales while still maintaining fully atomistic resolution. We now provide a brief summary of both efforts.

1.3.1 Interatomic potentials for nuclear fuels

In this thesis, we develop a methodology for generating interatomic potentials for use in classical molecular dynamics simulations of atomistic phenomena occurring at en-

ergy scales ranging from lattice vibrations to crystal defects to high-energy collisions. A rigorous method to objectively determine the shape of an interatomic potential over all length scales is introduced by building upon a charged-ion generalization of the well-known Ziegler-Biersack-Littmark universal potential that provides the short- and long-range limiting behavior of the potential. At intermediate ranges the potential is smoothly adjusted by fitting to *ab initio* data. This is done by fitting to accurate quantum mechanical data on equation of state, elastic constants, defect formation and migration energies and pathways. Where available, experimental data for high temperatures is also included in the fitting database. Our formalism provides a complete description of atomic interactions that can be used at any energy scale, and, thus, eliminates the inherent ambiguity of splining different potentials generated to study different kinds of atomic materials behavior. We exemplify the method by developing rigid-ion potentials for radiation damage in (U,Pu,Np)O_2 under conditions ranging from thermodynamic equilibrium to very high atomic-energy collisions relevant for fission events.

1.3.2 Fully atomistic hybrid algorithm for realistic time scales

We propose a hybrid deterministic and stochastic approach to achieve extended time scales in atomistic simulations that combines the strengths of molecular dynamics (MD) and Monte Carlo (MC) simulations in a novel and easy-to-implement way. The method exploits the rare event nature of the dynamics similar to most current accelerated MD approaches but goes beyond them by providing, without any further computational overhead, (a) rapid thermalization between infrequent events, thereby minimizing spurious correlations and (b) control over accuracy of time scale correction, while still providing similar or higher boosts in computational efficiency. We present two applications of the method: (a) vacancy-mediated diffusion in Fe and Ta yields correct diffusivities over a wide range of temperatures, thereby validating the method and (b) source-controlled plasticity and deformation behavior in Au nanopillars at realistic strain rates (up to 10^2/sec) with excellent agreement with previous

theoretical predictions and *in situ* high-resolution transmission electron microscopy (HRTEM) observations. The method gives several orders of magnitude improvement in computational efficiency relative to standard MD and good scalability with size of system.

We use the proposed algorithm to calculate temperature and stress dependence of activation free energy for surface nucleation of dislocations in pristine gold nanopillars under realistic loads. While maintaining fully atomistic resolution, we achieve the fraction of a second time scale regime. We find that the activation free energy depends significantly and nonlinearly on the driving force (stress or strain) and temperature, leading to very high activation entropies. We also perform compression tests on gold nanopillars for strain rates varying over 7 orders of magnitudes, reaching as low as $10^2/s$. Our calculations bring out the perils of high strain-rate molecular dynamics calculations: We find that while the failure mechanism for $\langle 001 \rangle$ compression of gold nanopillars remains the same across the entire strain-rate range, the elastic limit (defined as stress for nucleation of the first dislocation) depends significantly on the strain-rate. We also propose a new methodology that overcomes some of the limits in our original accelerated dynamics scheme (and accelerated dynamics methods in general). We lay out our methods in sufficient detail so as to be useful for understanding and predicting deformation mechanism under realistic driving forces for various problems.

We also look at vacancy diffusion in body-centered cubic tantalum under low temperatures (i.e. temperatures not directly inaccessible through MD simulations). We perform calculations of diffusion constant for vacancy-mediated diffusion using harmonic transition state theory, and through our method, and make a comparison of both. For this particular application, we explore in detail the sensitivity of our method to the choice of the only parameter that it involves.

Chapter 2

Ab Initio construction of interatomic potentials for uranium dioxide across all interatomic distances

2.1 Introduction

Molecular dynamics (MD) simulations provide a convenient tool for studying the behavior of large atomic ensembles, provided that the dynamics of interest is not of a duration that makes the simulation time impractical (an issue we address in detail in the later parts of this thesis). There are many examples of beautiful applications of how MD has been able to provide detailed insight into the dynamics and statistics of materials behavior. One contemporary interest is the field of high-energy radiation damage of crystalline materials, such as nuclear fuel. A core material of interest in this context is uranium dioxide, and one of the important aspects of the interest in this material is to understand the evolution and statistics of atomic displacement cascades due to high energy radiation [1]. Classical molecular dynamics is ideally suited for this kind of study since it strikes a fine balance between being coarse enough to simulate the spatial scale necessary to represent the extent of a damage cascade due to, e.g., a 100 MeV atomic collision, with being detailed enough to retain the atomic structure of the material. However, the complexity of the true interatomic interactions cannot be fully represented in an efficient manner by a simple classical functional form. Thus, one needs to develop a set of essential interaction features

that are necessary for a given application. This is a particularly challenging exercise for radiation damage simulations due to the disparate scales of energies involved. Therefore interatomic potentials suitable for this purpose are typically constructed by smoothly joining different types of interactions. At medium to long-range distances, a traditional potential (e.g., Buckingham, electrostatic etc.) fitted to a variety of thermodynamic and structural data is used. At short-ranges, accurate potentials are developed by fitting to *ab initio* data. The ZBL universal potential is one such very popular pair-potential developed by Ziegler *et al.* in the 1980's, as a generic function of the atomic numbers of the species involved [2]. Although each type of interaction is directly determined through fitting, the determination of a suitable spline that smoothly joins these two pieces is a highly non-unique process. Splining leads to an inherent ambiguity in the behavior of the complete potential, since the exact cutoff distances and the spline's algebraic form will have consequences for how large the "cores" of the atomic interactions are and how the potential features are in the region of transition. This, in turn, will have a significant impact on the ion trajectory and damage production one is ultimately interested in. Such ambiguity is illustrated in Figure 2.1.

In this chapter we introduce a rigorous method to unambiguously determine the form of the potential over all distances using *ab initio* data. Although our approach is applicable to any material system, we illustrate it using the important example of the nuclear fuel UO_2, which has been the focus of several detailed computational investigations, both through *ab initio* [4] and MD [5, 6] methods, due to its critical importance in the nuclear industry.

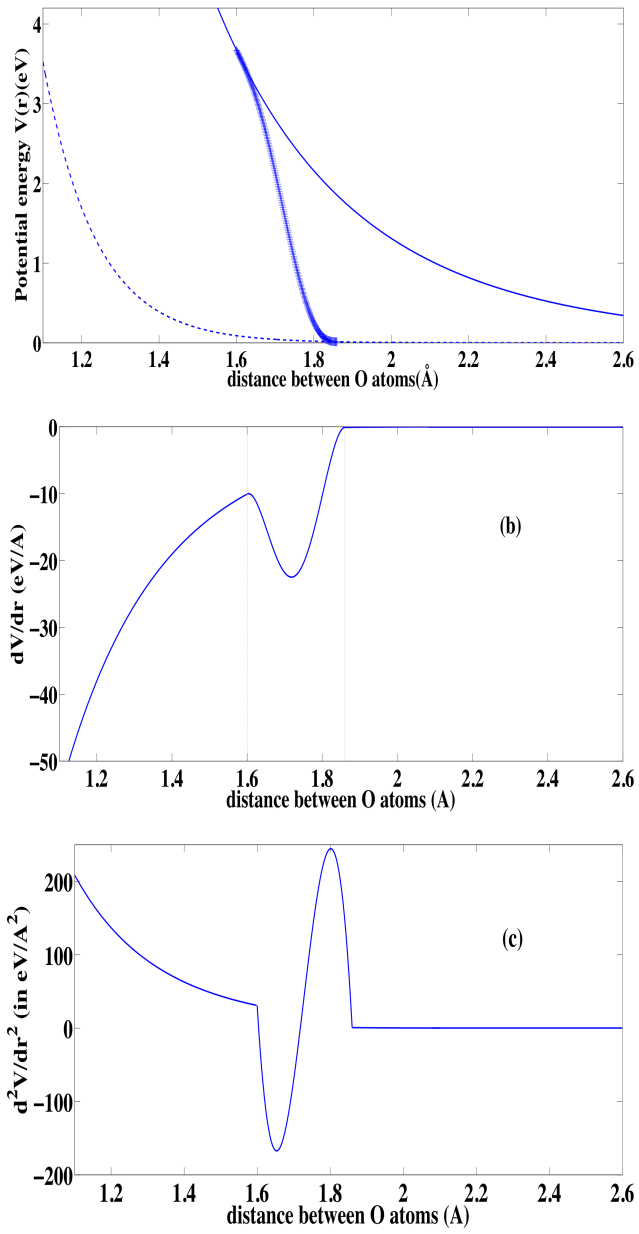

Figure 2.1: (a) ZBL screened potential (solid line) and the popular Morelon *et al.* potential (dashes) [3], joined together by a 5th order polynomial (open circles), for the case of two oxygen atoms. (b) First derivative of the net potential resulting from the same. (c) Second derivative of the potential. Since the spline was not fit to any data, one can not decide whether the resulting behavior in (b) and (c) is correct or spurious.

2.2 Interatomic potential form valid for all interatomic distances

Our approach is to first generalize the universal ZBL potential to include charged ions that behaves correctly in both short-range and long-range limits. This generalized potential smoothly interpolates between these two regimes over a physically-motivated length scale that is based on atomic orbital sizes instead of necessitating a user-specified transition radius for the electrostatic interactions at short ranges to prevent double-counting. The only component that remains to be determined by fitting is then the medium-range energy contribution associated with chemical bonding. As this contribution is only significant over a relatively small range of distances it is possible to introduce lower and upper cutoffs, where this contribution must smoothly vanish. Importantly, these physically motivated cutoffs can be fitted to *ab initio* data and are therefore no longer arbitrary; unlike in the current practice.

2.2.1 ZBL potential

The ZBL potential [2], which properly accounts for the screening of nuclear charge by the electronic clouds as a function of interatomic distances, is built on considering two interacting spherically symmetric rigid electron clouds. In this spirit, we also consider two interacting spherically symmetric rigid electron clouds with electron densities determined *ab initio* and fitted to a sum of Slater functions [7]. This approximation is valid beyond distances where electron clouds overlap and chemical bonds form. For short distances (i.e., distances less than chemical bond lengths) we obtain the energy as a function of distance between any two atoms through first order perturbation theory. It was demonstrated by Ziegler *et al.* that more sophisticated self-consistent field calculations incorporating the distortion of electronic clouds did not lead to any significant differences in the resulting interatomic potential at short distances [2]. Thus, since we employ the same electronic density and the same screening function (ratio of the actual atomic potential at some radius to the potential caused by an

unscreened nucleus) as used by Ziegler *et al.*, we recover the ZBL potential at these short distances, as we will show later.

2.2.2 Generalization of ZBL potential

We consider two spherically symmetric charge densities per unit volume $\rho_1(r)$ and $\rho_2(r)$, with central point charges of Z_1e and Z_2e respectively, $\rho_1(r)$ and $\rho_2(r)$ being normalized to equal -$(Z_1 + q_1)$e and -$(Z_2 + q_2)$e respectively. We further think of the point charge Z_1e as being made of two point charges, $(Z_1 + q_1)e$ and $(-q_1)e$; Z_2e is similarly decomposed into $(Z_2 + q_2)e$ and $(-q_2)e$. q_1e and q_2e here denote the net ionic charges on atoms 1 and 2 respectively. We make this decomposition so that the Coulombic interaction term naturally arises in the expression for the net interaction potential $V(r)$,

$$V(r) = ZBL_{Z_1+q_1,Z_2+q_2}(r) + \frac{q_1q_2e^2}{4\pi\epsilon_0 r} + t_1 + t_2 \ , \tag{2.1}$$

where $ZBL_{Z_1+q_1,Z_2+q_2}(r)$ denotes the ZBL form of interaction between two neutral atoms having atomic numbers $Z_1 + q_1$ and $Z_2 + q_2$. t_1 denotes the interaction between the point charge $-q_1e$ and the $(Z_2 + q_2)e$ point charge plus electron cloud system of the atom 2, and is given by

$$t_1(r) = \frac{-q_1e^2}{4\pi\epsilon_0}[\frac{Z_2 + q_2}{r} - \frac{1}{r}\int_0^r 4\pi s^2\rho_2(s)ds - \int_r^\infty 4\pi s\rho_2(s)ds] \ , \tag{2.2}$$

while t_2 is the converse remaining point-atom interaction, expressed similarly. Eq. (2.1) is correct for atomic separations smaller than the chemical bond length, and for very large atomic separations as well. In the latter case, only the 2nd term in Eq. (2.1) survives as we show below.

2.2.3 Determination of relevant charge densities

The task now is the determination of $\rho_O(r)$ and $\rho_U(r)$. It is here important to notice that the potential for very small interatomic separations is only as good as the ZBL

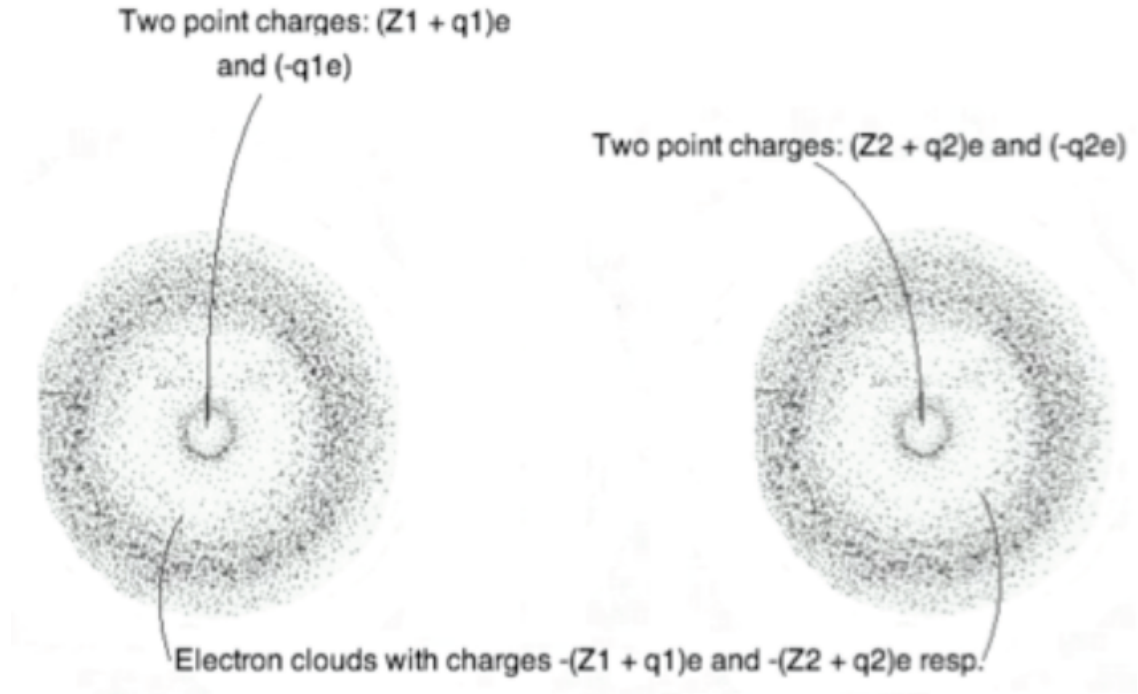

Figure 2.2: Decomposition of spherically symmetric charges to facilitate generalization of ZBL potential.

form (see Eq. (2.1)). Thus, we use the charge densities employed for ZBL, which are primarily Hartree-Fock-Slater atomic distributions for most of the atomic pairs. We fit the numerical data for charge density used by Ziegler *et al.* to a sum of Slater functions. While the density $\rho(r)$ is known through numerical evidence (we are not aware of a rigorous proof) to be a monotonic decreasing function of radial distance for all atoms, the graph of $4\pi r^2\rho(r)$ exhibits a number of peaks (see Figure 2.3) corresponding to atomic shells. To ensure the best possible accuracy, we fit to $4\pi r^2\rho(r)$ because this is the quantity entering Eq. (2.1). We find that 2 and 4 Slater functions are sufficient to capture the behavior of $4\pi r^2\rho(r)$ for neutral oxygen and uranium atoms (see Figure 2.3), i.e.,

$$\rho_O(r) = a_1 e^{-k_1 r} + a_2 r e^{-k_2 r} \tag{2.3}$$

$$\rho_U(r) = b_1 e^{-l_1 r} + b_2 r e^{-l_2 r} + b_3 r^2 e^{-l_3 r} + b_4 r^3 e^{-l_4 r} \ . \tag{2.4}$$

The Slater function fits needed a slight modification in their pre-factors, since the areas under the curves for the fitted functions for uxygen and uranium do not exactly equal 8 and 92, respectively. In addition, the pre-factors in the above two equations as reported in Table 2.1 have been multiplied by 10/8 for oxygen and 88/92 for uranium because we are interested in the electronic cloud of the ionic species and not of the neutral atoms. We also experimented with more sophisticated corrections (e.g., using noble gas densities instead) but this did not change the results by more than the intrinsic accuracy of the ZBL potential.

Table 2.1: Values of coefficients in Slater functions in Eqs. (2.3) and (2.4)

$a_1 = 2239.70$ eÅ^{-3}	$a_2 = 168.83$ eÅ^{-4}	$k_1 = 30.76$ Å^{-1}
$k_2 = 6.77$ Å^{-1}	$b_1 = 3232265.1$ eÅ^{-3}	$b_2 = 13855550.9$ eÅ^{-4}
$b_3 = 5207885.3$ eÅ^{-5}	$b_4 = 141768.5$ eÅ^{-6}	$l_1 = 309.92$ Å^{-1}
$l_2 = 87.23$ Å^{-1}	$l_3 = 32.98$ Å^{-1}	$l_4 = 13.80$ Å^{-1}

2.2.4 Final form of the general interatomic potential

By using Eqs. (2.3) and (2.4) in Eq. (2.1) and performing the integrations, we obtain the following pair potentials for oxygen-oxygen, uranium-uranium and oxygen-uranium respectively:

$$V_{OO}(r) = ZBL_{10,10}(r) + \frac{(-2)(-2)e^2}{4\pi\epsilon_0 r} - \frac{4e^2}{4\pi\epsilon_0}[\frac{10}{r} - 4\pi f_{OO}(r)] \tag{2.5}$$

$$V_{UU}(r) = ZBL_{88,88}(r) + \frac{(4)(4)e^2}{4\pi\epsilon_0 r} + \frac{8e^2}{4\pi\epsilon_0}[\frac{88}{r} - 4\pi f_{UU}(r)] \tag{2.6}$$

$$V_{OU}(r) = ZBL_{88,10}(r) + \frac{(4)(-2)e^2}{4\pi\epsilon_0 r} - \frac{2e^2}{4\pi\epsilon_0}[\frac{88}{r} - 4\pi f_{UU}(r)] + \frac{4e^2}{4\pi\epsilon_0}[\frac{10}{r} - 4\pi f_{OO}(r)] \tag{2.7}$$

where we have,

$$f_{OO}(r) = \frac{6a_2}{rk_2^4} - \frac{a_2 e^{-k_2 r}}{rk_2^4}[6 + 4k_2 r + k_2 r^2] + \frac{a_1}{rk_1^3}[2 - 2e^{-k_1 r} - k_1 r e^{-k_1 r}] \tag{2.8}$$

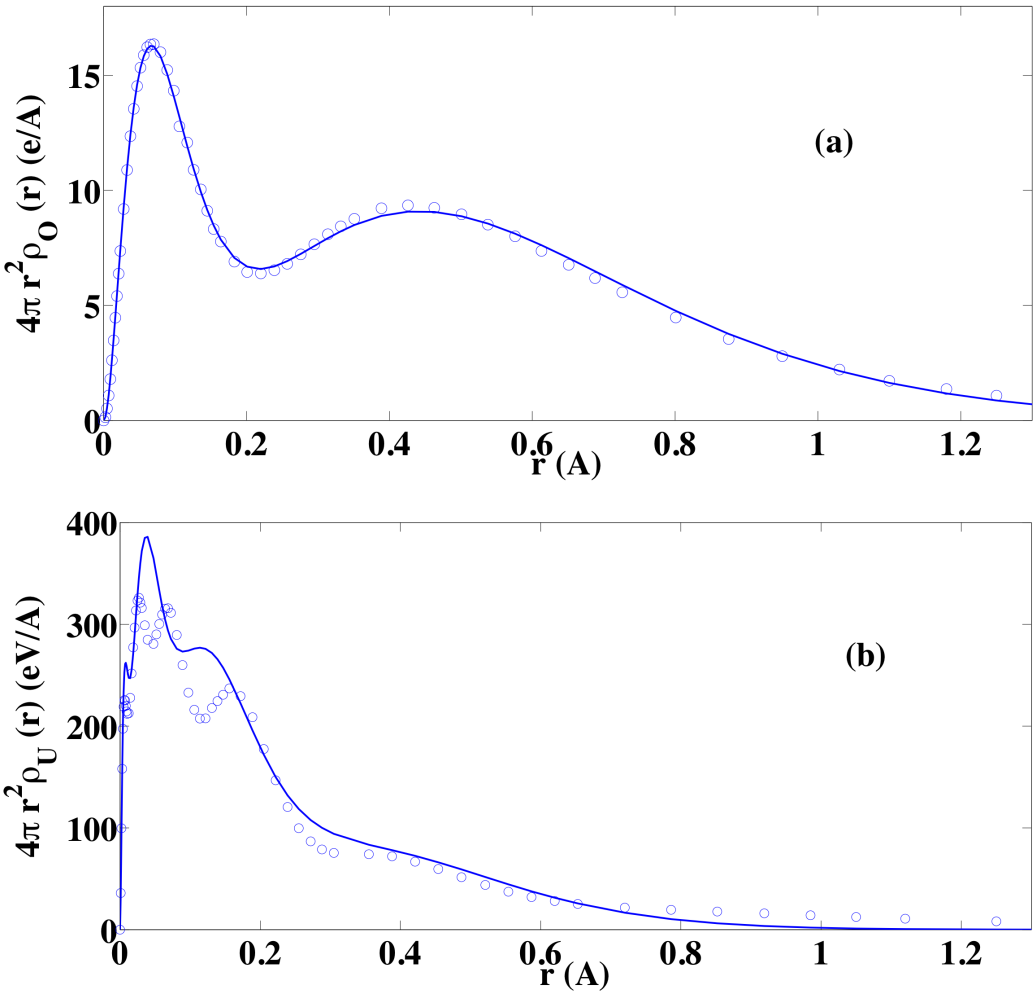

Figure 2.3: Charge density times $4\pi r^2$ fitted to sum of Slater functions for (a) oxygen and (b) uranium. Open circles denote values used by Ziegler *et al.*, [2] while the solid lines indicate our fit using sum of Slater functions. The resultant error in the short-range interatomic potential as compared to ZBL's original potential was well within the latter's standard deviation for both (a) and (b). Thus trying to capture more peaks for uranium, by introducing more Slater functions, was not necessary. The coefficients used here are provided in Table 2.1.

$$f_{UU}(r) = \frac{120b_4}{rl_4^6} - \frac{b_4 e^{-l_4 r}}{rl_4^6}[120 + 96l_4 r + 36l_4^2 r^2 + 8l_4^3 r^3 + l_4^4 r^4] +$$
$$\frac{24b_3}{rl_3^5} - \frac{b_3 e^{-l_3 r}}{rl_3^5}[24 + 18l_3 r + 6l_3^2 r^2 + l_3^3 r^3] +$$
$$\frac{6b_2}{rl_2^4} - \frac{b_2 e^{-l_2 r}}{rl_2^4}[6 + 4l_2 r + l_2 r^2] + \frac{b_1}{rl_1^3}[2 - 2e^{-l_1 r} - l_1 r e^{-l_1 r}] \quad (2.9)$$

We illustrate in Figure 2.4 how closely the potentials given in Eqs. (2.5-2.7) match, for small r, the neutral atom ZBL, and for large r, the relevant Coulombic interaction.

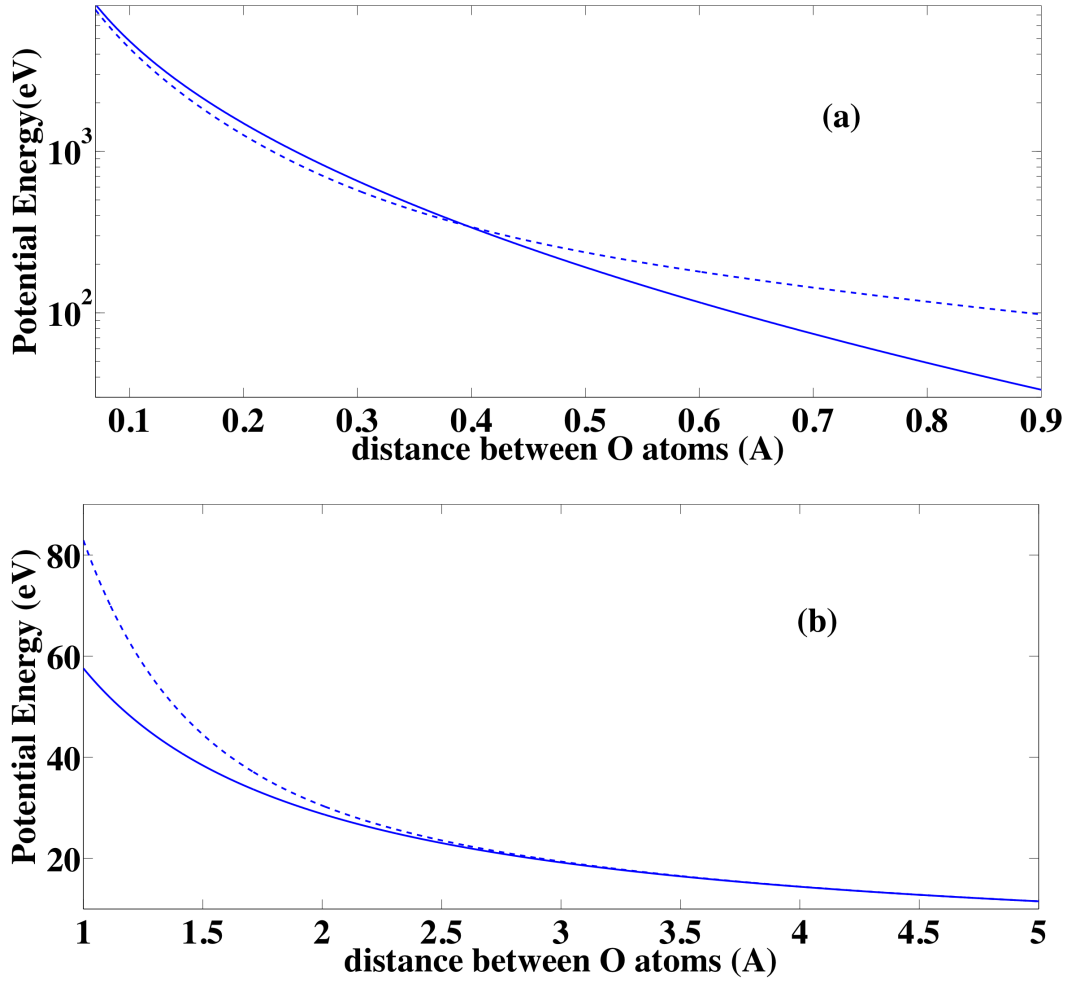

Figure 2.4: Comparison of our analytical potential form (dashed line) with (a) the currently used neutral atom ZBL interaction (solid line) for small distances, and (b) the ionic Coulombic interaction (solid line) between two (-2e)point charges for large distances for the case of two oxygen atoms.

2.3 *Ab initio* calculations to fine-tune potential in intermediate distance range

As for any empirical potential, there is an intermediate distance range for which the interactions follow neither a ZBL nor a purely Coulombic form. A correction term is thus needed for this regime. We find this correction term by fitting to an extensive database of GGA+U *ab initio* calculations on UO_2.

2.3.1 *Ab initio* GGA+U calculations

GGA+U is known to provide electronic and magnetic behaviors of UO_2 that are consistent with experiments [8], and a correct treatment of the localized and strongly correlated $5f$ electrons of uranium [9,10]. Our *ab initio* calculations also take into account the experimentally observed noncollinear antiferromagnetic magnetic moment ordering and the oxygen cage distortion in UO_2 [11]. Therefore, in addition to capturing correct elastic and defect properties, our potential also covers a much more vast energy landscape in the material due to the richness of the *ab initio* data used. We fit to a database obtained by GGA+U calculations with the projector-augmented-wave method implemented in the VASP [12] package. In the GGA+U approximation, the spin-polarized GGA potential is supplemented by a Hubbard-like term to account for the strongly correlated $5f$ orbitals [13]. We use the rotationally invariant approach to GGA+U due to Dudarev *et al.* [14], wherein the parameter U-J is set to 3.99 eV. This is the generally accepted value for this parameter to reproduce the correct band structure for UO_2 [15].

2.3.2 *Ab initio* database details

The *ab initio* database we use in fitting comprises:

- Isochoric relaxed runs on a 12 atom unit cell which was isometrically contracted and expanded by various amounts (i.e., equation of state calculations), and for which an energy cutoff of 500 eV and a 8×8×8 k-point grid were taken; k-point

convergence was ascertained before choosing this value for the k-point grid. The cell was allowed to relax in shape but not in size. Ionic relaxations were carried out until residual forces were less than 0.01 eV/Å.

- Static (i.e., no ionic relaxation) runs on 96 atom 2×2×2 supercell in which one atom at a time (i.e., oxygen or uranium) was perturbed from its equilibrium position by varying distances in different directions. Energy cutoff was 500 eV. Gamma point only version of VASP was used for this. Note that any interactions between atoms and their periodic images do not systematically bias the fit of the potential because the same supercell geometry is used in both the *ab initio* and the empirical potential energy calculations.

- 96 atom 2×2×2 supercell for the formation energies of three kinds of stoichiometric defects, namely oxygen Frenkel pair, uranium Frenkel pair and Schottky trio. The vacancies and the interstitials were taken as far from each other as the supercell would allow. The details of the calculations are the same as that for case (ii) above. Correct prediction of defect energies has been given great importance in generating interatomic potentials for cascade simulations.

- first-order transition states in a 2×2×2 supercell for the migration energy of oxygen vacancy and oxygen interstitial. Nudged elastic band (NEB) method in conjunction with the climbing image method [16] for determination of saddle point energy, as implemented in VASP, was used for this. We did not fit to corresponding migration energies for uranium defects since uranium defect diffusion processes are known from experiments to be very insignificant compared to diffusion of oxygen defects: The diffusivity of oxygen at 1400°C in UO_2 is more than five orders of magnitude larger than that of uranium [17]. Also, uranium vacancies and interstitials are minority defects in UO_2 since their formation energies are very high (see Table 2.2).

Table 2.2: Comparison of defect formation and migration energies (all in eV), between our values and best values as per previous potentials [3, 5], compared with *ab initio* values from this work and with experimental values [18].

	Exptl.(E)/ *ab initio*(AI)	This work	Previous potentials
O Frenkel Pair Formation	3.5 +/- 0.5(E), 3.9 (AI)	3.3	3.17
U Frenkel Pair Formation	9.5 -12(E),10.1 (AI)	15.5	12.6
Schottky Trio Formation	6.5+/- 0.5(E),7.4 (AI)	7.1	6.68
O Interstitial Migration	0.9-1.3(E)	1.4	0.65
O Vacancy Migration	0.5(E)	0.5	0.33

2.4 Final potential form and details of the fitting procedure

2.4.1 Potential form with intermediate distance correction

With the *ab initio* database so generated, we now fit the final potential forms as follows.

$$V_{UU}(r) = ZBL_{88,88}(r) + \frac{(4)(4)e^2}{4\pi\epsilon_0 r} + \frac{8e^2}{4\pi\epsilon_0}[\frac{88}{r} - 4\pi f_{UU}(r)] \quad \forall \quad 0 < r < 12\text{Å} \quad (2.10)$$

$$V_{OO}(r) = \frac{(-2)(-2)e^2}{4\pi\epsilon_0 r} + \begin{cases} ZBL_{10,10}(r) - \frac{4e^2}{4\pi\epsilon_0}[\frac{10}{r} - 4\pi f_{OO}(r)] & 0 < r \leq 1.17\text{Å} \\ 5^{th}\ order\ polynomial & 1.17\text{Å} < r \leq 2.28\text{Å} \\ 3^{rd}\ order\ polynomial & 2.28\text{Å} < r \leq 2.84\text{Å} \\ -603.268\text{eV}^6/r^6 & 2.84\text{Å} < r < 12\text{Å} \end{cases}$$

$$V_{OU}(r) = \frac{(-2)(4)e^2}{4\pi\epsilon_0 r} + \begin{cases} ZBL_{88,10}(r) + \frac{4e^2}{4\pi\epsilon_0}[\frac{10}{r} - 4\pi f_{OO}(r)] - \frac{2e^2}{4\pi\epsilon_0}[\frac{88}{r} - 4\pi f_{UU}(r)] & 0 < r \leq 1.42\text{Å} \\ 5^{th}\ order\ polynomial & 1.42\text{Å} < r \leq 1.70\text{Å} \\ 394.391\text{eV}\exp(-r/0.534) - 1.5\text{eV}^6/r^6 & 1.70\text{Å} < r < 10\text{Å} \end{cases}$$

As seen from Eq. (2.10) we now have absolutely no splines for the U^{+4}-U^{+4}

interaction, reflecting the fact that no chemical bonding takes place. There are splines in the other two interactions but these are now unambiguously determined since the respective cut-offs are not imposed but instead determined through fitting. The splines maintain continuity through the second derivatives of the potential and the specific form of the splines can be uniquely recovered from these conditions. For the interaction between two oxygen ions, the potential has one (and only one) minimum at $r_{min} = 2.28$Å, as may be seen from Figure 2.5. We have thus removed all unaccounted behaviors in the potentials, which were demonstrated for the case of oxygen-oxygen interaction in Figure 2.1.

2.4.2 Details of the fitting procedure

The downhill simplex method of Nelder-Mead was used to carry out the fitting [19]. The fitting involved minimizing the sum of the squares of the differences between the *ab initio* energies and the energies predicted by the potential for classes (i) and (ii) of data points as detailed above, and the sum of the squares of the differences between the *ab initio*/experimental and predicted values of the various defect formation/migration energies respectively. The package GULP [20] was used for energy calculations and for atomic positions optimization. The quality of fit for the equation of state data and the perturbed atom data can be seen in Figure 2.6. The *ab initio*/experimental and predicted defect formation/migration energies are compared in Table 2.2, while Table 2.3 lists the predicted ground-state lattice parameter and other elastic properties as compared with the corresponding experimental values [18] (extrapolated accordingly) and with values obtained with the Morelon *et al.* potential [3]. The agreement is very satisfactory.

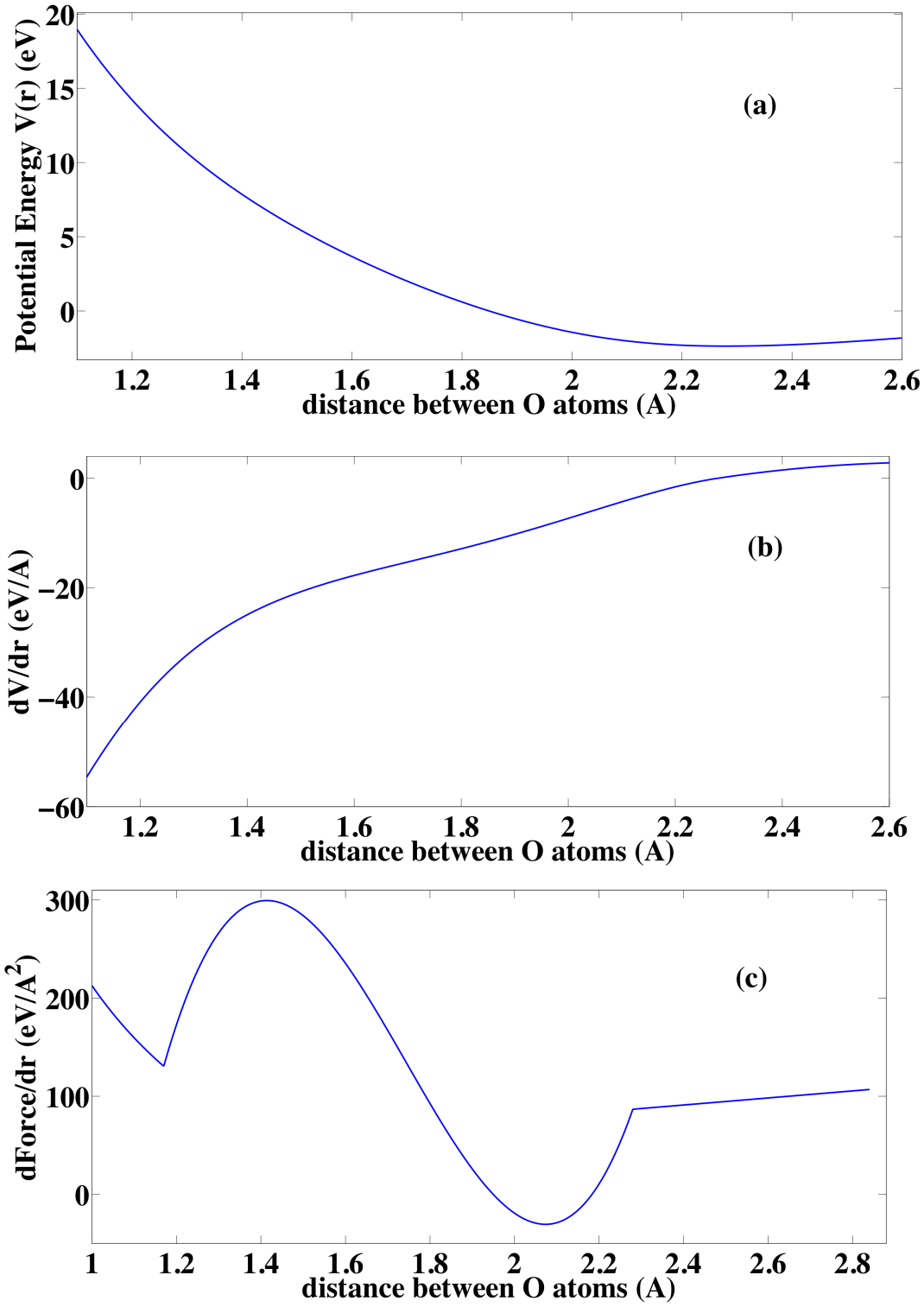

Figure 2.5: (a) The interatomic potential for oxygen-oxygen as per current work (Eq. 10). (b) First derivative of the net potential resulting from the same. (c) Second derivative of the potential. These are to be compared with Figure 2.1.

Table 2.3: Comparison of various ground- state elastic properties, between our values and best values as per previous potentials [3], compared with (extrapolated) experimental values [18]. N.B. These are *predicted* and not *fitted* values.

	Exptl.	This work	Previous potentials
Lattice Parameter (Å)	5.46	5.46	5.46
Bulk Modulus (GPa)	207	210	125
Elastic Constant C_{11} (GPa)	389.3	401.8	216.9
Elastic Constant C_{12} (GPa)	118.7	114.1	79.1
Elastic Constant C_{44} (GPa)	59.7	107.8	78.5

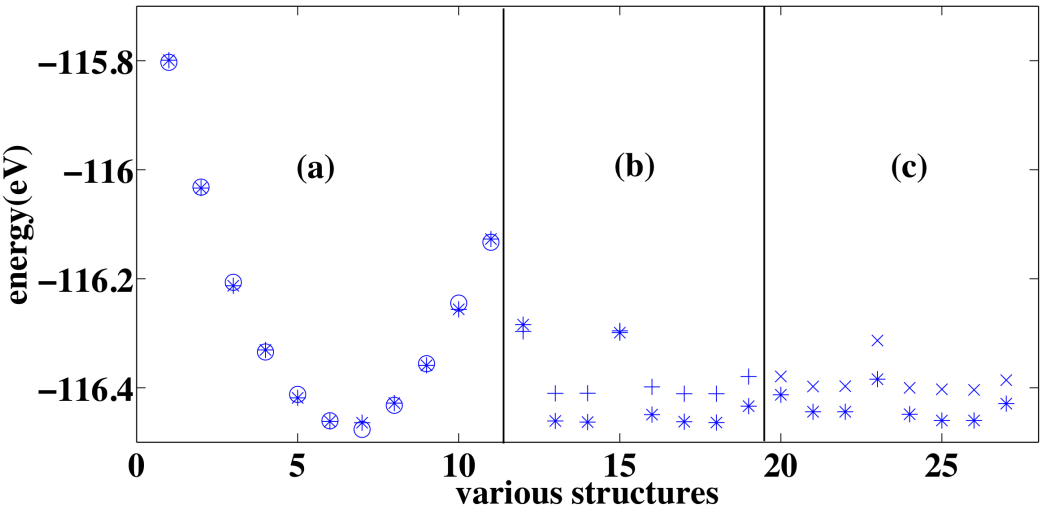

Figure 2.6: Quality of fit from our fitted potential for various *ab initio* energies: (a) expansion/contraction (open circles), (b) oxygen atom perturbation (plus signs), (c) uranium atom perturbation (cross signs). Asterisks denote experimental data. For each of oxygen and uranium, the first four perturbations are along $< 100 >$ direction while the second four are along $< 110 >$ direction.

2.5 Validation of the potential through MD simulations

As a final validation of the developed potential we considered various dynamic properties by performing MD simulations in a constant number, pressure and temperature (NPT) ensemble comprising 6×6×6 unit cells. The system was equilibrated for 10.0 ps, while production runs were carried out for 100.0 ps, with a time step of 0.001 ps and sampling every 0.05 ps. The fluorite structure remained stable during all the runs we performed, up to temperatures of 2500 K. The properties we considered are the variation in the lattice parameter and the enthalpy as functions of the temperature. These are compared in Figure 2.7 with the corresponding experimental data. [18] The quality is similar to what is given by the previous potentials [3, 21, 22], as tabulated in the work by Morelon *et al.* [3].

2.6 Summary

To summarize, we have shown a methodology for developing an interatomic pair potential such that it is appropriate for all relevant interatomic separations, without the need for any ambiguous splines. Splining between regions of different characteristics is not just an inconvenience in the implementation of a potential in MD simulations, but also introduces an uncertainty regarding which distances, and by which functions, one realizes the splines.

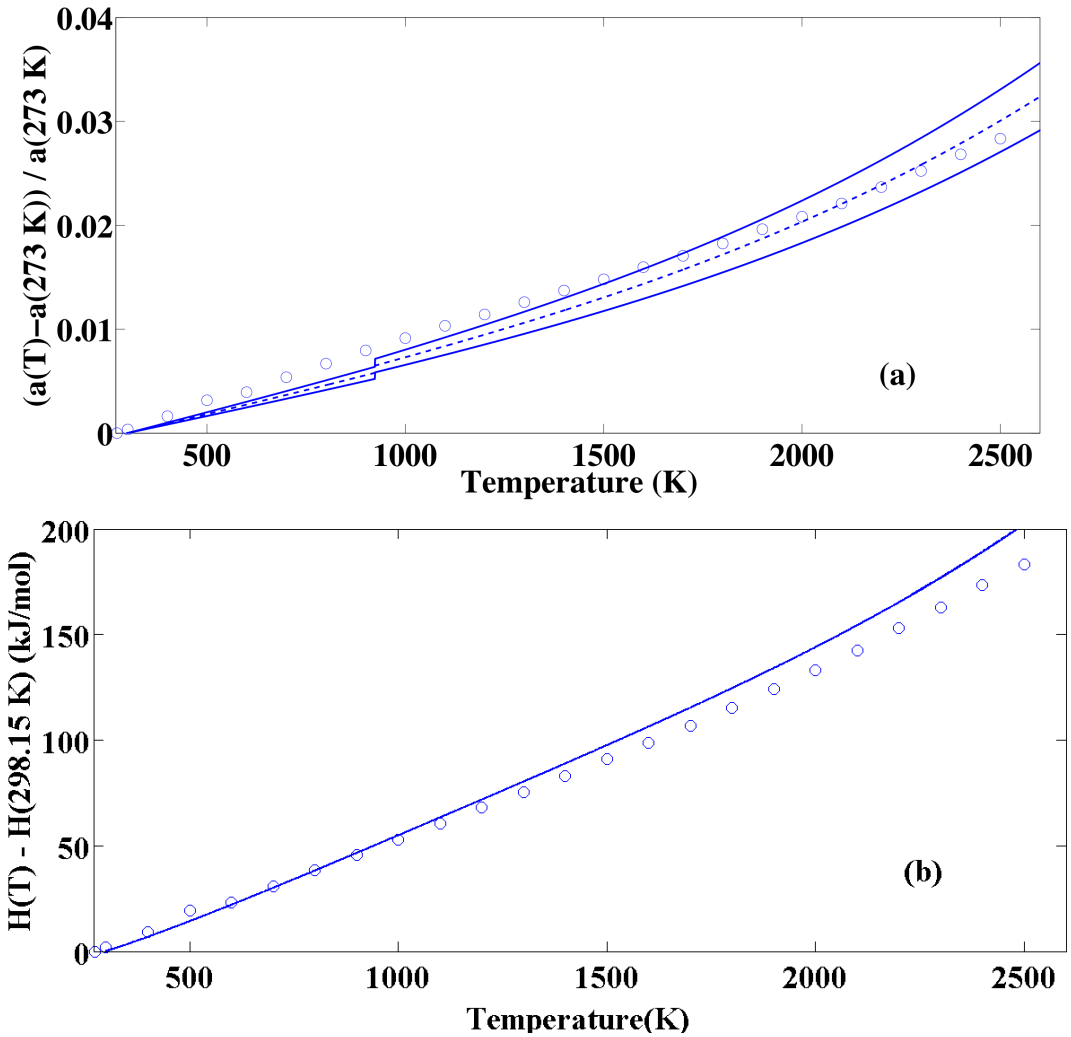

Figure 2.7: (a) Relative lattice parameter variation using potential from current work (open circles) compared with corresponding experimental values (dashed line). [18] The scatter in the experimental values is also shown (solid lines). (b) Enthalpy variation using potential from current work (open circles) compared with corresponding experimental values (solid line). [18] The scatter in the experimental values was less than 1 percent and is thus not shown.

Chapter 3

Interatomic potentials for mixed oxide (MOX) nuclear fuels

3.1 Motivation

This chapter continues with developing accurate and robust interatomic potentials for use in classical molecular dynamics simulations of atomistic phenomena occurring at energy scales ranging from lattice vibrations to crystal defects to high-energy collisions.

The interest in using mixed oxide (MOX) fuels comprising (U,Pu,MA)O_2 (where MA = Np, Am and Cm) in fast breeder and transmutation reactors is ever increasing. Since this complex fuel experiences a high burn-up ratio with large quantities of fission products and materials defects, it becomes crucial to understand the evolution and statistics of atomic displacement cascades due to high-energy radiation that the material faces [23]. Classical molecular dynamics (MD) with its ability to simulate fairly long length scales, though still retaining the fine atomic structure of the material, is ideally suited for such studies. Classical MD is limited though by the time scale problem, an issue we will be tackling in later parts of this thesis.

In this chapter we continue to address the issue that the complexity of the interatomic interactions for radiation damage simulations cannot be fully represented

by simple classical forms due to the disparate scales of energies involved. Interactions corresponding to equilibrium conditions are traditionally found by fitting to a variety of thermodynamic data; while for description of the short-range behavior, the Ziegler-Biersack-Littmark (ZBL) universal pair potential [2] developed in the 1980s is well-accepted. These two "pieces" then need to be smoothly connected via somewhat arbitrarily applied splines. In Chapter 2 we proposed a methodology for developing interatomic potentials that is valid for all interatomic separations, without the need for any ambiguous splines [24]. We used the formalism to develop force-fields for the nuclear fuel UO_2 that captured a wide range of properties, as described in Chapter 2. In this chapter, we extend the formalism to a more general case of MOX nuclear fuels of varying composition. In addition to capturing high-temperature thermodynamic properties, as done by available potentials [25–27], we also incorporate correct treatment of point defects. Created due to irradiation, these are critical for the understanding of a variety of phenomena such as fuel swelling, fission gas release and burn-up structure formation [1, 3].

3.2 Details of calculations

A key test of any developed energy surface lies in its ability to adequately represent systems/configurations that were not included in the fitting procedure [28]. In this chapter we fit the potential parameters to *ab initio* and experimental data for the oxides PuO_2 and NpO_2, and then check for their transferability by comparing against *ab initio* data for $(U_xPu_{1-x})O_2$ and $(U_xNp_{1-x})O_2$ configurations that were not included in the fit.

3.2.1 *Ab initio* GGA+U calculations

In the present chapter we employ the generalized potential formalism [24] that behaves correctly in both short-range and long-range limits. The only component in this potential that remains to be determined is a correction term for intermediate distances associated with chemical bonding. We find this correction term by fitting

to an extensive database of generalized gradient approximation GGA+U *ab initio* calculations [13] on PuO_2 and NpO_2. The potential's applicability in a mixed environment pertinent to MOX fuels is further verified by testing against GGA+U data for $(U_xPu_{1-x})O_2$ and $(U_xNp_{1-x})O_2$.

GGA+U is known to provide electronic and magnetic behaviors of the actinide oxides [9] that are consistent with experiments. In this approximation, the spin-polarized GGA potential is supplemented by a Hubbard-type term to account for the localized and strongly correlated $5f$ electrons. Our database comprises results obtained from GGA+U calculations with the projector augmented-wave method and collinear antiferromagnetic moments as implemented in the VASP package [12]. Dudarev's rotationally invariant approach [14, 15] to GGA+U is employed wherein the parameter U-J is set to 3.99, 3.25 and 3.40 for U, Pu and Np respectively [4, 10, 29]. These are the generally accepted values for reproducing the correct band structures of the corresponding oxides. Energy cutoff for the plane waves was kept at 400 eV. Since GGA+U overestimates the lattice parameter, a common scaling factor (same as that used [24] for UO_2) was employed to get experimentally correct lattice parameters.

3.2.2 *Ab initio* database details

3.2.2.1 *Ab initio* database used in fitting the potential

The *ab initio* database so obtained for fitting comprises:

1. Isochoric relaxed runs on a 12 atom unit cell, which was isometrically contracted and expanded by various amounts (i.e., equation of state calculations wherein each data point was calculated under the constraint of constant cell volume) and for which an 8×8×8 k-point grid was taken after ascertaining k-point convergence. Ionic relaxations were carried out until residual forces were less than 0.01 eV/Å.

2. Static (i.e., no ionic relaxation) runs on a 96 atom 2×2×2 supercell in which

one atom at a time (O or Pu or Np) was perturbed from its equilibrium position by varying distances (on the order of 1 Å or less from the equilibrium positions) in different directions. Sampling of the gamma point only was found to be satisfactorily accurate for this.

3. A 96 atom 2×2×2 supercell for the formation energies of stoichiometric defects, namely, oxygen Frenkel pair, neptunium Frenkel pair and plutonium Frenkel pair. Several vacancy-interstitial distances were considered to ascertain the separation between these corresponding to the minimum defect formation energy (excluding the case of nearest neighbor distances, which was found to lead to vacancy-interstitial recombination). Correct prediction of these energies has been given great importance in generating interatomic potentials for cascade simulations in UO_2 [1, 3, 5, 6, 23, 30].

A total of approximately 50 *ab initio* configurations were thus used in the fitting. Note that in the above calculations, any interactions between atoms and their periodic images do not systematically bias the fit of the potentials because the same supercell geometry is used in both the *ab initio* and the empirical potential energy calculations.

3.2.2.2 *Ab initio* database used in validating the potential

The *ab initio* database employed for validation and for testing transferability includes equation of state runs similar to those in the fitting database, for oxides of $U_{31}Pu$, $U_{30}Pu_2$, $U_{31}Np$ and $U_{30}Np_2$, each with 64 oxygens. These data points were not included in the fit itself and were used only after the fitting was complete for checking the robustness of the potentials with respect to use in mixed environments.

3.2.3 Experimental data used in fitting

In addition to the *ab initio* data, we also included experimental thermal expansion behavior [31] of PuO_2 and NpO_2 in the fit. We found that including experimental thermal expansion data (which is readily available) is a very effective way to ensure reasonable thermal expansion behavior in this system. To make the calculation of

high-temperature lattice parameters computationally tractable during the fitting procedure, we employed the *quasiharmonic approximation* (QHA) [32], in which atoms are treated as pure harmonic oscillators whose frequencies depend on the cell volume. The so-called *zero static internal stress approximation* (ZSISA) [33] to QHA, as implemented in the package GULP, was used [20]. QHA involves a full relaxation with respect to external (cell parameters) and internal (atom positions within the cell) coordinates. ZSISA ignores the dependence on internal coordinates of the vibrational part of the free energy. We found that for the materials studied and potential forms used in this chapter, the lattice parameter through NPT (constant number, pressure, temperature) MD was slightly lower than that through ZSISA. As such, an empirical adjustment to the ZSISA lattice parameter had to be included in the fitting. Thus, several independent fits were done using ZSISA lattice parameter values equal to the experimental lattice parameter multiplied by η, with η varying between 1 and 1.01. NPT MD was carried out with these potentials (details of MD provided later) to find the η that led to MD values matching the experimental data the best. We found that η equals 1.0006 and 1.0008 for PuO_2 and NpO_2 respectively, for a best match in the least squares sense between experimental and NPT MD lattice parameters.

3.3 Form of the developed potential

The potential forms thus used for fitting to the *ab initio* and experimental data are similar to that proposed previously [24], and are summarized below for Pu-Pu and Pu-O interactions (with similar forms for other interactions):

$$V_{PuPu}(r) = ZBL_{90,90}(r) + \frac{(4)(4)e^2}{4\pi\epsilon_0 r} + \frac{8e^2}{4\pi\epsilon_0}[\frac{90}{r} - \frac{4\pi}{e}f_{PuPu}(r)] \quad \forall \quad 0 < r \qquad (3.1)$$

$$V_{OPu}(r) = \frac{(-2)(4)e^2}{4\pi\epsilon_0 r} +$$
$$ZBL_{90,10}(r) + \frac{4e^2}{4\pi\epsilon_0}[\frac{10}{r} - \frac{4\pi}{e} f_{OO}(r)] - \frac{2e^2}{4\pi\epsilon_0}[\frac{90}{r} - \frac{4\pi}{e} f_{PuPu}(r)] \qquad \forall 0 < r \leq r_1$$
$$5^{th}\ order\ polynomial \qquad \forall r_1 < r \leq r_2$$
$$A\exp(-r/\rho) - B/r^6 + (r - r_3)^2(Cr^3 + Dr^2) \qquad \forall r_2 < r \leq r_3$$
$$A\exp(-r/\rho) - B/r^6 \qquad \forall r > r_3 \tag{3.2}$$

The UO_2 family of interactions is kept the same as in Chapter 2. In the above equation $ZBL_{Z_1+q_1,Z_2+q_2}(r)$ denotes the ZBL form of interaction between two neutral atoms having atomic numbers $Z_1 + q_1$ and $Z_2 + q_2$, but using the screening length for Z_1 and Z_2, as explained in Chapter 2. The functions f in the above are related to the charge densities of the respective atoms. Detailed coefficients of f_{OO} and f_{UU} can be found in Chapter 2, while f_{PuPu} and f_{NpNp} can be calculated from the relations $f_{PuPu} = (90/88)f_{UU}$ and $f_{NpNp} = (89/88)f_{UU}$. This was needed since Np^{+4} and Pu^{+4} charge densities $\rho(r)$ are not available in Ref. [2].

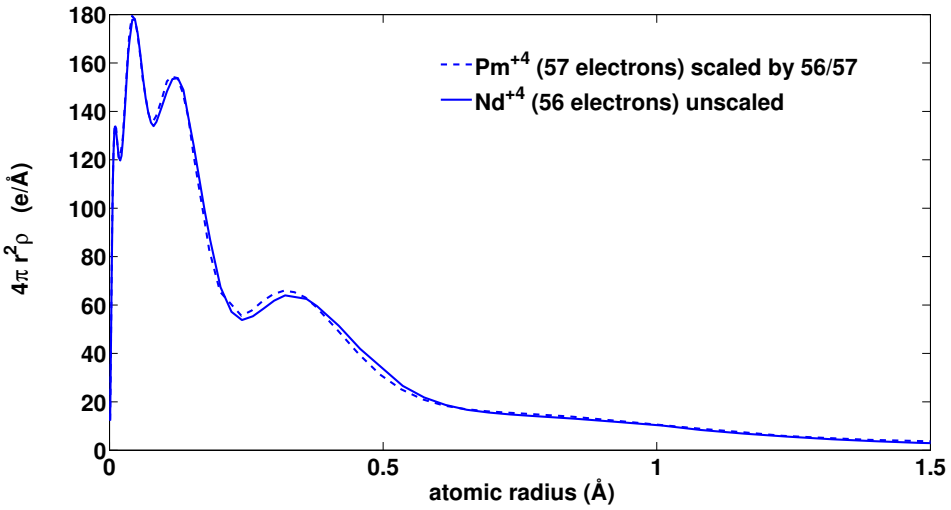

Figure 3.1: Test of approximation-validity of $f_{PuPu} = (90/88)f_{UU}$ and $f_{NpNp} = (89/88)f_{UU}$ by looking at the applicability of similar relations for cations of members of the previous row of the periodic table with similar shell structure namely Pm and Nd. Dashed line denotes the result from this approximation while solid line is the actual charge density [2] for Nd^{+4} .

We tested this approximation using cations of elements in the previous row of the periodic table where actual ZBL charge densities are available, namely Nd, Pm and Sm. As can be seen from Figure 2.2, the approximation satisfactorily captures the electronic shell structure of $4\pi r^2\rho(r)$, which is the quantity of interest to us. Note that we have removed altogether any splines for cation-cation interactions. The downhill simplex method of Nelder-Mead was then used to carry out the potential fitting [19]. The fitting involved minimizing an objective function equal to the sum of the squares of the differences between the *ab initio*/experimental data (weighted since they denote different quantities) and that predicted by the potential for all the classes of data as detailed above. GULP was used for energy calculations and for atomic-positions optimization [20].

3.4 Quality of fit

Figure 3.2 shows the quality of fit for the PuO_2 equation of states and single atom perturbation data, while Figure 3.3 shows the same for NpO_2. Table 3.1 shows the defect formation energies as obtained by us in the GGA+U calculations, along with the corresponding values from the current potential and from the previous potentials published for these systems. We excluded the cation defect formation energies entirely from the fitting objective function. This can be justified by considering that (i) these energies as per *ab initio* are already very high - upwards of 12 eV; (ii) from the case [24] of UO_2, it is expected that *ab initio* actually underestimates these energies, and thus they are even less likely to form; and (iii) these (Pu and Np) are the minority cations. It has been argued [34] though that uranium Frenkel pairs and Schottky trios might play an important role in the diffusion of noble gas impurities formed after fission - as such, our library of potentials does provide a much better match for the uranium Frenkel pair and Schottky trio formation energy since it is based on the potentials for UO_2 in Chapter 2.

The potentials so obtained are plotted in Figure 3.4, while the fitted coefficients are detailed in Table 3.2. Note that since there was no spline in any cation-cation

Table 3.1: Defect energy comparisons (in eV)

	ab initio	Potential	Previous potentials [5]
O Frenkel pair in PuO_2	3.9	4.9	7.0
O Frenkel pair in NpO_2	4.5	5.8	10.0
Pu Frenkel pair	11.9	24	17
Np Frenkel pair	12.2	26.7	17.5

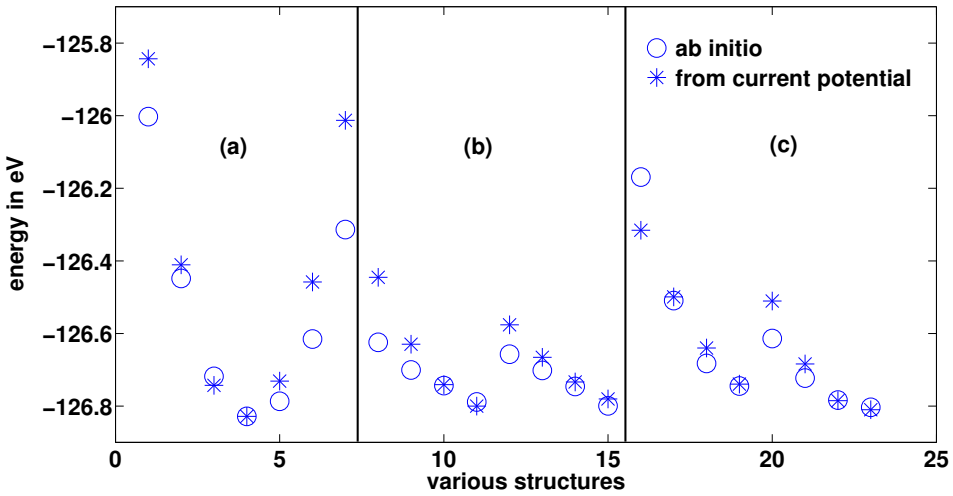

Figure 3.2: Quality of fit from our fitted potential (asterisks) for various *ab initio* energies (circles) for PuO_2 :(a) equation of state (b) oxygen atom perturbation (c) plutonium atom perturbation. For each of oxygen and plutonium, the first four perturbations are along $\langle 100 \rangle$ direction while the second four are along $\langle 110 \rangle$ direction. The perturbations are on the order of 1 Å or lower from the equilibrium positions.

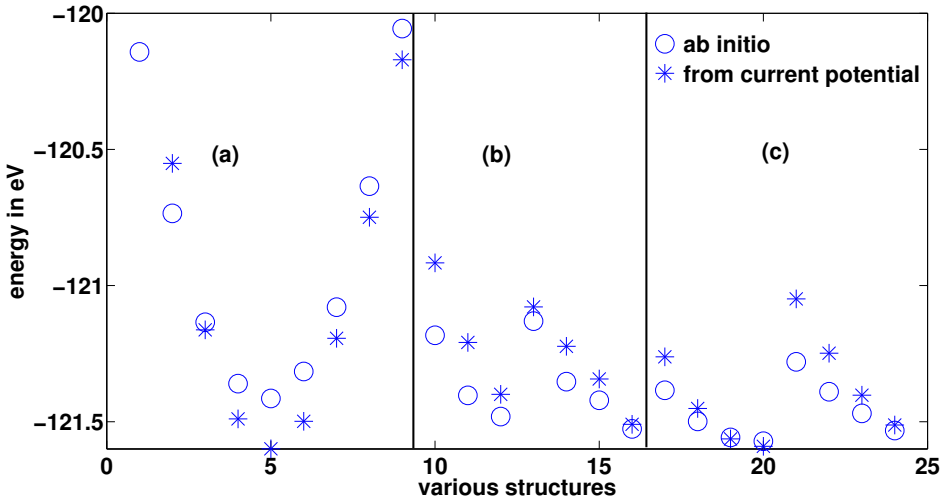

Figure 3.3: Quality of fit from our fitted potential (asterisks) for various *ab initio* energies (circles) for NpO_2 :(a) equation of state (b) oxygen atom perturbation (c) neptunium atom perturbation. For each of oxygen and neptunium, the first four perturbations are along $\langle 100 \rangle$ direction while the second four are along $\langle 110 \rangle$ direction. The perturbations are on the order of 1 Å or lower from the equilibrium positions.

interaction (see Equation (3.1)), they do not find a mention in the above list. The aforementioned 5^{th} order polynomial is uniquely determined by the provided cutoffs and potentials. The detailed potentials are available from NIST-CTCMS as a GULP library file [20] .

Table 3.2: Coefficients of fitted potentials

	PuO_2	NpO_2
A (eV)	597.304	597.605
ρ (Å)	0.475712	0.484948
B (eVÅ^6)	0.31187	0.31187
C (eV/Å^5)	0.0003375	-0.0735556
D (eV/Å^4)	0.029085	0.048972
r_1 (Å)	1.42	1.17
r_2 (Å)	1.7	1.7
r_3 (Å)	2.85	2.94

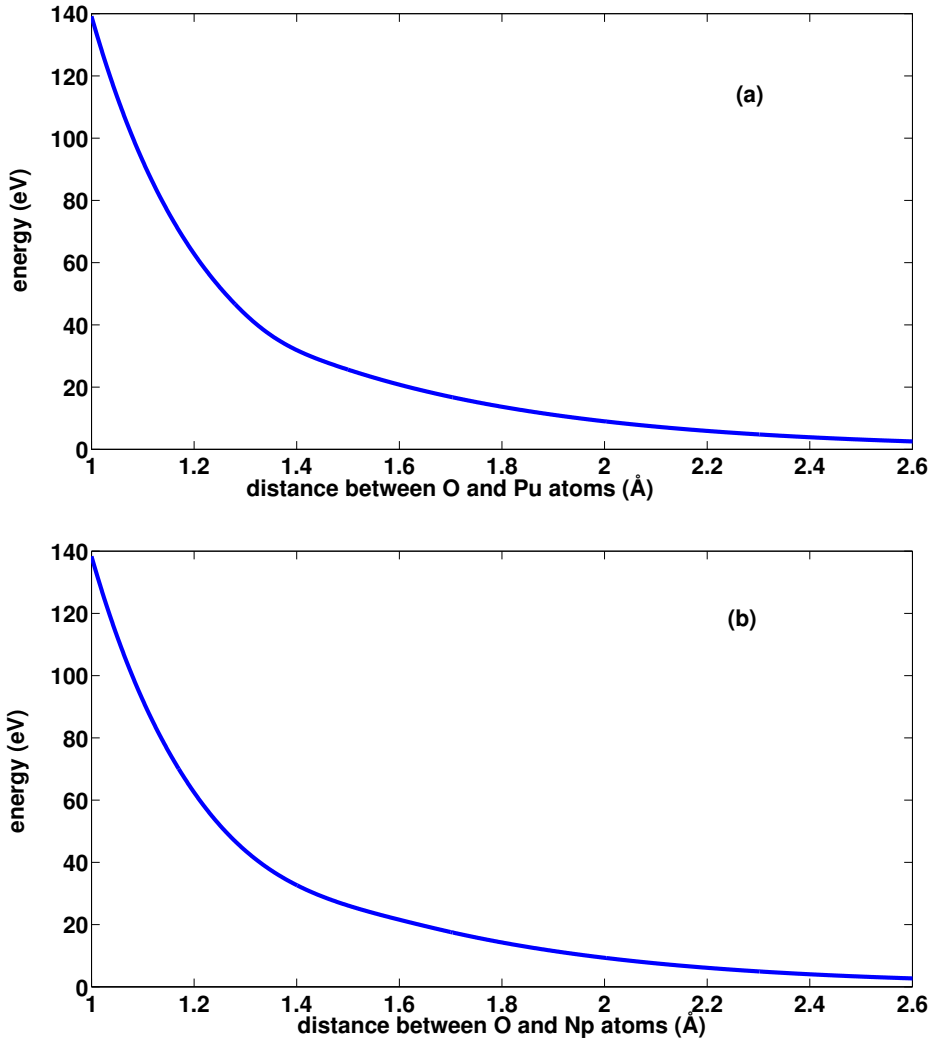

Figure 3.4: (a) fitted O-Pu interaction (b) fitted O-Np interaction

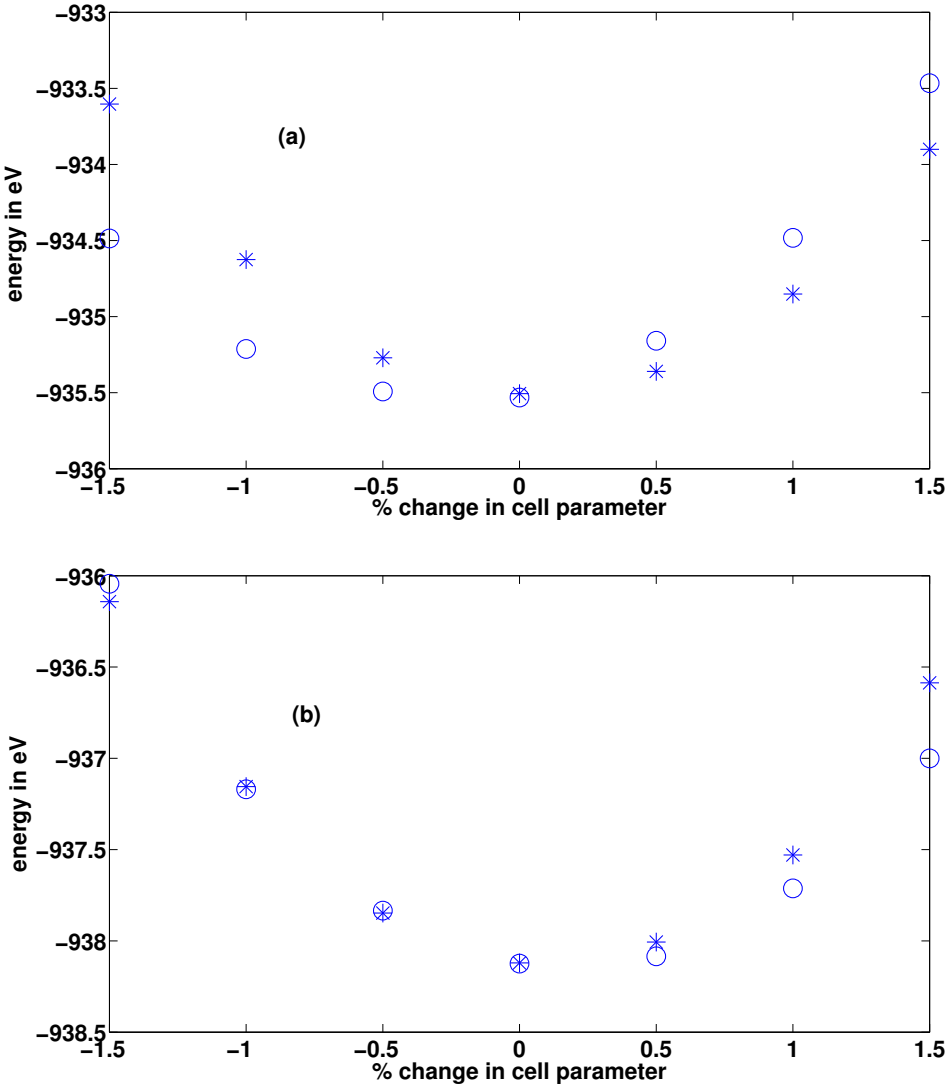

Figure 3.5: Equation of state for (a) $U_{31}PuO_{64}$ and (b) $U_{30}Pu_2O_{64}$. Circles denote *ab initio* data while asterisks are the values predicted (not fitted) with current potential.

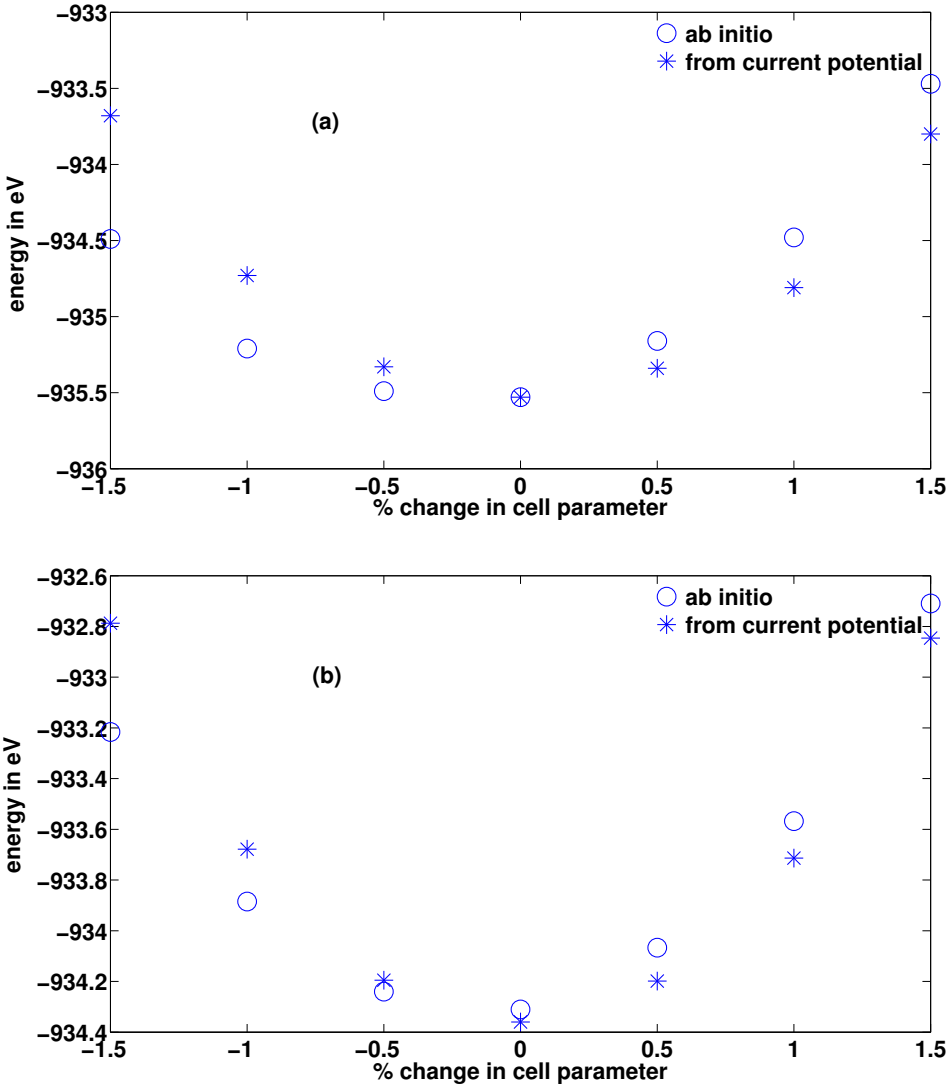

Figure 3.6: Equation of state for (a) $U_{31}NpO_{64}$ and (b) $U_{30}Np_2O_{64}$. Circles denote *ab initio* data while asterisks are the values predicted (not fitted) with current potential.

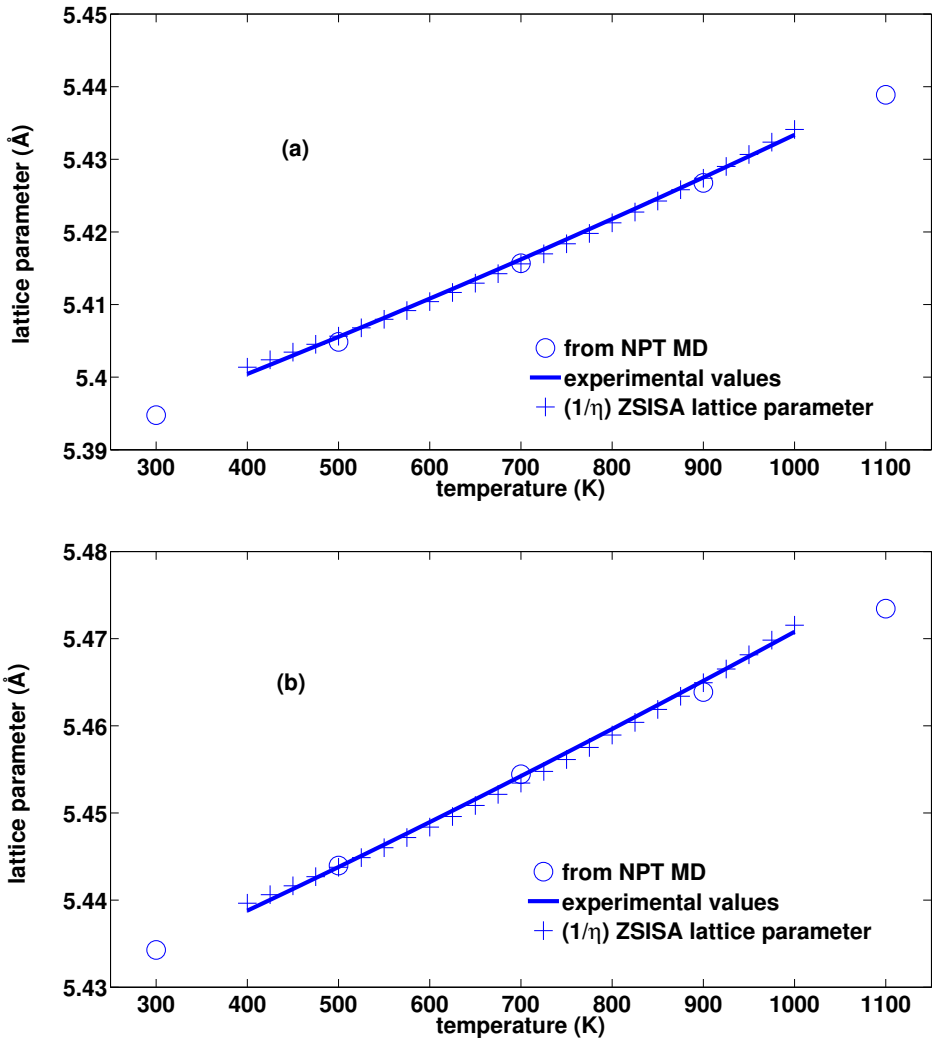

Figure 3.7: Lattice parameter at various temperatures for (a) PuO_2 and (b) NpO_2. Straight lines are the experimental values [31] valid between 400 and 1000 K, while circles denote values obtained from MD simulations using current potentials. Plus signs represent $(1/\eta)$ times the experimental values actually used in fitting to account for the observation that ZSISA slightly overestimates the MD lattice parameters. Details of calculation of this adjustment factor η (equaling 1.0006 and 1.0008 for PuO_2 and NpO_2 respectively) can be found in the text.

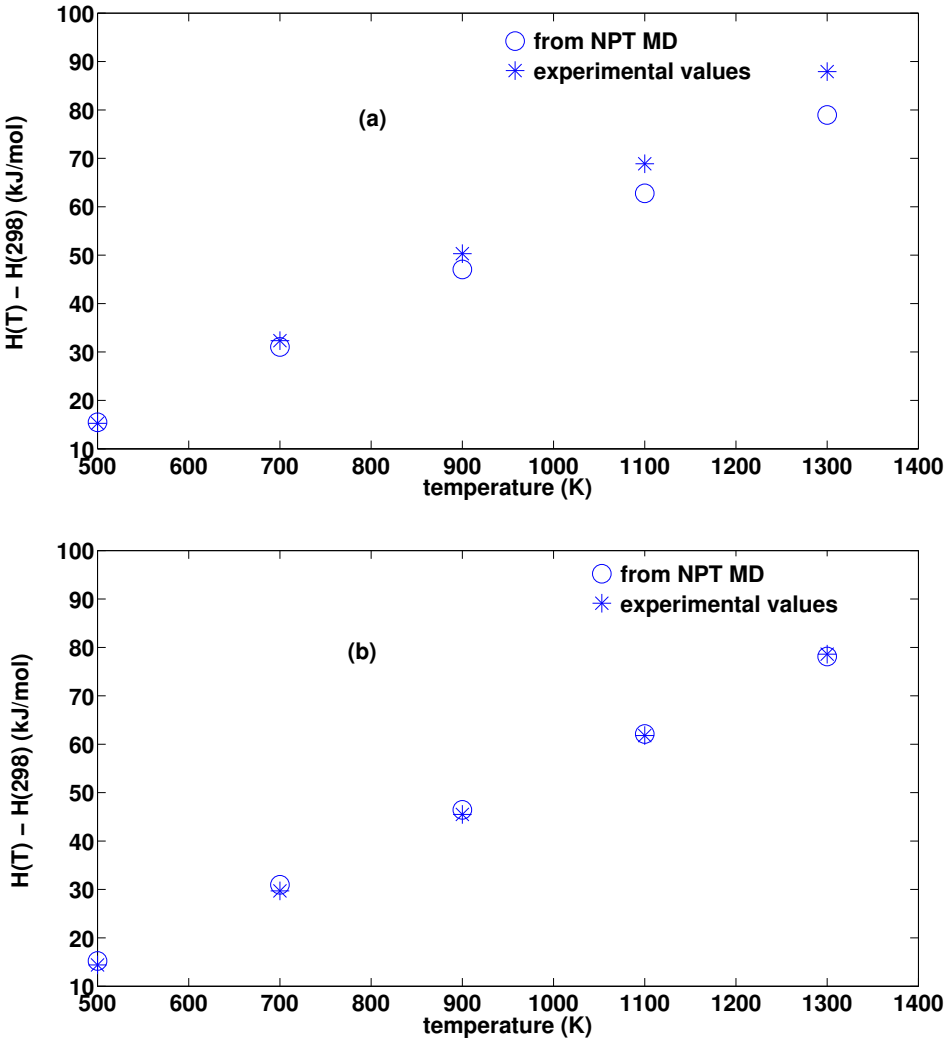

Figure 3.8: Enthalpy at various temperatures (relative to room temperature enthalpy) for (a) PuO_2 and (b) NpO_2. The circles denote values from NPT MD (predicted and not fitted values) while the asterisks are the known experimental values [35].

3.5 Validation and transferability to different environments

The performance of the potential against the validation data, i.e., equation of states for oxides of $U_{31}Pu$, $U_{30}Pu_2$, $U_{31}Np$ and $U_{30}Np_2$ that were not included in the fitting procedure, can be seen from Figures 3.5 and 3.6. The match is satisfactory and interestingly it improves with more Pu or Np content in respective cases.

The generated potentials were verified through NPT MD simulations on 3×3×3 unit cells (324 ions). The system was equilibrated for 10 ps while production runs were carried out for 100 ps with time steps between 0.001 and 0.0005 ps (depending on temperature). Apart from the lattice parameter, we also considered the enthalpy as a function of the temperature.

Figure 3.7 compares the lattice parameter as obtained from the MD simulations with experimental values for PuO_2 and NpO_2 [31]. Figure 3.7 also shows the corresponding ZSISA values as obtained from the potentials. The over-estimation adjustment factor η used on the ZSISA values can be seen here. After this adjustment to ZSISA, the match for the lattice parameters between NPT MD and experiments is excellent. The quality of the enthalpy values compared between experiments [35] and those predicted from NPT MD with current potential is also very good (see Figure 3.8).

3.6 Summary and outlook

To summarize, we have developed interatomic potentials for the Mixed Oxide fuel system (U,Pu,Np)O_2 by fitting to an extensive *ab initio* database and to available experimental observations using a formalism that has been shown to be capable of dealing in a self-contained manner with conditions ranging from thermodynamic equilibrium to very high-energy collisions relevant for fission events. The potentials cap-

ture known experimental measurements on these oxides as well as a rich database of *ab initio* GGA+U results. The applicability of these potentials in scenarios not included in the fitting is also explicitly demonstrated.

Even with the accurate and robust potentials as developed in these last two chapters, their applicability stays somewhat limited because of the restricted time scales accessible in MD simulations. For instance in nuclear fuels, there is great need to study long term annealing of defects produced during damage, but this is a task current-day MD can not challenge due to the limited time issue.

As such, in the remaining parts of this thesis we will now take on the challenge of developing and designing algorithms that can achieve realistic time scales while still maintaining fully atomistic resolution.

Chapter 4

Hybrid deterministic and stochastic approach for efficient long time scale atomistic simulations

4.1 Motivation: Time scale problem in MD

With vast improvements in the quality of available interatomic force-fields and computer power, the classical MD simulation has seen a dramatic increase in its use across a variety of fields over the past few decades [36–39]. In the previous two chapters we developed such force-fields that capture accurate quantum mechanics derived properties, and also capture high-temperature experimental observations.

In addition to the availability of good potentials, one of the features that has made MD so appealing is its ability to actually follow the dynamical evolution of the system, thus giving insight into the microscopic behavior of the material. However, this is where the major limitation of MD comes into light too: most of the interesting dynamics occurs as the system moves from one energy basin to another through infrequent rare events, while the system remains stuck in some energy basin for extended periods of time (see Figure 4.1). This non-ergodicity, coupled with the small time steps (on the order of femtoseconds) needed for total energy staying conserved, severely restricts the timescales accessible in MD simulations and also leads to limited phase space exploration.

In this chapter, we propose a hybrid deterministic and stochastic approach to achieve extended time scales in atomistic simulations that combines the strengths of MD and Monte Carlo (MC) simulations in a novel and easy-to-implement way. The method exploits the rare event nature of the dynamics similar to most current accelerated MD approaches but goes beyond them by providing, without any further computational overhead, (a) rapid thermalization between infrequent events, thereby minimizing spurious correlations and (b) control over accuracy of time scale correction, while still providing similar or higher boosts in computational efficiency.

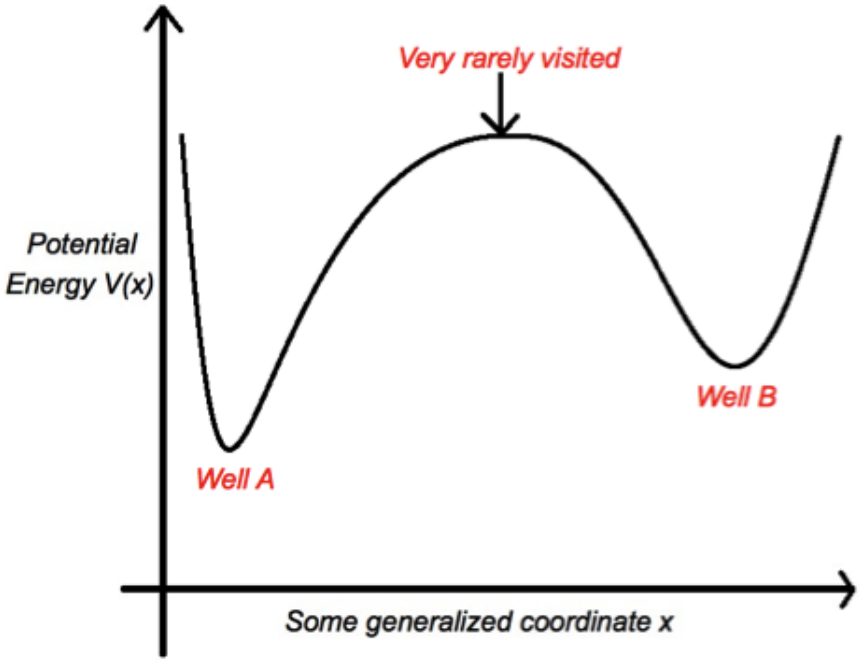

Figure 4.1: Most of the simulation time in a MD simulation gets spent near the bottom of energy wells, and transition from one well to another thus becomes a so-called *rare event*.

We present two applications of the method: (a) vacancy-mediated diffusion in Fe yields correct diffusivities over a wide range of temperatures and (b) source-controlled plasticity and deformation behavior in Au nanopillars at realistic strain rates (as low as 10^2/sec in this thesis) with excellent agreement with previous theoretical predictions and *in situ* high-resolution transmission electron microscopy (HRTEM) observa-

tions. The method gives several orders of magnitude improvements in computational efficiency relative to standard MD and good scalability with size of system.

4.2 Some previous approaches to address the time-scale problem

There have been many attempts at addressing this time-scale problem in MD - examples include hyperdynamics [40, 41], metadynamics [42], the activation relaxation technique [43], parallel replica dynamics [44], temperature accelerated dynamics [45], κ-dynamics [46] and several others [40]. In this section we provide a brief survey of some of these methods. There are several excellent reviews such as Ref. [40] available on the subject and the reader is referred to those for a more detailed *critique*. Here we restrict the discussion to algorithms that maintain a fully atomistic resolution.

4.2.1 Hyperdynamics

The hyperdynamics method [41] is a very popular and well-established method that offers an elegant and practical way to increase the rate of infrequent events. It consists of adding a potential energy bias that makes the potential wells, in which the system normally remains trapped for extended periods, less deep (see Figure 4.2). A time-scale correction is also evaluated in terms of the bias potential. The hyperdynamics method, especially with the advent of a variety of easy to implement biasing forms [47], has seen several compelling applications over the past years [47–51].

4.2.2 Kinetic Monte Carlo

The kinetic Monte Carlo (or KMC) method [40] assumes that one knows (a) all the *elementary* processes or transitions (typically escape pathways from energy wells) that could occur in a system, (b) the rates at which they occur, and (c) that these processes are of the Poisson process type and (d) these processes are independent and uncorrelated. Given these assumptions, KMC comes up with a Markov chain that

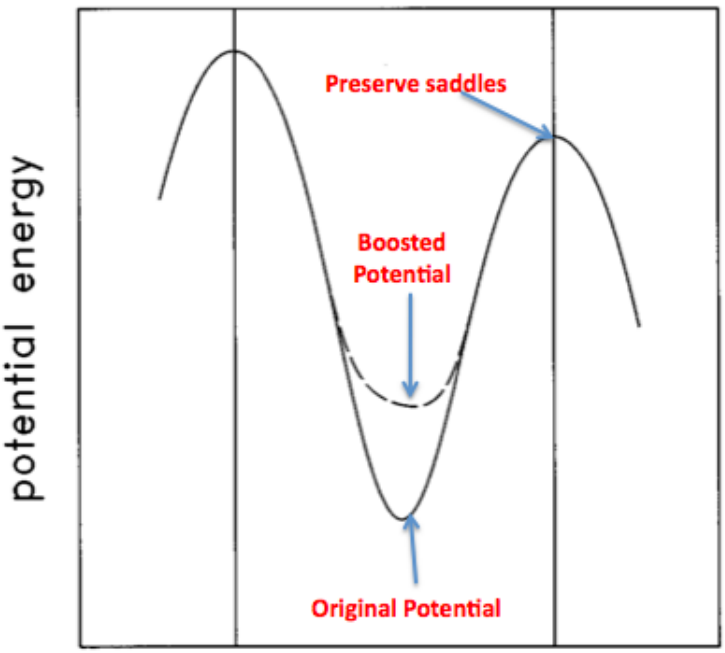

Figure 4.2: A schematic illustration of the key idea in Hyperdynamics [41]: lifting the potential energy landscape without affecting the saddle surfaces.

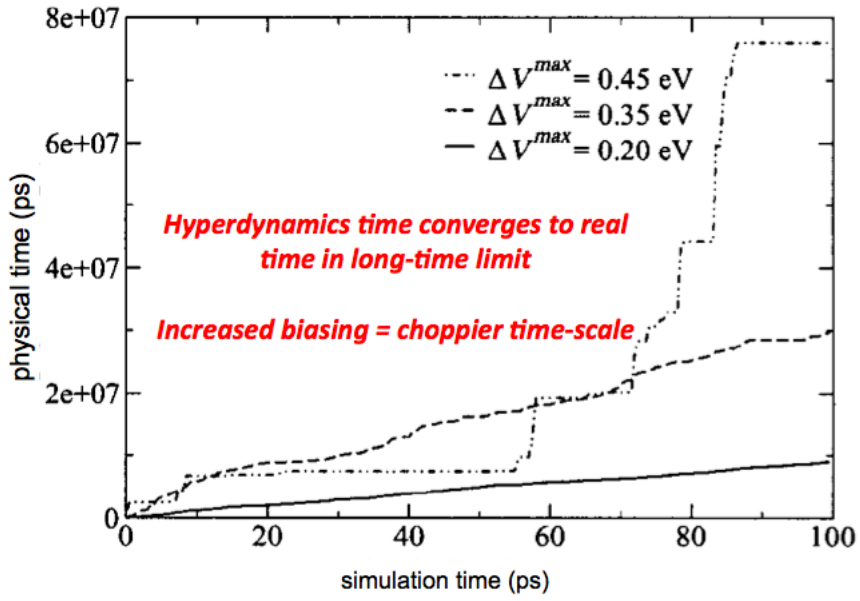

Figure 4.3: Increased biasing (inherently sought for speed-up of simulation) leads to incorrect time-scales. Figure from Miron and Fichthorn using their bond-boost scheme [52] of biasing the potential.

simulates thermodynamic equilibrium, executing transitions with the correct transfer rates, only that one needs to know-before hand what these transitions are. KMC can not actually predict these transitions (something for which we rely on MD), and their *a priori* knowledge (typically through *ab initio* calculations) is necessary. The reliance on pre-knowledge of transitions can become rather prohibitive in many cases, such as highly disordered solids. On this note, several workers have been recently making effort to design algorithms that can predict transition pathways *on-the-fly* as the simulation progresses, such as the on-the-fly KMC method [53].

4.2.3 Parallel replica dynamics

This involves running several replicas of the system in parallel while waiting for transition from one energy well to another to happen [44]. Each replica runs on a different processor. Once transition is recorded on some processor **P**, all the processors are stopped, and the run is restarted by creating replicas of the state one obtained after transition on the processor **P**. Theoretically the algorithm achieves an enhancement in the time-scale that is linearly proportional to the number of replicas used. There are however problems in using this technique for large systems (more than a few hundred atoms) where transitions start becoming too frequent, thereby leading to prohibitively large overhead time.

4.2.4 Temperature accelerated dynamics

This approach does not require a biasing potential as in Hyperdynamics, but it makes the additional approximation of harmonic transition state theory [45]. The central idea is to let the system evolve at a higher temperature, causing transitions to occur more rapidly. The rates so-obtained are however incorrect (or correct only at the elevated temperature), and they are extrapolated back to the temperature of interest by assuming that the rates follow an Arrhenius dependence on the temperature. No prior information on possible mechanism is needed. But one has to be careful that the transition found to be occurring at high temperatures might not be the preferred

transition or might not even occur at low temperatures, and hence a whole catalog of prospective transitions (that could happen at low temperature) needs to be built. Once the escape events at higher temperature are identified, the algorithm involves doing nudged elastic band calculations to find the saddle point energy for each escape event [16]. This knowledge is needed for the correct extrapolation of the rates.

4.2.5 Metadynamics and related methods

Metadynamics [42] assumes that the transitions in a system can be described by a few collective coordinates - for instance, bond length in a chemical reaction. The energy wells in this collective coordinate space are identified, and positive Gaussian potentials are added to these, thereby discouraging the system to revert back to these wells.

One obvious criticism of Metadynamics is that it is difficult to come up with obvious collective coordinates in solid state systems, and as such the related Autonomous Basin Climbing method involves filling up the free energy wells in configuration space itself [54]. Much recent effort has also gone into defining correct collective coordinates for complicated systems, for example glasses. for instance, it has been pointed out in Ref. [55] that trying to describe the system in terms of such collective coordinates can be perilous, and the dynamics can be sensitive to the exact choice of collective coordinates.

4.2.6 κ-dynamics

κ-dynamics is another recently proposed accelerated dynamics method [46] that involves following trajectories beginning from an energy well (using forward flux sampling) until the first successful trajectory is found that has crossed a transition surface and thus per definition reached another well (but without recrossing the transition surface). Once such a transition is identified, the simulation is restarted from the new state. One key limitation of this method is the need to identify a reaction coordinate that separates *reactants* from *products*. The transition state surface also needs to be

well defined.

4.3 Hybrid deterministic and stochastic approach for long time scale MD simulations

We now propose a hybrid method that combines the strengths of MD and MC simulations in a novel way (refer to Figure 4.4). Our approach builds upon the crucial insights of Voter and co-workers while seeking improvements along two important dimensions:

- First, it bypasses a fundamental trade-off present in hyperdynamics: A shallower potential well provides faster dynamics but, at the same time, reduces the ability of the modified potential to properly thermalize the system in between the infrequent events, resulting in artificial correlation between these events.
- Second, our method provides better independent control over the accuracy of the time scale correction, while the hyperdynamics time scale estimates can remain noisy up to long simulation times, especially for large system sizes (see Ref. [52] for a discussion on this, also see Figure 4.3).

Let the state of the system be characterized by position x and velocity v, each being a $3N$-dimensional vector for a system of N atoms. When the system potential energy goes below V_0, we allow MD to continue until the system has lost memory of how it entered this well $\mathbf{W}$ (defined as all points x such that $V(x) \leq V_0$). We found that a simple and appropriate criterion to check for this memory loss is when the energy reaches the system's mean energy at that temperature (although other choices are possible, such as letting MD continue for a sufficiently long, user-specified, time or for a random length of time drawn from a user-specified exponential distribution). During this thermalization time, the system may escape the well, in which case the system simply keeps evolving via MD. Most likely, however, the system will not escape the well during that time. When the mean energy is reached, we stop MD and launch

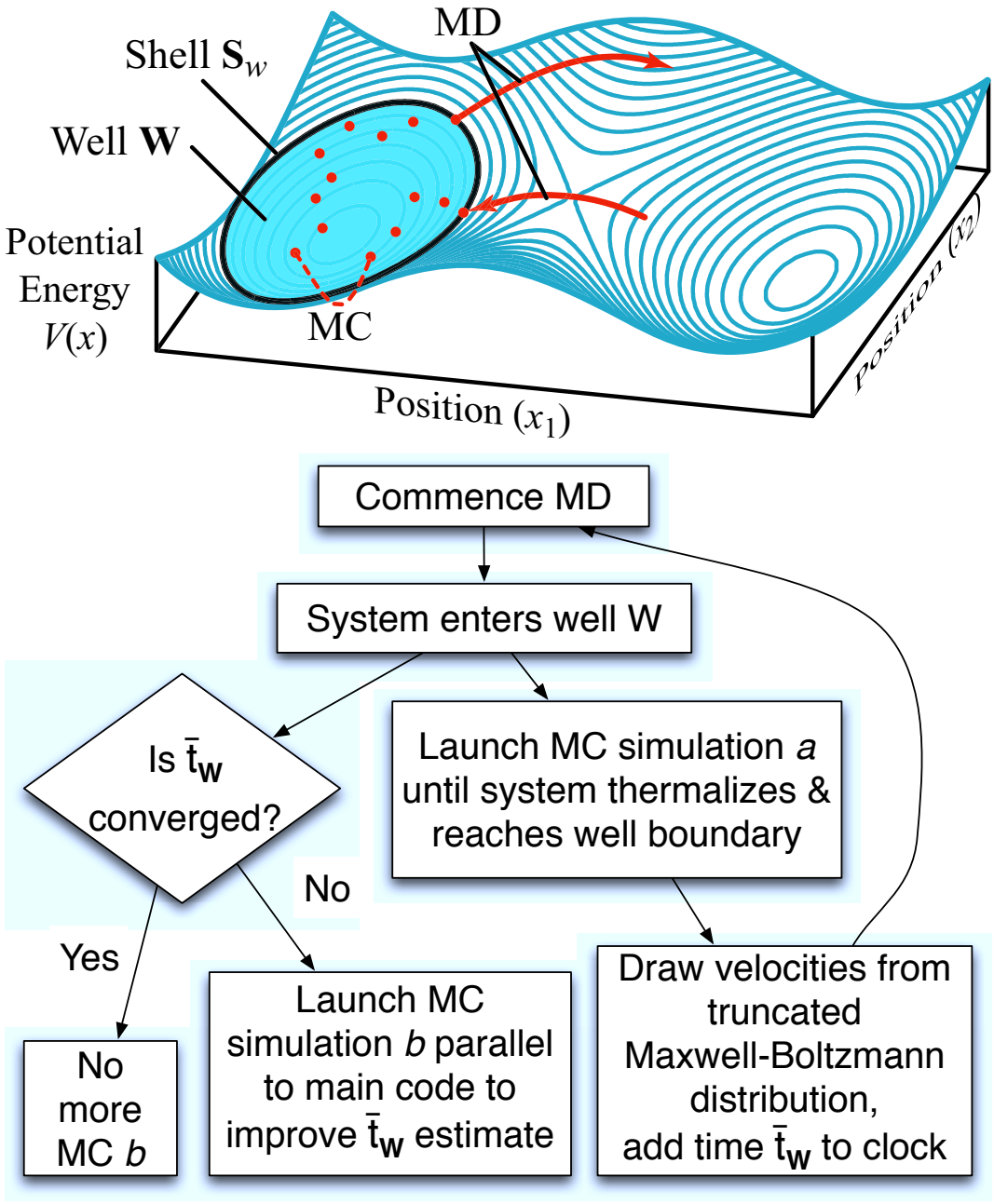

Figure 4.4: Schematic and flowchart of the algorithm. Shell $\mathbf{S}_w$ of constant potential energy and energy well $\mathbf{W}$ as described in text are shown here. See Eq. (4.7) for definition of $\bar{t}_{\mathbf{W}}$.

the first MC simulation (called MC a) on the same processor as on which MD was running, and on parallel processors, a second MC simulation (denoted MC b).

4.3.1 2 kinds of MC simulations

As described above, once we know that the MD routine has entered the well **W**, we stop MD and launch two kinds of MC simulations. We now describe the details of these two MC simulations.

4.3.1.1 MC simulation a: For thermalizing the system

MC a is the first type of MC simulation. It runs with a perfectly uniform potential inside the well, rejecting all moves that lead to $V(x) > V_0$. The purpose of MC simulation a is to generate a new, properly thermalized, starting point for MD. MD resumes with positions drawn from the last MC a step that visited the boundary of the well (defined rigorously in Eq. (4.2)), and velocities drawn from a Maxwell-Boltzmann distribution in the half space pointing outward of the well. V_0 can be picked high or low depending on the speed-up relative to MD we seek for a particular application. The method is formally correct for any choice of V_0; a higher choice of V_0 limits our ability to monitor the detailed dynamics of some events. In Chapter 6 we do a detailed analysis of the dependence on particular choice of V_0.

Simulation a is run until the system is well thermalized and has lost memory of how it entered the well (this takes a few MC passes, an insignificant amount of wall clock time). MD then resumes with positions drawn from the last MC state that visited the boundary of the potential well. The vector v of the velocities of all atoms for restarting MD is drawn from a Maxwell-Boltzmann distribution corresponding to the temperature T of interest, conditional on $v \cdot \nabla V(x) > 0$ (i.e. we only consider velocities in the half-space pointing outwards of the well).

MC simulation a is first of the crucial differences between our approach and hyper-

dynamics: It ensures proper thermalization of the system between rare events even when using a completely flat potential in the well. Even though it is done with a uniform potential, it does not lead to the molecular structure being completely lost since we rule out all moves that lead to energy higher than V_0.

4.3.1.2 MC simulation *b*: For estimating time-scale correction

In parallel to simulation a, another MC simulation b is launched to estimate the mean time the system should have spent in the well **W**. Akin to simulation a, b also rejects all moves that land outside the well **W**. The mean time spent in **W** is given by the reciprocal of the flux exiting [56] the well **W**:

$$t_{\mathbf{W}} = \lim_{w \to 0} (\langle \frac{\overline{v}}{w} \, 1(x \in \mathbf{S}_w) \rangle)^{-1} \tag{4.1}$$

where the average $\langle \cdots \rangle$ is taken over x drawn from the well **W** with a probability density proportional to $e^{-V(x)/(k_B T)}$, where k_B is Boltzmann's constant and the following definitions hold: $1(A)$ equals 1 if the event A is true and 0 otherwise, $\mathbf{S}_w$ is a shell of width w at the boundary of the well **W** (see Figure 4.5), which can be defined in the limit of small w as

$$\mathbf{S}_w = \{x : |V(x) - V_0| \leq w |\nabla V(x)|/2\} \tag{4.2}$$

and $\overline{v}$ denotes the mean projection of a Maxwell-Boltzmann-distributed velocity along the unit vector u parallel to $\nabla V(x)$, conditional on $v \cdot u > 0$. The latter is given by

$$\overline{v} = \sqrt{\frac{k_B T}{2\pi} \sum_{i=1}^{N} \frac{|u_i|^2}{m_i}} \tag{4.3}$$

where m_i is the mass of atom i and $|u_i|$ denotes length of the 3 dimensional subvector of u associated with atom i. Note that the Eq. (4.3) reduces to the familiar expression [56] $\overline{v} = \sqrt{k_B T / 2\pi m}$ when all atoms have the same mass, in which case $\overline{v}$ factors out of the average in (4.1).

4.4 Refinements to the basic algorithm

The times $t_{\mathbf{W}}$ obtained via MC simulations b can be directly added to the physical time spent doing MD simulations to yield the overall physical time of the simulation. Note: What is actually added to the clock is an exponentially distributed random number with mean $t_{\mathbf{W}}$ given by:

$$t = ln(1/r) \times t_{\mathbf{W}} \tag{4.4}$$

where r is a random number drawn from a uniform distribution on (0,1].

However, more refinements of the method can yield further improvement in efficiency. We describe some such refinements now. Some more $not - so - obvious$ refinements will be described in the next chapter.

4.4.1 Biasing the energy landscape for faster estimation of time-scale correction

Since Eq. (4.1) involves an average, it can be approximated by MC simulations. However, the most straightforward implementation of this approach would be very inefficient because x would rarely visits the boundary $\mathbf{S}_w$ of the well. The efficiency can be considerably improved by using a biased potential $V^*(x)$ which is the same as the real potential in the high-energy regions (i.e. regions outside well $\mathbf{W}$ with $V(x) \geq V_0$), but lifted up in the deep energy basins (as in Figure 4.2). With this Eq. (4.1) becomes

$$t_{\mathbf{W}} = \lim_{w \to 0} \frac{\langle e^{-\beta(V(x)-V^*(x))} \rangle^*}{\langle \frac{\overline{v}}{w} e^{-\beta(V(x)-V^*(x))} 1(x \in \mathbf{S}_w) \rangle^*} \tag{4.5}$$

where the averages $\langle \cdots \rangle^*$ are taken over x drawn from the well $\mathbf{W}$ with a probability density proportional to $e^{-V^*(x)/(k_B T)}$ and $\beta = 1/k_B T$. MC simulation b is the second

main difference with hyperdynamics: It provides separate control over the accuracy of the speed up factor since the length of the MC simulation b can be adjusted independently of the length of the whole simulation.

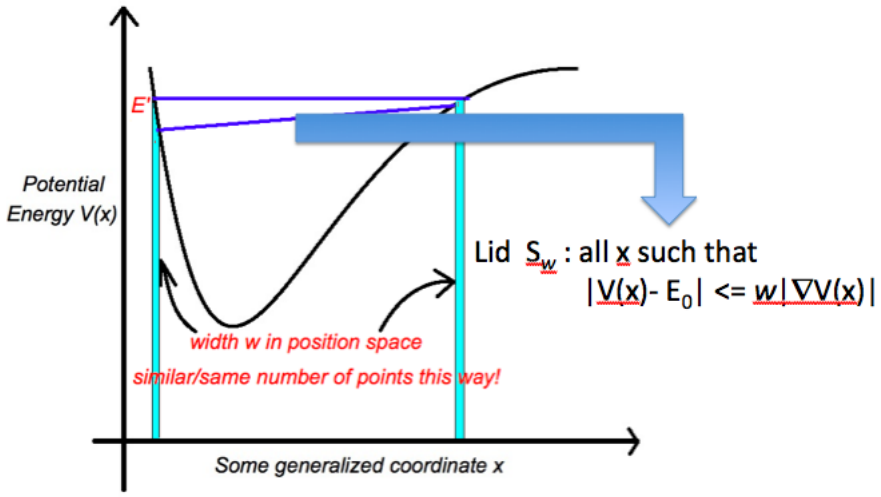

Figure 4.5: Illustration of the energy shell $\mathbf{S}_w$ as defined in Eq. (4.2). By defining the shell this way we ensure that it contains similar number of points in the configuration space irrespective of the gradient of the potential energy landscape.

The form of biasing we use in this chapter is a well established and easy to implement biasing potential used in several implementations of Voter's hyperdynamics method, originally proposed by Hamelberg *et al.* [47]:

$$V^*(x) \;=\; V(x) + \begin{cases} 0 & V(x) \geq V_0 \\ \frac{(V_0 - V(x))^2}{\alpha + V_0 - V(x)} & V(x) < V_0 \end{cases} \tag{4.6}$$

4.4.2 Averaging time over all wells without distinguishing between the *types* of wells

Instead of computing $t_{\mathbf{W}}$ for each well $\mathbf{W}$, one may keep a running average

$$\bar{t}_{\mathbf{W}} = \frac{1}{n_{\mathrm{b}}} \sum_{W} t_{\mathbf{W}} \tag{4.7}$$

of the time spend in the n_b wells sampled via MC simulation b (n_a, the number of wells actually visited, may well far exceed n_b). Once this average is converged, there is no need to initiate MC simulation b anymore. The overall time spent in all the wells will simply be $\bar{t}_{\mathbf{W}} * n_a/n_b$. Note that there is no need to keep separate averages for different types of wells, which would have been difficult to implement. Although MC simulations a still need to be performed for all wells, the quantity in Eq. 4.7 converges much more rapidly.

4.4.3 *Quick* and *dirty* evaluation of the time-scale correction

Other efficiency improvements can be obtained by not performing fully converged MC simulations b and exploiting the fact that errors will average out over wells in Eq. (4.7). Also, given the embarrassingly parallel nature of the algorithm, the Ergodic Hypothesis can be invoked and the simulation MC b can be launched on as many processors as available thereby improving the quality of estimate without having to wait for long simulation times. Note that this scheme must be used while ensuring that the biasing potential is sufficiently strong so that most of the random errors in Eq. (4.5) are concentrated in the numerator, to avoid a systematic bias due to nonlinearity of the ratio.

4.4.4 Optimum extent of biasing

To minimize the wall-clock time needed for calculation of time in Eq. (4.5) via simulation b, we use an optimal extent of biasing as suggested in Ref. [47]. This involves setting $\alpha \simeq V_0 - V_{min}$ which allows the biased potential to capture the shape of the potential wells [47]. α smaller than this would improve sampling of the numerator in Eq. (4.5) but deteriorate that of the denominator.

4.5 Some comments and comparison with Hyperdynamics

We would like to point out that only the parameter w is additional to those in any typical hypderdynamics scheme (Hamelberg *et al.* [47]'s in this case), the choice of which does not effect the result since we extrapolate $t_{\mathbf{W}}$ to the limit of small w [56]. Our approach compares favorably with hyperdynamics [41] where one does not have control over the accuracy of the accelerated time (hyperdynamics relies on this error cancelling out over time but does not provide an estimate of how much it is [41, 52]), and one is obliged to keep performing dynamics with the biased potential at all stages of the calculation. Thus our method offers boosts as high as those that one could get from setting $\alpha = 0$ in Eq. (4.6) (akin to the flooding scheme [57, 58]), but still avoiding the slow convergence in time and problems with discontinuous forces that one encounters in implementing flooding based hyperdynamics. In addition we avoid errors from sampling the system in the state when it is not thermalized between two rare events - once MD is relaunched in our scheme, the system is well thermalized by virtue of simulation *a*.

The main advantages of this new method over existing accelerated MD techniques (see, for e.g., [40, 41, 46, 59]) are that (i) it provides a statistically more accurate "real" time scale (which is important when determining the actual strain rate in a simulation and time-dependent forces in general), (ii) it does not rely on transition state theory (which is important when the object of interest is the entropy of activation or migration), (iii) it does not require the specification of the degrees of freedom of interest or specific reaction coordinates as in Ref. [42, 46] (which is crucial when the mechanisms are complex and involve the movement of many atoms) and (iv) the efficiency of estimating the "real" time scale (as in (i)) improves linearly with number of computer processors employed for the calculation.

One possible source of inefficiency (from the perspective of computational time)

in our method is the waiting period allowing the mean energy of the system to be attained before relaunching MC simulation a. This however is not a very long period of time (few picoseconds or less), and it helps us ensure that the transition (if it happened) if not undone by recrossing.

4.6 Validation of the method

We picked two problems to demonstrate that our method yields correct dynamics: (a) vacancy -mediated diffusion in BCC Fe at room temperature, and (b) deformation behavior in Au nanopillars at realistic strain rates.

4.6.1 Lattice diffusion in BCC iron at low temperatures: Is the speeded time correct?

Lattice diffusion at low temperatures is beyond the time scales one can access in current MD simulations, with most investigations [60] only beyond 700 K. The system we consider is 249 Fe atoms (5x5x5 BCC supercell with 1 vacancy) interacting through the Embedded Atom Method (EAM) potential [60]. For the MD part here and in deformation behavior problem, we performed NVT (constant number, volume, temperature) simulations using time step of $2\text{x}10^{-15}$ sec and a Langevin thermostat with coupling constant $1\text{x}10^{-11}$ sec^{-1}. The biasing parameter α was 50 eV. The V_0 values we used at 500 and 300 K were -975.5 eV and -984 eV resp. (4 and 2.5 eV more than the mean energy at 500 and 300K resp.). We took the equilibrium concentration of defects [60] to convert our effective diffusivity into equilibrium diffusivity. In Figure 4.6 we plot the equilibrium diffusivity as obtained from (a) MD simulations [60],(b) our proposed approach, and (c) experimental measurements [61] that include contributions from interstitial migrations also and hence are only slightly higher than both ours and MD values. We obtain around 5 orders of magnitude boost, with similar speed up factors for system sizes up to 30000 atoms.

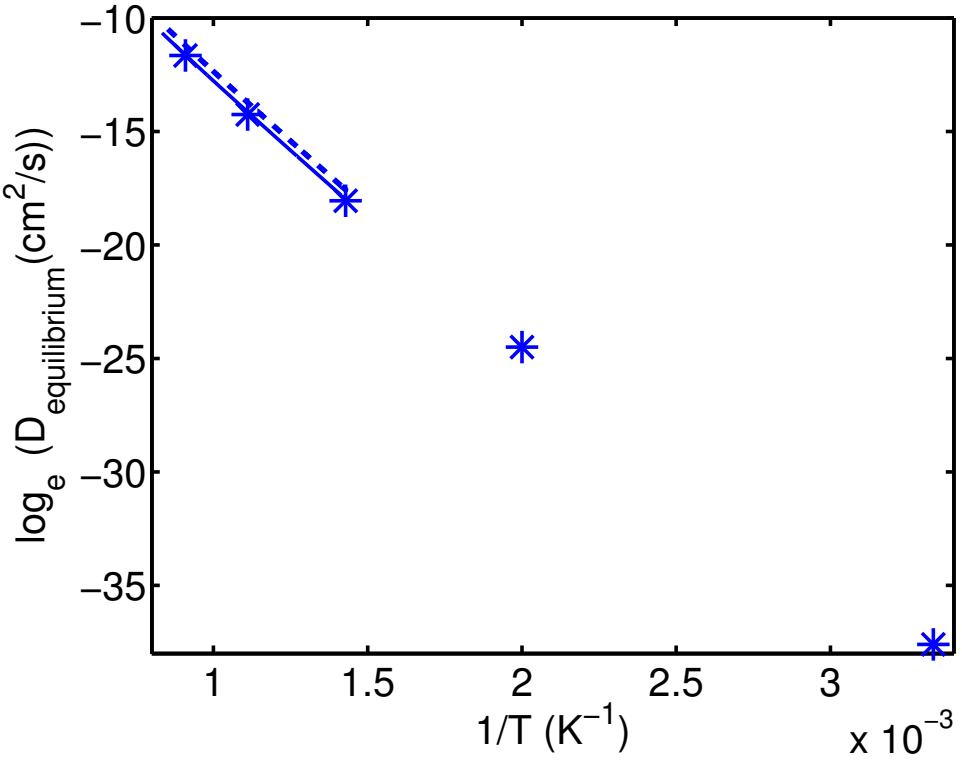

Figure 4.6: Diffusivity at various temperatures. (a) Straight lines denote Mendelev *et al.*'s [60] MD calculations. These are valid only until 700 K. (b) Asterisks denote diffusivity measurements per our approach. (c) The dashed line shows experimental measurements [61] valid between 1000 and 1200 K.

4.6.2 Compression tests on nanopillars under low strain-rates: Are correct deformation mechanisms predicted?

For our second problem (see Figure 4.7), we looked at deformation behavior of Au nanopillars. With advent of excellent *in situ* TEM and HRTEM tools, there are many elegant experiments on sub-10-nm sized crystals [62–64]. Deformation in such small sizes is controlled by dislocation nucleation, and has been phenomenologically predicted [65] and experimentally found [62–64] to have small activation volumes and strong strain-rate sensitivity. However there is no direct MD based confirmation of this strong strain-rate sensitivity due to inability of MD to reach strain rates lower than 10^7/sec.

Using our method we were able to reach 10^3/sec strain-rate regime with only around 48 hours of computer time. We could also obtain several correct qualitative and quantitative aspects of the deformation dynamics, without assuming anything about the nature of deformation. In this section we provide a brief summary of the key results.

4.6.2.1 Specifications of the system

The system we consider is 2016 Au atoms (cylinder with height 7.4 nm and diameter 2.5 nm) interacting through EAM potential [68]. The biasing parameter α was 1500 eV while the starting V_0 value used was -7266 eV(8 eV more than the mean energy at 300K), adjusted every 1000 MD steps to take into account the pressure-volume work contribution from the stress. The cylinder was initially carved out from perfect FCC lattice (Figure 4.7(a)). Periodic boundary conditions were imposed only along the cylinder axis z which is the same as the compression axis $\langle 001 \rangle$. The cylinder was first equilibrated for 500 ps before beginning the compression carried out by uniformly re-scaling the z-coordinates of all atoms. The atomic virial stress [69] was used to obtain the Cauchy stress.

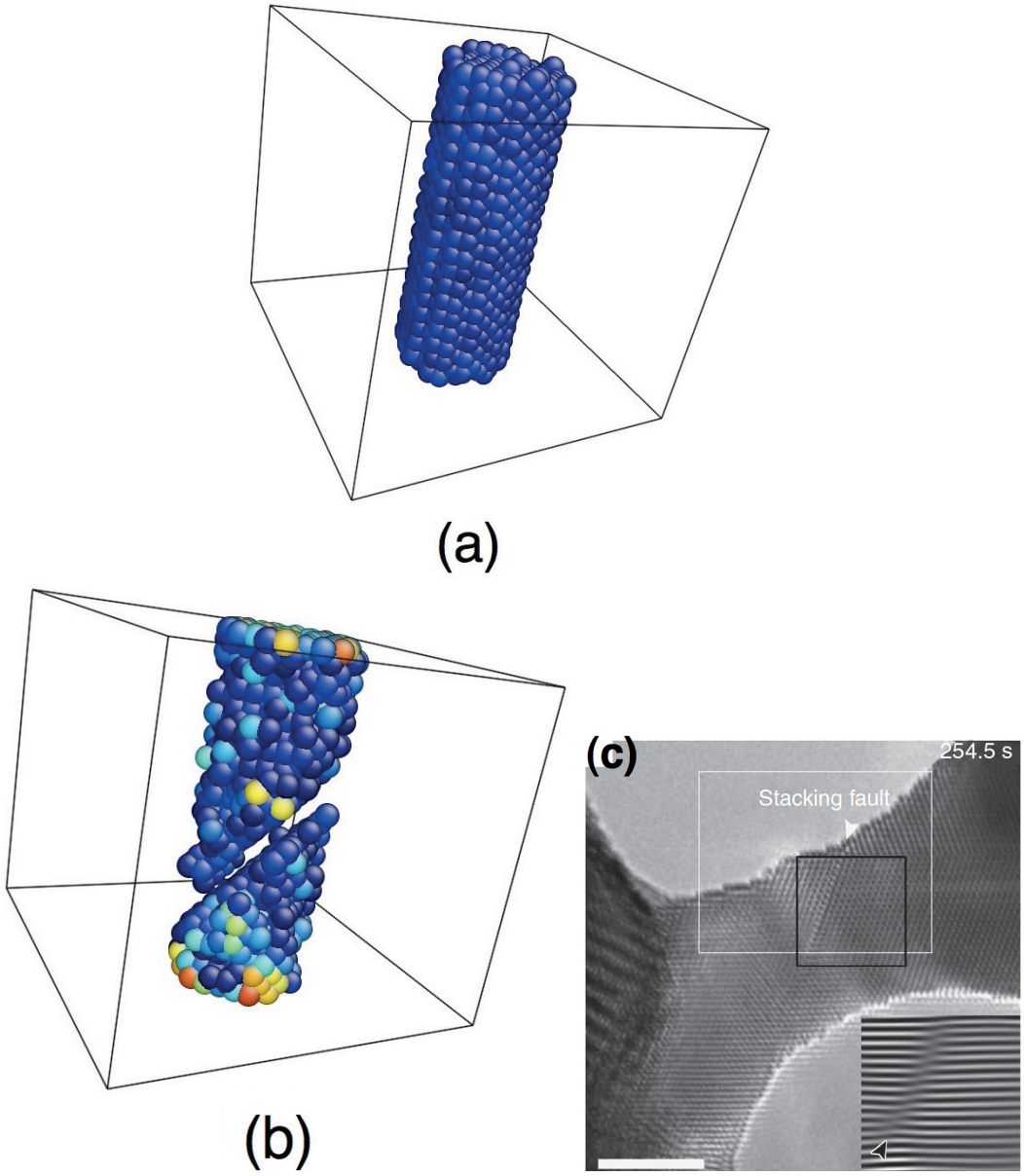

Figure 4.7: (a) and (b) illustrate simulation cell for stress-strain calculations. Coloring is as per bond order parameter Q_6 [66,67], with blue denoting FCC, and perfect HCP atoms removed for clarity. Other colors denote non-12 coordinated atoms. (a) Prior to application of any strain, (b) after yielding (strain = 12%) with strain rate = 10^3/sec. In (b) the leading partial has nucleated on {111} slip plane leaving behind the 2-layer thick HCP region denoting an intrinsic stacking fault. Failure is thus through slip and not twinning, in agreement with HRTEM experiments as shown in (c) taken from Ref. [62].

4.6.2.2 Results

In this chapter, 4 different strain rates $\dot{\epsilon}$ were considered: 5x10^6/sec, 2.5x10^6/sec, 5x10^5/sec and 5x10^4/sec (we present results for 10^3/sec strain-rate in Chapter 5). We present the resulting stress(σ)-strain(ϵ) plots in Figure 4.8(a). Several conclusions can be drawn from Figs. 4.7 and 4.8 that prove our algorithm capable of predicting correct dynamics in complicated systems. The yielding occurs around 10% strain, and is through slip and not twinning or elastic instabilities: a leading partial nucleates on a {111} slip plane at lower stresses than a trailing partial. This can be seen in Figure 4.7(b) where the leading partial nucleated from the surface and left behind a 2-layer thick HCP region which again changes back to FCC after the trailing partial also nucleates at higher stresses and recombines with the leading partial. Figure 4.7(b) is identical to HRTEM images for $\langle 001 \rangle$ loading of Au nanowires [62]. The strain rate sensitivity m in the relation $\sigma = \sigma_0 \dot{\epsilon}^m$ (derived by looking at stress at 11% strain) is around 0.14±0.07 (see Figure 4.8(b), while Ref. [64] reports it to be around 0.11 for 75 nm diameter pillars. The activation volume Ω for the deformation as calculated through [64] $\Omega = \sqrt{3} k_B T \partial(lg\dot{\epsilon})/\partial\sigma$is around $1b^3$ (b=burgers vector) in excellent agreement with experiments observations [64, 65].

4.7 Summary

To summarize, we have proposed a hybrid deterministic and stochastic approach that combines the strengths of MC and MD simulations in a unique yet easy to implement scheme, thus offering boosts of several orders of magnitudes with good system size scaling. We have applied the method to study lattice diffusion in BCC Fe at low temperatures and deformation of Au nanopillars at strain rates hitherto unachievable and found it to work really well in both cases, predicting correct dynamics and exhibiting good scaling with increase in system size from 249 to 2016 atoms. We thus expect the method to be useful in a variety of situations. In the next chapter we will introduce more algorithms that build upon the efficiency of the basic idea presented

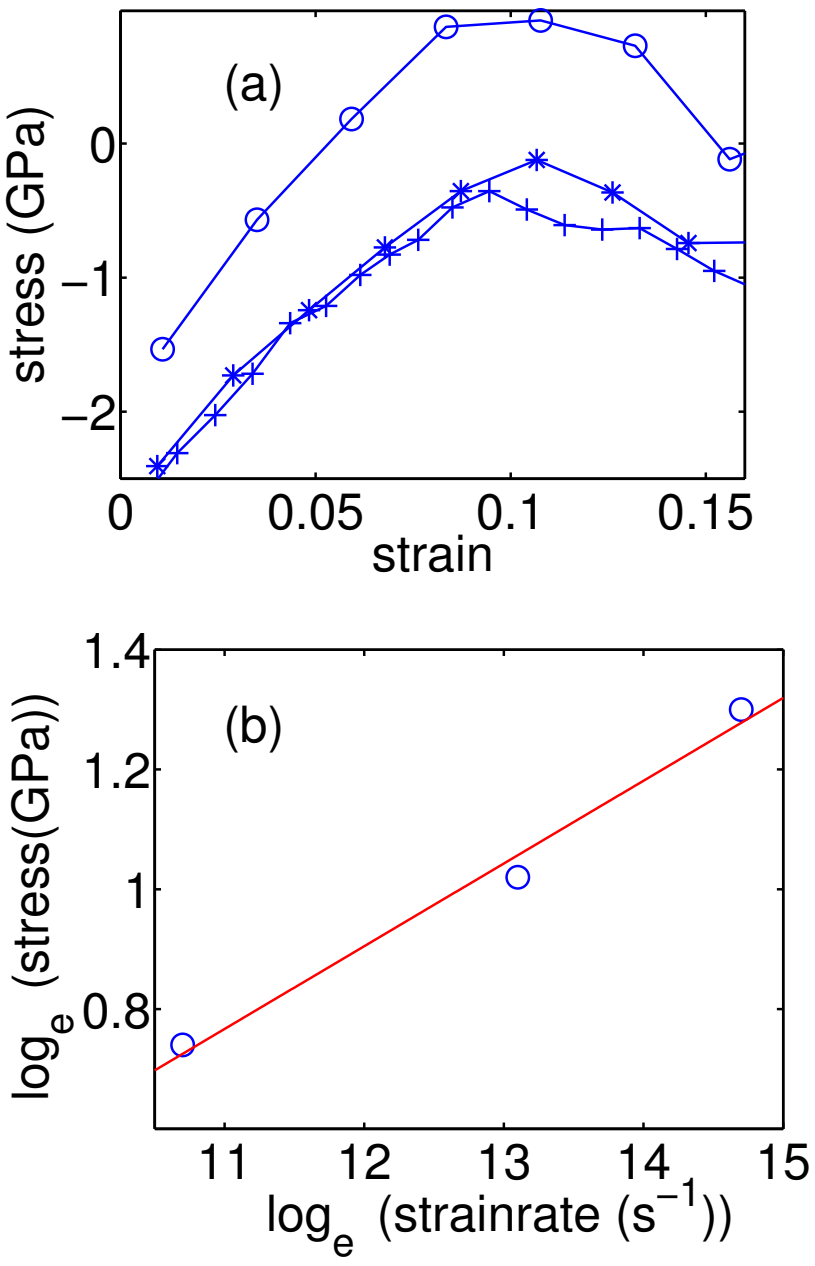

Figure 4.8: (a)Stress-strain plots for 2.5 nm diameter Au nanopillar at 3 different strain rates: 2.5x10^6/sec (open circles), 5x10^5/sec (asterisks), 5x10^4/sec (pluses). The initial stress corresponding to zero-strain is non-zero due to surface effects [69]. (b) log-log plot of stress at 11% strain (relative to surface stress at zero strain) versus strain rate.

in this chapter. We then also provide a more detailed application of the method.

Chapter 5

Realistic time-scale fully atomistic simulations of surface nucleation of dislocations in pristine nanopillars

5.1 Motivation

In the previous chapter we proposed a hybrid MC-MD algorithm to achieve realistic time-scales while still maintaining fully atomistic resolutions. The algorithm was validated for vacancy assisted diffusion and for low-strain rate tensile tests. In this chapter, we address a limitation fundamental to our algorithm as proposed in the previous chapter and in fact to all related accelerated dynamics algorithms. We also apply the method to investigate surface nucleation of dislocations in pristine nanowires. We thus demonstrate that our method is capable of achieving extended time-scales, while still predicting correct mechanisms involving concerted motion of several atoms (nucleation of partial stacking fault in this chapter).

Forming a correct picture of dislocation nucleation is central to our understanding of deformation mechanisms at the nanoscale. The initial discoveries by Uchic and subsequent work by various groups [63, 64, 70–76] have now established that there is a marked increase of yield strength as the specimen size decreases, with significant strain-rate dependence as well. These observations have generally been attributed to the scarcity of dislocation sources (such as Frank-Read sources) in nano-sized samples,

and having to nucleate dislocations in a perfect crystal (perfect apart from presence of surfaces) [77–80]. As such there have been numerous attempts to link simulations of dislocation nucleation processes to experimentally observed mechanical behavior - in fact a lot of crucial insight has come from simulations [65,81–87]. Nanoindentation experiments [88–90], Scanning Electron Microscopy combined with Nanoindentation [91], and High Resolution Transmission Electron Microscopy (HRTEM) [62] are now sufficiently advanced for one to hope for a direct match between simulations and experiments [62, 92–94]. However, the time-scale disparity between experiments and simulations is a pressing limitation here and that is the concern we address in this chapter.

5.2 Introduction

5.2.1 Methods for modeling nanomechanics

There are three broad classes of techniques for such simulations, often used in conjunction with each other and along with approaches such as Transition State Theory: Classical molecular dynamics, continuum based methods and *ab initio* techniques. *Ab initio* simulations, though they often provide insight into mechanical behavior [95–99], are still restricted to very small sizes, less than a hundred atoms typically (although there are several promising attempts at bridging this length-scale gap for *ab initio* calculations [100–103]). The achievable time-scales are also typically restricted to less than a few picoseconds. Continuum based methods are another elegant option capable of dealing with a variety of length and time scales, though they suffer from not providing atomic scale resolution and assuming elastic behavior even at dislocation cores [104–106]. Classical molecular dynamics can be helpful in gaining quantitative insight into mechanical behavior at various length scales (nanometers to microns or larger) [69,76,107–110]. MD does not assume much apart from the form of interatomic interaction, which is typically developed by fitting to first principles or experimental data. The availability of quality interatomic force-fields [68, 69, 111, 112] and increase

in computer power has led to a tremendous increase in the popularity of MD over the last decade.

5.2.2 Time-scale problem

However, most of the interesting dynamics happens only as the system moves from one energy basin to another through infrequent, rare events. Most of the simulation time gets spent with the system staying stuck in some energy basin [42]. This behavior, combined with the femtosecond timestep required for total energy conservation, gives rise to a major limitation of MD: The time-scale problem [40, 113, 114]. Even with the advent of powerful super-computers, MD simulations are unable to reach more than a few nanoseconds of time if the system size is more than a few hundred atoms. Thus while laboratory strain-rates are typically in the range 10^{-5}-10^{3}/sec, with corresponding activation free energies being around $30k_BT$, MD is unable to go slower than 10^{7}/sec strain-rate, corresponding to free energies of around $5k_BT$ or lower [65, 87, 115, 116]. One approach to get around this shortcoming is to perform 0 temperature Nudged Elastic Band calculation [16] of the activation free energy and how it varies with applied stress, and then either assume it to be temperature independent, or assume a phenomenological model for its variation with temperature (such as multiplying it with an empirical temperature dependent scaling factor) [106]. These approaches can sometimes work well, but as shown by [87, 115] and in this current work, can sometimes lead to significant inaccuracies in the predictions, such as errors of several orders of magnitude in the nucleation rate, or even qualitatively incorrect phase transitions [117].

5.2.3 Temperature dependence of activation free energies of dislocation nucleation under realistic loads

It has remained an unsolved problem so far to design and perform fully atomistic simulations that could provide a picture of temperature dependent activation free energies of dislocation nucleation from surfaces at realistic loads and loading rates. Such a picture is key to linking experimental results with simulation predictions [87,106,117]. The critical nucleus for surface nucleation can be as small as a few atomic planes, thus questioning the applicability of continuum methods. As for classical MD, the time-scale achievable is several orders of magnitude smaller than experiments, thus limiting MD simulations to regimes of extremely high nucleation rates. With our recently proposed hybrid MC-MD method that allows us to achieve extended time-scales while still maintaining atomistic resolution, we are able to study the temperature dependence of activation parameters for surface nucleation of dislocations in pristine nanowires and obtain several significant results in an activation regime actually achievable in laboratory experiments. The specific problem we consider pertains to several nano-indentation experiments where it was found that even if the applied stress on a sample is in the elastic regime, yielding could occur after a certain statistically distributed waiting time [118–120]. We perform fully atomistic simulations of this time-dependent incipient plasticity behavior in gold nanowires, reaching hundreds of milliseconds time-scales for several thousand atoms. After collecting statistics for various temperatures and applied stresses, we then derive the full picture of stress and temperature dependence of the activation free energy.

In this Chapter we apply our algorithm from Chapter 4 to study in detail the problem of dislocation nucleation under realistic driving forces. We also propose a new adiabatic switching technique that significantly reduces the number of input parameters in our hybrid MC-MD approach and eliminates some of the fundamental limitations of our earlier implementation (that were shared by related algorithms [41]). The algorithms employed here make it possible to achieve linear scaling in efficiency

of estimating the accelerated time as the number of parallel processors employed is increased. We describe our algorithm and its implementation in sufficient detail for researchers to be able to use it for their problem of interest, and hope that it will be found helpful for modeling a variety of mechanical behavior problems.

5.3 Details of calculations

5.3.1 Choice of interatomic potential

There are several good potentials available for modeling mechanical behavior of gold [68, 111, 121, 122]. The embedded atom method potential proposed in Ref. [68] gives very realistic values for the surface energy and the stacking fault energy [69]: The stacking fault energy from the potential by [68] is 42 mJ/m^2 while the experimental value for it is in the range 32-46 mJ/m^2. Since the current chapter deals with nucleation of dislocations from surfaces, we choose the Grochola potential. This potential was also used and found to perform very well in a recently published joint computational and experimental work studying dislocation behavior in sub-10nm gold nanowires [62]. Ref. [69] provide a critical comparison of this potential with other available potentials for various physical properties relevant to the current work.

5.3.2 Hybrid stochastic and deterministic technique for achieving realistic time-scales

5.3.2.1 Summary of ideas

In Chapter 4 we proposed using a combination of MD and MC techniques for achieving long time scales [116]. Our approach is built upon minimizing the MD time spent in low-lying energy basins, and instead using 2 kinds of MC simulations. One (a) seeks to properly thermalize the system between infrequent events, thereby minimizing artificial correlations, and the other (b) provides independent control over the

accuracy of the time-scale correction. When the potential energy $V(x)$ of the system (where x is a point in the 3-N dimensional configuration space for a system with N particles) is above a certain V_0, the system evolves as per regular MD (see Figure 4.4). This high-energy region of the phase space is the one containing the interesting but infrequent events. When the system potential energy goes below V_0, we allow MD to continue until the system has lost memory of how it entered this well (defined as all points x such that $V(x) \leq V_0$). In Chapter 4 we proposed a simple and appropriate criterion to check for this memory loss: When the energy reaches the system's mean energy at that temperature .

We also need to estimate the expected value of the time the system would have spent in the energy well $\mathbf{W}$, which can be calculated as the reciprocal of the flux exiting the well:

$$t_{\mathbf{W}} = \lim_{w \to 0} (\langle \frac{\overline{v}}{w} \, 1(x \in \mathbf{S}_w) \rangle)^{-1} \tag{5.1}$$

We discussed details of the terms in the above equation in Chapter 4.

Since Eq. (5.1) involves an average, it can be approximated using MC simulations. We make use of the system's ergodicity, replacing the time average (that would require us to wait for long times for it to converge) by an ensemble average. Thus in parallel to MC a, we launch several instances (as many as number of available processors) of a second kind of MC simulation, called MC b, to estimate the time-scale correction. A most straightforward implementation of this still won't be as effective in estimating the average in Eq. (5.1) because the shell $\mathbf{S}_w$ would be visited very rarely. Thus, to improve the efficiency in estimating Eq. (5.1), we proposed in Chapter 4 using a biased potential $V^*(x)$, which is the same as the true potential $V(x)$ in the high-energy regions but lifted up in the energy basins [40, 41]. Several lifting (or biasing) schemes are available for use in this [40]. A simple importance sampling expression (as detailed in Chapter 4) can thus give us the following time-correction:

$$t_{\mathbf{W}} = \lim_{w \to 0} \frac{\langle e^{-\beta(V(x)-V^*(x))} \rangle^*}{\langle \frac{\overline{v}}{w} e^{-\beta(V(x)-V^*(x))} 1(x \in \mathbf{S}_w) \rangle^*} \tag{5.2}$$

where $\langle \cdots \rangle *$ denote expectations taken under a density proportional to $e^{-\beta V^*(x)}$, in which β is $1/(k_B T)$.

This approach works well, but there is a fundamental trade-off that limits its usefulness. Lifting the biased potential more and more leads to the energy shell $\mathbf{S}_w$ being visited more frequently and should lead to greater computational efficiency in estimating Eq. (5.1). However a compensating effect leads to a decrease in efficiency beyond a certain amount of biasing. This is because increased biasing of the potential leads to noisier statistical averaging of the time in Eqs.(5.1) and (5.2) - as biasing increases, $(V(x) - V^*(x))$ becomes a large number causing $e^{-\beta(V(x)-V^*(x))}$ to dramatically increase. This point has been discussed in detail in [59, 115, 116].

5.3.2.2 Adiabatic switching technique

We now propose a technique that bears some resemblance to adiabatic switching methods that helps us deal with the trade-off discussed above, and also eliminates the need for picking a particular biasing scheme. The motivation here is to avoid the statistical noise in Eq. (5.2) that arises as the biased potential $V^*(x)$ becomes increasingly different from the true potential $V(x)$. To avoid this noise in sampling, the system is continuously, *adiabatically* switched from $V(x)$ (the true potential) to V_0 (a flat potential within the well, identical to the potential used in MC simulation a for thermalization). We now formally derive the method.

Let $\hat{V}(x, \alpha)$ smoothly interpolate between $\hat{V}(x, 0) \equiv V(x)$ and $\hat{V}(x, 1) \equiv V_0$. Then we can express the ensemble average in Eq. (5.1) as below (working in terms

of $rate = 1/time$):

$$\begin{aligned} rate &= \lim_{w\to 0} \frac{\int \frac{\bar{v}}{w} 1\left(x \in S_w\right) e^{-\beta \hat{V}(x,0)} dx}{\int e^{-\beta \hat{V}(x,0)} dx} \\ &= \lim_{w\to 0} \frac{\int \frac{\bar{v}}{w} 1\left(x \in S_w\right) e^{-\beta\left(\hat{V}(x,0)-\hat{V}(x,1)\right)} e^{-\beta \hat{V}(x,1)} dx}{\int e^{-\beta \hat{V}(x,1)} dx} \left(\frac{\int e^{-\beta \hat{V}(x,1)} dx}{\int e^{-\beta \hat{V}(x,0)} dx}\right) \\ &\equiv \lim_{w\to 0} \left\langle \frac{\bar{v} 1\left(x \in S_w\right)}{w} e^{-\beta\left(\hat{V}(x,0)-\hat{V}(x,1)\right)} \right\rangle_1 R \end{aligned} \tag{5.3}$$

where dx denotes a differential volume in 3-N dimensional configuration space for N particles, the integration being performed over entire configuration space within the well **W** and the expected value $\langle \cdots \rangle_\alpha$ in Eq. (5.3) is defined by

$$\langle \cdots \rangle_\alpha = \frac{\int (\cdots) e^{-\beta \hat{V}(x,\alpha)} dx}{\int e^{-\beta \hat{V}(x,\alpha)} dx} \tag{5.4}$$

Below we define the term R in Eq. (5.3) and re-express it in a computationally tractable form:

$$\begin{aligned} R &= \frac{\int e^{-\beta \hat{V}(x,1)} dx}{\int e^{-\beta \hat{V}(x,0)} dx} \\ &= \exp\left(\ln \int e^{-\beta \hat{V}(x,1)} dx - \ln \int e^{-\beta \hat{V}(x,0)} dx\right) \\ &= \exp\left(\int_0^1 \left(\frac{\partial}{\partial \alpha} \ln \int e^{-\beta \hat{V}(x,\alpha)} dx\right) d\alpha\right) \\ &= \exp\left(-\beta \int_0^1 \frac{\int \frac{\partial \hat{V}(x,\alpha)}{\partial \alpha} e^{-\beta \hat{V}(x,\alpha)} dx}{\int e^{-\beta \hat{V}(x,\alpha)} dx} d\alpha\right) \\ &= \exp\left(-\beta \int_0^1 \left\langle \frac{\partial \hat{V}(x,\alpha)}{\partial \alpha} \right\rangle_\alpha d\alpha\right) \end{aligned} \tag{5.5}$$

With this we can now write the rate in Eq. (5.3) as

$$rate = \lim_{w\to 0} \bar{v} \left\langle \frac{1\left(x \in S_w\right)}{w} e^{-\beta\left(\hat{V}(x,0)-\hat{V}(x,1)\right)} \right\rangle_1 \exp\left(-\beta \int_0^1 \left\langle \frac{\partial \hat{V}(x,\alpha)}{\partial \alpha} \right\rangle_\alpha d\alpha\right) \tag{5.6}$$

We now make a few observations regarding the above expression. It involves 3

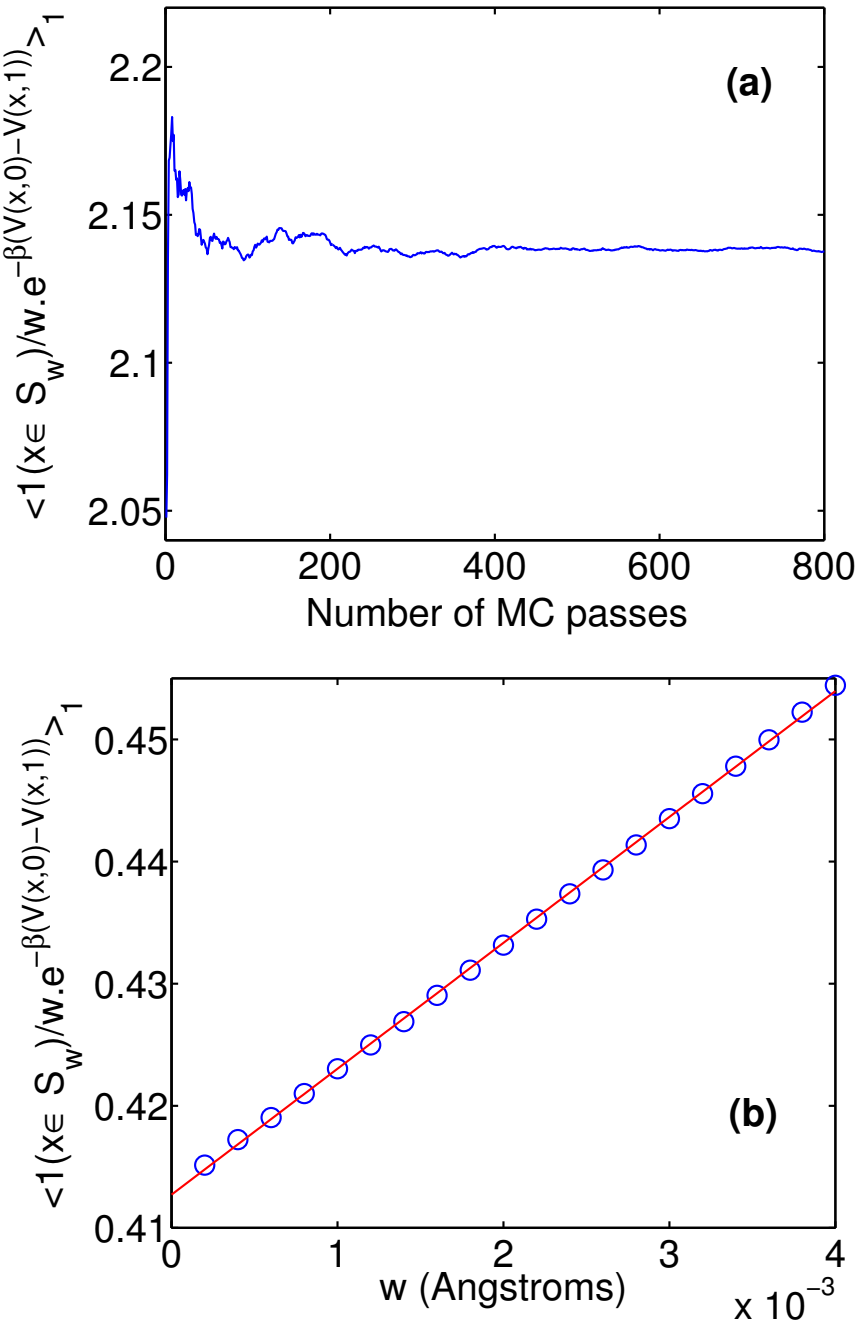

Figure 5.1: (a) The 2nd part in Eq. (5.6), i.e. $\left\langle \frac{1(x\in S_w)}{w} e^{-\beta\left(\hat{V}(x,0)-\hat{V}(x,1)\right)} \right\rangle_1$, can be evaluated in a very small number of MC passes as explained in the text. (b) Calculating $\lim_{w\to 0} \left\langle \frac{1(x\in S_w)}{w} e^{-\beta\left(\hat{V}(x,0)-\hat{V}(x,1)\right)} \right\rangle_1$ using linear extrapolation. Calculations are for a Au nanowire with 2016 atoms, 2.5nm in diameter and 7.5nm in height, at 300 K.

independent parts. The first is $\bar{v}$, which we already know as $\sqrt{k_B T/2\pi m}$ for identical atoms. We could keep $\bar{v}$ inside the ensemble average to cover the general case of unequal masses in which $\bar{v}$ may depend on x. The second part in Eq. (5.6) is $\lim_{w\to 0}\left\langle \frac{1(x\in S_w)}{w} e^{-\beta\left(\hat{V}(x,0)-\hat{V}(x,1)\right)}\right\rangle_1$. This is non-0 only when $x \in S_w$, and whenever it is non-0, the difference $\hat{V}(x,0) - \hat{V}(x,1)$ is a very small number (see Eq. (4.2))). Since this average is calculated with a flat potential $\hat{V}(x,1)$, the boundary $x \in S_w$ is visited frequently, and thus the second term in Eq. (5.6) can be evaluated very quickly - in a few MC passes as shown in Figure 5.1(a). We calculate $M \equiv \left\langle \frac{1(x\in S_w)}{w} e^{-\beta\left(\hat{V}(x,0)-\hat{V}(x,1)\right)}\right\rangle_1$ for a few values of w, and simple linear extrapolation gives the desired limit, as shown in Figure 5.1(b). The third part in Eq. (5.6) is $exp\left(-\beta\int_0^1 \left\langle \frac{\partial\hat{V}(x,\alpha)}{\partial\alpha}\right\rangle_\alpha d\alpha\right)$. Here, the average $\langle\frac{\partial\hat{V}(x,\alpha)}{\partial\alpha}\rangle_\alpha$ does not contain any exponentials, and thus no terms that could blow-up and lead to noisy estimates and slow convergence.

We now need to pick up a switching scheme for $\hat{V}(x,\alpha)$, i.e. an interpolation scheme between $\hat{V}(x,0)$ and $\hat{V}(x,1)$. We picked the simplest scheme - a linear switching model - and found it to work very well:

$$\hat{V}(x,\alpha) = (1-\alpha)V(x) + \alpha V_0 \tag{5.7}$$

With this, Eq. (5.6) for the rate of escaping energy basins bounded by $V(x) < V_0$ becomes

$$rate = \lim_{w\to 0} \bar{v}\left\langle \frac{1\left(x\in S_w\right)}{w} e^{-\beta\left(\hat{V}(x,0)-\hat{V}(x,1)\right)}\right\rangle_1 \exp\left(\beta\int_0^1 \langle V(x)-V_0\rangle_\alpha d\alpha\right) \tag{5.8}$$

Thus to summarize till this point, to calculate Eq. (5.8):

- we first do a quick MC simulation using a flat potential to get the quantity $\lim_{w\to 0}\left\langle \frac{1(x\in S_w)}{w} e^{-\beta\left(\hat{V}(x,0)-\hat{V}(x,1)\right)}\right\rangle_1$, as shown in Figure 5.1.
- We then vary α adiabatically during the simulation, going from $\alpha = 0$ to $\alpha = 1$. We perform a series of MC simulations, with the Hamiltonian of the system

evolving as per Eq. (5.7) as the simulation time progresses.

A typical evaluation of Eq. (5.8) done as per this scheme is shown in Figure 5.2, where we show the change in the following two as a function of α:

(a) $\left(-\beta \int_0^1 \left\langle \frac{\partial \hat{V}(x,\alpha)}{\partial \alpha} \right\rangle_\alpha d\alpha\right)$, related to the 3rd part in Eq. (5.8), and

(b) the expected value of the time spent in the energy well **W**.

It may be useful to re-emphasize one point: The reason we do not immediately start MC as soon as $V(x)$ falls below V_0 is because the rate expression (Eq. (5.1)) is only valid conditional on the system being initialized at a Boltzmann-distributed random position within the well. If we start MC at the boundary of the well, this assumption is violated. Although it may seem that, by running MD within the well for some time before calculating the escape rate, we slightly overestimate the time spent in the well, this is not the case. The distribution of escape time from the well is independent of the time already spent in the well (since it follows an exponential distribution). Another way to see that there is no time over-counting is to observe that, during this MD trajectory in the well, there is also a small probability that the system escapes the well, so we are not artificially constraining the system to remain in the well for a longer time. The above scheme is a new, yet formally correct, way to deal with so-called re-crossing events that typically affect the accuracy of transition-theory based estimates of escape times [40, 46].

5.3.3 Simulation setup and compression testing

We first report the stress-strain plots for $\langle 001 \rangle$ compression of pristine cylindrical Au nanowires. The cylinder was initially carved out from perfect FCC lattice and before compression, it was 2.5nm in diameter and 7.5nm in height, comprising 2016 atoms (see Figure 5.3) with periodic boundary conditions imposed along all three directions. The cylinder axis z is also the compression axis $\langle 001 \rangle$. Thus all sites along the length of the wire are now equivalent sites for nucleation. For the other two directions, we do not strictly need periodic boundary conditions, but we nevertheless apply it for

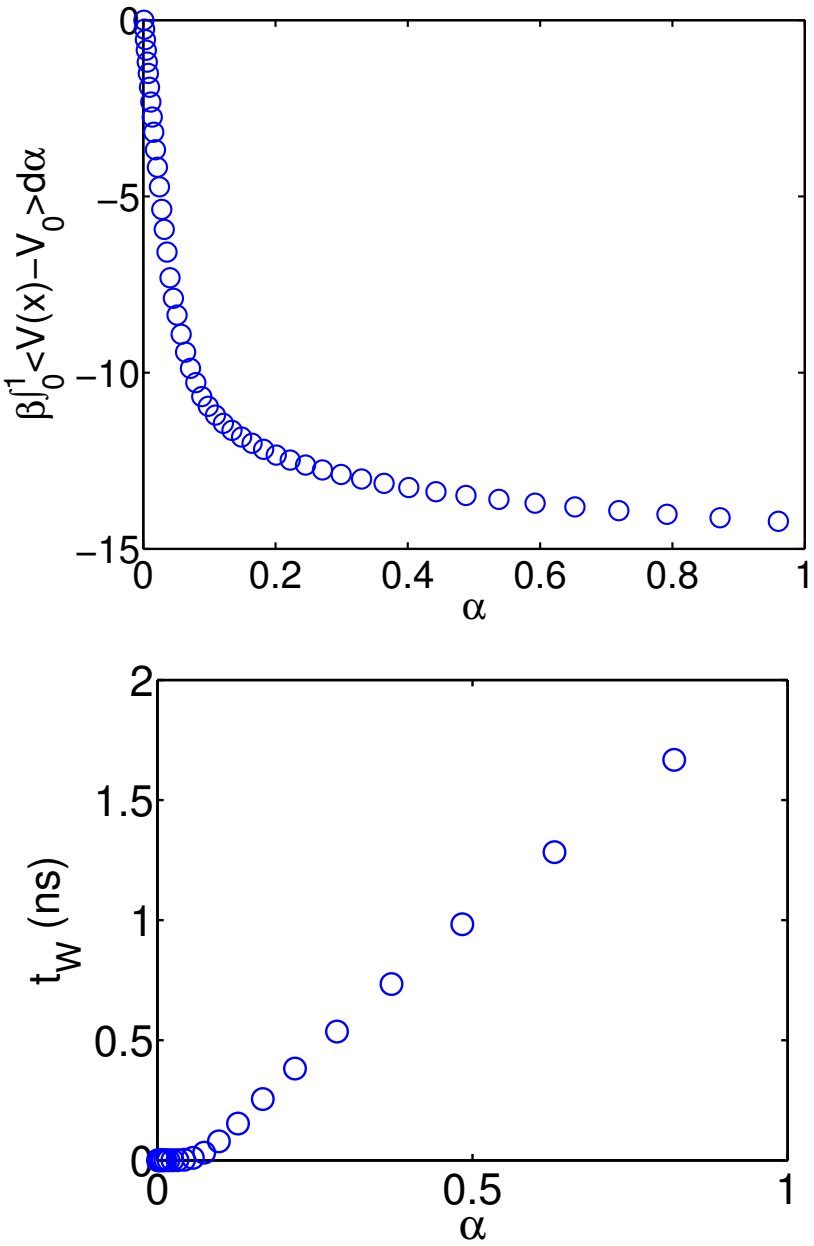

Figure 5.2: (a) Change in $\left(-\beta \int_0^1 \left\langle \frac{\partial \hat{V}(x,\alpha)}{\partial \alpha} \right\rangle_\alpha d\alpha\right)$ as a function of α as the simulation progresses (see Eq. (5.6)). (b) Expected value of the time spent in the energy well **W**. Calculations are for a Au nanowire with 2016 atoms, 2.5nm in diameter and 7.5nm in height, at 300 K.

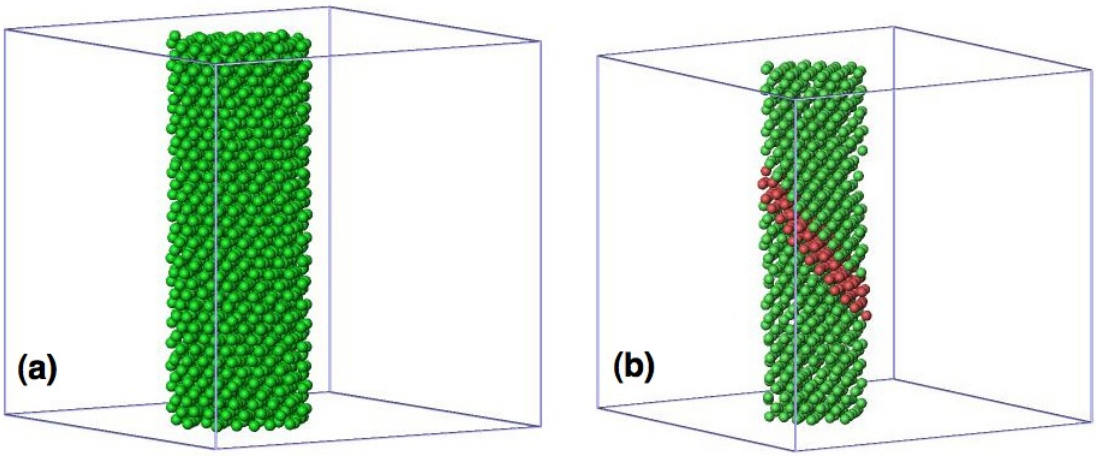

Figure 5.3: Perspective view of the nanopillar (a) before application of strain and (b) after application of strain when partial dislocation has nucleated. Coloring is as per Common Neighbor Analysis [123], where green denotes FCC, red denotes HCP. In (b), the surface atoms (identified as atoms that are neither FCC nor HCP) have been removed to bring the slip plane into clarity. Visualization was carried using the package OVITO [124].

computational ease. The dimensions of the supercell in the x and y directions are both around 75Å, which is much larger than the range of the EAM potential employed (5.5Å) [68]. As such there is no artifact from the pillar interacting with its images in these two directions. The cylinder was first equilibrated for 500 ps before beginning the compression, which was carried out by uniformly re-scaling the z-coordinates of all atoms. The atomic virial stress was used to obtain the Cauchy stress [69]. The stress at zero nominal strain is non-zero and tensile, and arises from the surface stress (see [69, 106] for a more detailed explanation). We adjust for this, and as such Figure 5.4 provides the stress span, i.e. the stress at a strain ϵ relative to the stress at 0 strain. We present the resulting stress(σ) versus nominal strain(ϵ) plots for 2 different strain rates $\dot{\epsilon}$: 5x10^7/sec, a strain rate value used in current day state-of-the-art MD simulations, and 10^3/sec. To the best of our knowledge, the latter is a strain rate several orders of magnitude slower than any reported calculation for a nanowire, and is a value that can actually be achieved in laboratory experiments on nanowires.

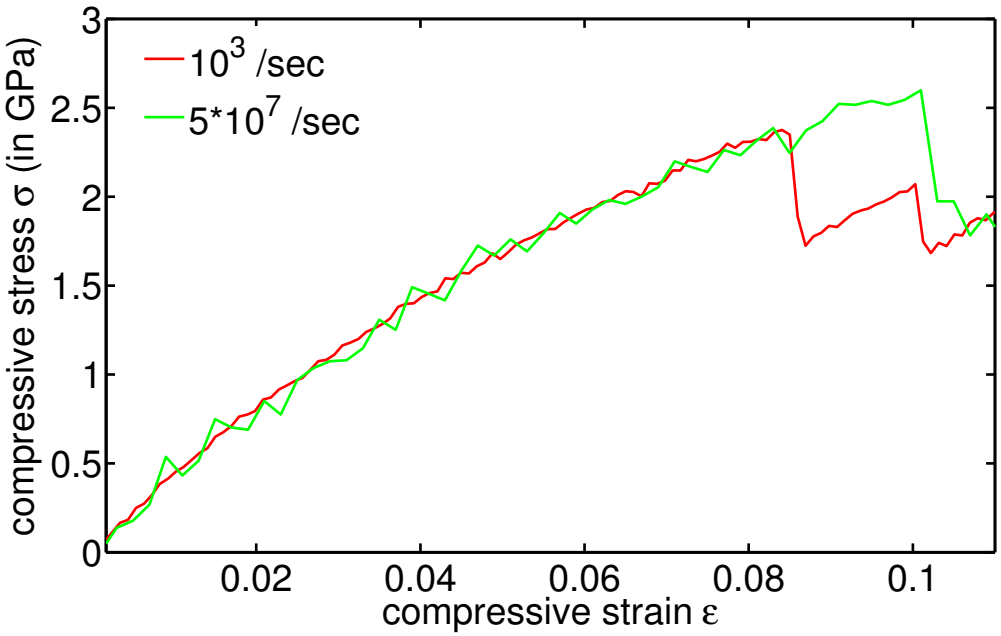

Figure 5.4: The stress versus nominal strain curve of Au nanowire under ⟨001⟩ compression (with inverted sign of stress). The data represents stress relative to surface stress at 0 strain as explained in text. The stress-strain plots are shown for two different strain rates. The green line denotes our calculations for a strain rate of $5\text{x}10^7$/sec, which is a commonly used strain rate in current-day MD. The red line shows our calculations for a strain rate of 10^3/sec.

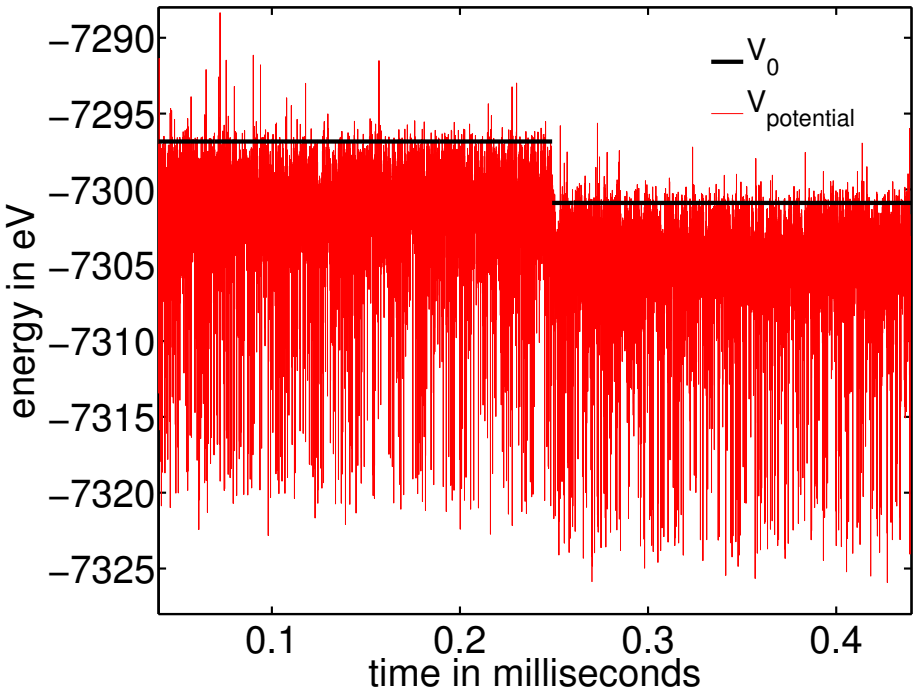

Figure 5.5: Typical variation of the energy lid V_0 (black line) and potential energy (red line) as a function of time. V_0 is adjusted as per the change in mean potential energy every few thousand MD steps. A sharp drop in the potential energy and accordingly in V_0 indicates that a nucleation event has occurred.

For the strain rate of $5x10^7$/sec, it was sufficient to perform ordinary NVT MD simulations using a time step of $2x10^{-15}$ sec and a Langevin thermostat with a coupling constant $1x10^{-11}$/sec. For the strain rate of 10^3/sec which can not be achieved through plain MD, we used our hybrid MC-MD algorithm as described in the preceding section and in [116]. The time-step and thermostat were same as for the strain rate of $5x10^7$/sec. All the calculations were performed on our in-house parallel MD package. Starting value of V_0 was picked such that it gave a rough $t_{\mathbf{W}}$ of around 1 nanosecond (see table 5.1). This was a value high enough for our current application. As the temperature/driving force (stress or strain) decrease, one would pick a higher V_0 that would accordingly lead to a larger $t_{\mathbf{W}}$. During compression as work is being performed on the system, there is a change in the potential energy, and as such the value of V_0 was updated every few thousand MD steps by an amount equaling the change in the mean potential energy over these many MD steps. A sharp drop in the potential energy indicates that a (partial) dislocation nucleation event has occurred in the system (see Figure 5.5). Table 5.1 provides values of the various parameters used in the compression testing experiment.

For both of these strain rates, the yielding is through slip and not twinning or elastic instabilities: a leading Shockley partial nucleates on a $\{111\}$ slip plane at lower stresses than a trailing partial. This can be seen in Figure 5.3(b) where the leading partial nucleated from the surface and left behind a 2-layer thick HCP region. The trailing and leading partials are in agreement with what one expects by calculating relative Schmid factors: for $\langle 001 \rangle$ compression, $(a/6)[11\bar{2}]$ and $(a/6)[\bar{2}11]$ were found to be the leading and trailing partials corresponding to Schmid factors of 0.47 and 0.24 respectively [106].

Figure 5.4 brings out the perils of using unrealistic strain-rate MD calculations as a tool for insight and discovery. We find that though the failure mechanism stays same for both the strain-rates, there is a significant difference in the strain at which slip occurs. At the high strain-rate of $5x10^7$/sec, the wire withstands strain of as high

Table 5.1: Starting value of V_0 and eventually expected value of $t_{\mathbf{W}}$, for unstrained samples at various temperatures. For strained samples, the change in potential energy during the process of straining was calculated, and V_0 was changed by this amount. For the temperatures between 350K to 425 K, ordinary MD was sufficient for the stress range considered in this work and hence the parameters below are only for temperatures till 325 K.

T(K)	V_0 (eV)	$t_{\mathbf{W}}$ (ps)
275	-7275.00	1400
300	-7267.75	1700
325	-7260.25	30

as almost 10% before the first partial dislocation is emitted (corresponding to a stress span of around 2.6 GPa). However at the more realistic strain rate of 10^3/sec, the partial is emitted around 8.6% only (corresponding to a stress span of around 2.35 GPa). For both the strain-rates, there is a distribution of the strain at which slip occurs and the values in 5.3) denote mean values.

This strong difference is in accordance with the strain-rate sensitivity in true nanowires (i.e. wires less than 100nm in diameter) as predicted by [65] and observed in real experiments on small nanowires by [64]. To understand and motivate this dependence, we look at the rate of nucleation of leading partial dislocation, as given by Eq. (5.9) below [65]:

$$R = N\nu(\epsilon).exp(\frac{-F(\epsilon,T)}{k_BT}) \tag{5.9}$$

Here F is the Helmholtz free energy of activation as a function of temperature T and strain ϵ (since our experimental setup is a constant strain situation), k_BT is the thermal energy, N is the number of equivalent surface nucleation sites and $\nu(\epsilon)$ is an athermal strain-dependent attempt frequency. Eq. (5.9) thus has two contributions: An athermal part related to the elastic limit (which we defined as stress for nucleation of the first dislocation) of the surface at which nucleation would occur spontaneously without any thermal contributions, and an activated part that takes into account the role of thermal fluctuations in causing nucleation to happen even below the athermal

strain (which is the minimum strain at which nucleation would occur at absolute zero temperature).

5.3.4 Activation parameters

5.3.4.1 Activation volume

The activation volume Ω is defined as the derivative of the activation free energy with respect to stress, i.e. $\Omega(\sigma, T) \equiv -(\frac{\partial F}{\partial \sigma})_T$. As reported through experimental measurements as well as TST based calculations, the activation volume for surface nucleation remains in a characteristic range of few b^3 (where b is the burgers vector). In comparison, for a typical bulk dislocation source the activation volume is upwards of $100b^3$ and can be as high as $1000b^3$ [64]. The activation volume in turn determines whether a process will be strain-rate sensitive or insensitive. This can be reasoned as follows. Assuming a simple case where the activation energy depends linearly on stress (see [65] for detailed derivation), one can show that the most probable estimate of the nucleation stress is given by

$$\sigma = \sigma_{athermal} - \frac{k_B T}{\Omega} ln \frac{k_B T N \nu}{E \dot{\epsilon} \Omega} \tag{5.10}$$

where E is the Young's modulus and $\sigma_{athermal}$ is the athermal nucleation stress causing instantaneous dislocation nucleation. As can be seen in Eq. (5.10), a high activation volume (as in the case of bulk dislocation source) masks out the effect of strain-rate. As the activation volume decreases towards values relevant for surface nucleation, the effect of strain rate should become very significant. Figure 5.4 provides the first direct MD based evidence of this.

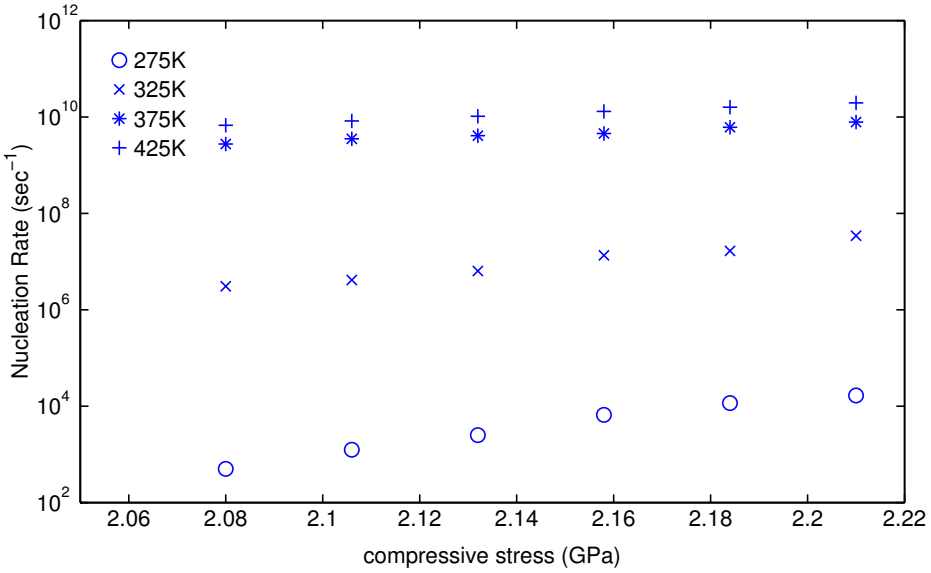

Figure 5.6: Strain and temperature dependence of the dislocation nucleation rate $R(\epsilon, T)$, converted here to $R(\sigma, T)$ by assuming a linear dependence of stress on strain. Each data point was calculated by averaging over 16 samples. The size of the individual markers corresponds to the 90% confidence interval in the measurement.

5.3.4.2 Activation free energy

We now report detailed calculations of the activation terms in Eq. (5.9). To do so, we performed the compression testing at a strain-rate of 10^3/sec at 7 different temperatures from 275 K to 425 K at intervals of 25 K. These compression tests were stopped at various values of the nominal strain from 8% to 8.5% (the athermal strain at 0 Kelvin for nanowire of these dimensions was found to be around 13.5%). The wisdom behind choosing this particular range of strain will be clear soon when we provide estimates of the nucleation rate. For each of these strains, the wire is still in the elastic regime. As described in the introduction, we are interested in collecting statistics of the waiting time before nucleation of the first dislocation as the nanowire is held at this strain [118, 119]. The structures from the compression tests stopped at varying strains served as samples for our waiting time statistics tests.

For each of these structures (corresponding to a combination of imposed strain

and temperature), 16 different runs were carried out where the nanowire was held at a particular strain and temperature. Each of the runs was carried out until nucleation of the first dislocation, marked by appearance of a 2-layer thick HCP region, as well as sudden dips in the potential energy and the stress (see Figure 5.5). The average rate of nucleation was then calculated as

$$R(\epsilon, T) = \frac{1}{\tau_{average}} \tag{5.11}$$

where $\tau_{average}$ is the time for nucleation averaged over the 16 samples.

Figure 5.6 provides the value for nucleation rate for various strain and temperature combinations. In this figure we have converted strain to stress by assuming a roughly constant Young's Modulus of around 26 GPa as we obtained in Figure 5.4 for $\langle 001 \rangle$ compression of gold nanowire, in order to facilitate comparison with published literature, even though in Figure 5.4 we see a softening in the tangent modulus as the strain increases. This plot clarifies our choice of imposed strains - with 8% strain (or 2.08 GPa stress), the nucleation rate is already slower than one every few milliseconds at 275K. The other end of 8.5% was picked because as illustrated in Figure 5.4, the wire slips at high temperatures around 8.6%. The lengthiest of these calculations took around a few CPU days. With a slightly more aggressive choice of V_0, it should be possible to reach the one per second or still slower regime.

For each strain ϵ, we picked a sufficiently high value of reference temperature T_0 such that the rate $\mathrm{R}(\epsilon, T_0)$ did not any longer depend on the choice of temperature. We can then make the approximation that $F(\epsilon, T) \gg F(\epsilon, T_0)$, and express Eq. (5.9) as Eq. (5.12) below, to factor out the athermal frequency term. Given this approximation, the entropy of activation we calculate subsequently is effectively measured relative to the high-temperature limit (since the activation entropy at high temperature could still be nonzero).

$$F(\epsilon, T) \approx -k_B T ln(\frac{R(\epsilon, T)}{R(\epsilon, T_0)}) \tag{5.12}$$

From Eq. (5.12) we directly calculate the Activation free energy F(ϵ, T) (Figure 5.7). Our values are in the rough benchmark of the 0.3 eV value found in Copper nano-indentation experiments where one expects homogeneous nucleation to be the mechanism at work [89]. Figure 5.7 also provides the only published values of activation free energy at 0 Kelvin temperature for Au nanowires [106]. Ref. [106]'s calculations are for a 5nm diameter nanowire (thus 4 times as many atoms as in our nanowire) using a chain of states methodology at 0 Kelvin. A comparison between our and their free energies is thus not really justified due to differing system sizes - this can be understood by looking at Eq. (5.10). In a larger sample the number of nucleation sites (surface atoms) N is higher. As such the nucleation stress goes down, increasing the probability of nucleation for the same driving force (stress/strain and temperature). This in turn leads to a lower free energy of activation. Some qualitative differences between these two calculations may will also arise because of difference in interatomic potentials. Even though a direct comparison between Ref. [106]'s and our results is not justified due to these reasons, we still provide their results in Figure 5.7) since viewed together our results give a full picture of how the activation free energy varies with stress, temperature and specimen size.

Our calculations demonstrate how strongly and rather nonlinearly the free energy of activation depends on the temperature. It has been a common practice, mostly arising from lack of methods capable of providing high temperature activation energy barriers calculations, to assume the same temperature dependence for activation free energy across temperatures. Many workers have found direct and indirect evidence suggesting this is incorrect for studying deformation in materials. For example, Ref. [117] reported that in Al, a temperature dependent activation barrier can lead to a transition from twinning to full dislocation emission back to twinning with increasing temperature. We believe our algorithm should now provide researchers with a tool to

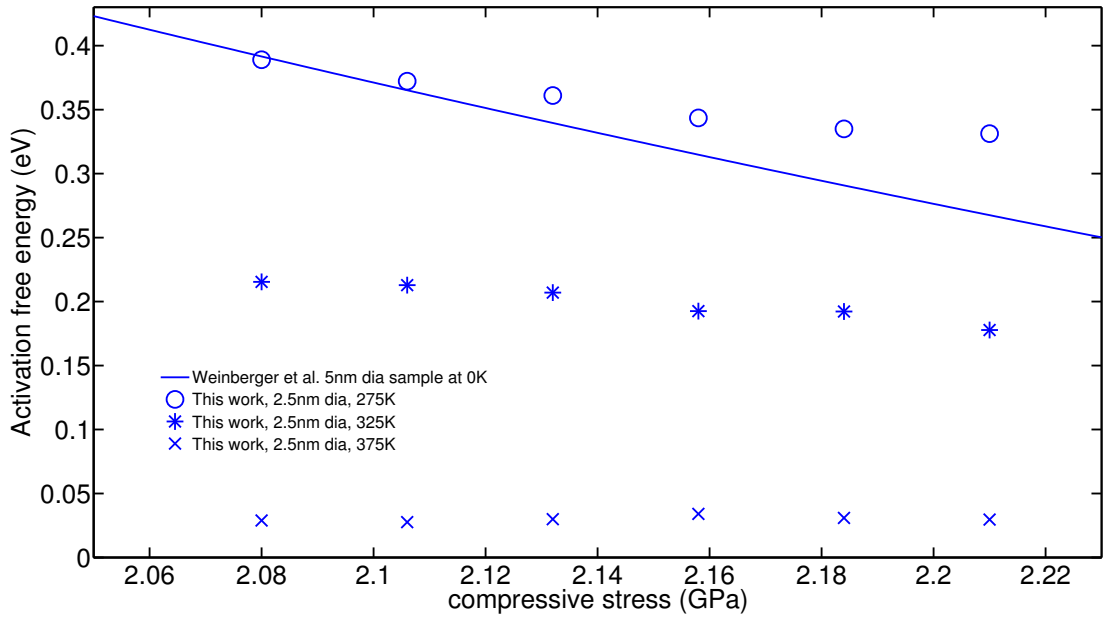

Figure 5.7: Activation free energy for surface nucleation of dislocations as a function of stress and temperature. Comparisons are made with results from literature for 0 Kelvin activation energy for a wire 8 times bigger (thus with many more possible nucleation sites). The size of the individual markers corresponds to the 90% confidence interval in the measurement.

calculate such barriers at various temperatures under realistic loading rates for the first time.

5.3.4.3 Activation entropy

From the variation of activation free energy with stress and temperature in Figure 5.7, we calculated the stress dependent activation entropy. To obtain this quantity, we do a linear fit between the activation energy and the temperature at each stress value. The entropy is then the slope of this linear fit (with a negative sign), reported in Figure 5.8. Such a calculation has rarely been performed for dislocation nucleation or for other problems - the two instances of such calculations we could find were Ref. [115]'s recent adaptive strain-boost hyperdynamics (ASBHD) where the authors calculate the stress dependent entropy for corner nucleation in Copper nanowires, and Ref. [87]'s Umbrella Sampling based calculations (in Copper as well). We find that the entropy decreases as the driving force (stress or strain) increases, and is typically in the range 20-30k_B. This is roughly in the benchmark of values reported through previous simulations. We avoid making detailed comparisons here between our values and these previously published values, given that we differ in elements (gold versus copper), geometries (circular versus square with sharp cross-sections), size and ensemble (constant stress versus constant strain, see Ref. [87]).

5.4 Discussion

5.4.1 Key results

5.4.1.1 Tensile tests

Our compressive tests on Au nanopillars show that the mechanism of deformation stays same for strain rates from $10^8/s$ to $10^2/s$, i.e., slip through nucleation of a leading Shockley partial dislocation on a {111} slip plane. However, the elastic limit (defined as stress for nucleation of the first dislocation) changes significantly as the strain-rate is changed. This is in qualitative agreement with the strain-rate depen-

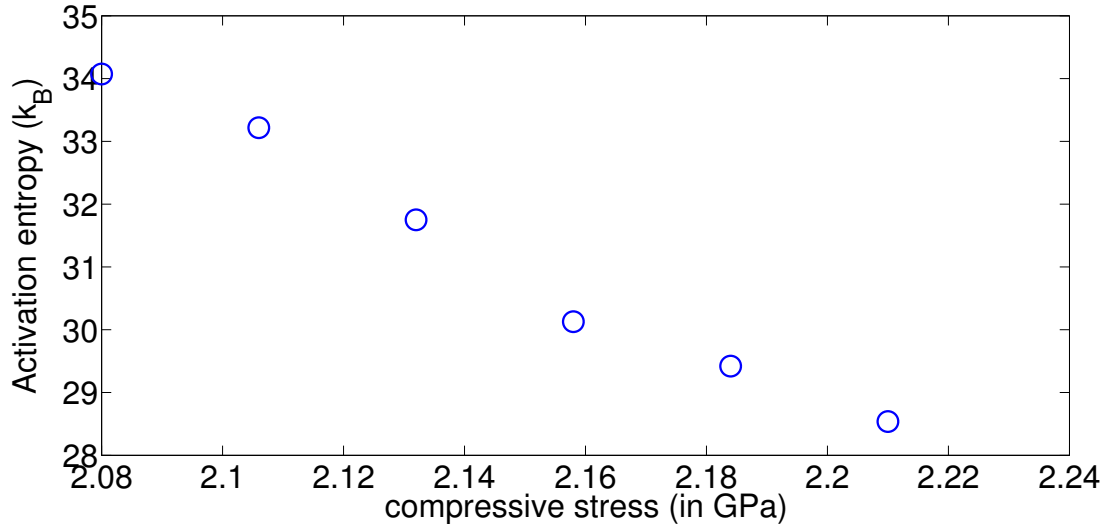

Figure 5.8: Activation entropy as a function of stress for surface nucleation of dislocations.

dence in nanopillars as observed in experiments [64] and also predicted by the phenomenological models of [65]. We believe ours is the first fully atomistic calculation reported across 6 orders of magnitudes in the strain-rate and reaching a realistic strain rate of $10^2/s$.

5.4.1.2 Activation entropy and free energy

The origin of activation entropy in dislocation nucleation, and related to it the rapid drop of activation free energy with temperature, can be attributed to thermal expansion in the material [87]. As the temperature increases the expansion causes atoms to move away from each other making it easier for planes to shear and thus reducing the free energy barrier for nucleation. Our high activation entropy values show that not considering the temperature dependence of the activation energy can lead to nucleation rate being erroneous by as much as 8-12 orders of magnitude. This has been emphasized in the very recent literature by [87]. We also found that the entropy decreases as the driving force for nucleation (stress or strain) increases, leading to a significant and nonlinear dependence of the activation free energy on driving force

and temperature. Our method now provides an easy-to-implement way to calculate this dependence under realistic driving forces for any general sample geometry.

5.4.2 Comparison of our algorithm with other algorithms for extended time-scales

It is also instructive to compare our algorithm with other realistic time-scale algorithms for studying dislocation nucleation. Two algorithms that have been recently used to model temperature-dependence of the dislocation nucleation process include the Umbrella Sampling method (proposed in Ref. [87]) and the Adaptive Strain Boost Hyperdynamics (ASBHD) method (proposed in Ref. [115]). Both are excellent methods, but have their respective limitations. The former needs to define an order parameter (or a reaction coordinate) for the system, in terms of which the biasing potential is then imposed on a certain sub-set of atoms. Picking such an order parameter might be a non-trivial task in complicated sample geometries and can have its pitfalls [55]. Also, while this method is excellent for computing free energy barriers - it does not perform any actual dynamics. ASBHD does away with the need to pick up an order parameter. However the speed-up in ASBHD relative to ordinary MD becomes significant (i.e. 4-5 orders of magnitude or more) only as the temperature of the system falls below 100K or so. The method is a local boost scheme, thus specific atoms are lifted out of the low-lying energy basins, making them preferential sites for nucleation to happen. Such a local boost scheme works well for specific geometries (such as a square nano-rod with sharp corners), but might not be very well suited for studying more homogeneous nucleation as we considered in the current chapter. Since our method does not require the specification of the degrees of freedom of interest (which is crucial when the mechanisms are complex and involve the movement of many atoms), it is well suited for studying homogeneous nucleation.

By providing a time-scale correction independent to the main simulation, our

algorithm also provides the ability to implement time-dependent boundary conditions (relevant to a tensile test for e.g.) and in general time-dependent forces. To do this, we can launch a set of adiabatic switching jobs prior to the main simulation, that give a good starting value for the quantity $t_{\mathbf{W}}$ and thus for the boosted time-scale. This is to be contrasted with ASBHD [115] and Hyperdynamics methods in general [41] where time-scale estimates remain noisy and non-converged for long simulation times, especially as one tries to increase the speed-up relative to ordinary MD [59, 116].

5.5 Conclusions

In this and the previous chapters we have derived and demonstrated a hybrid MC-MD algorithm that can be used to achieve realistic time-scales in fully atomistic simulations of materials while still predicting correct deformation physics. The algorithm is especially designed to be suited for massive parallelization. By using this algorithm, we obtained compression testing stress-strain plots at strain rates several orders of magnitude lower than ever previously reported for MD simulations. We showed that high strain-rates in simulations, which have been common due to lack of methods capable of implementing low strain-rates, can lead to a significant error in the elastic limit of the material. We also derived the full stress and temperature dependence of the activation free energy for surface nucleation of dislocations in gold nanowires. The algorithm was described in sufficient detail to be useful to the mechanics community for different applications.

Chapter 6

Vacancy diffusion in tantalum

6.1 Introduction

This chapter builds up ground for future work involving multiple vacancies and their collective dynamics in BCC tantalum metal, under conditions of strain and temperature. As these vacancies diffuse through the lattice, they agglomerate to form voids, which can continue to grow and eventually result in fracture. Often the time-scales for such migration processes are in the seconds to still longer time regime, thus prohibiting the direct application of MD simulations. The traditional approach of dealing with such problems involves severe approximations such as harmonic transition state theory (HTST), which, as we showed in the case of surface nucleation of dislocations in the previous chapter, can be rather misleading.

In this chapter, we also scrutinize the robustness of our algorithm with respect to the **only free parameter** in it: The energy lid V_0 which denotes the exit point of the thermalization Monte Carlo (see Figure 4.4 in Chapter 4). Vacancy diffusion in tantalum is has a relatively low barrier (around 1eV as per experiments [125]). One would thus expect this to be a source of error in several current day accelerated dynamics algorithms. We demonstrate that our algorithm as proposed in this thesis performs well even for such a (relatively) low barrier. The algorithm has other internal parameters too, however they are well-determined as explained in the previous chapters and do not require tinkering with on part of the algorithm's user.

We calculate the diffusion rate for vacancy diffusion in tantalum for different values of the parameter V_0 at different temperatures, and it is verified that the diffusion constant is rather insensitive to the exact choice of V_0, thereby minimizing the need for *clever* human intervention in getting the algorithm to work.

We study as a starting point the case of 1 vacancy in a periodic supercell. We calculate the diffusion rates for this using

- brute-force MD at high temperatures (upwards of 1500K)
- Zero temperature saddle point search calculations combined with HTST. This is the standard way to access diffusion rates when the time-scales are excruciatingly slow for fully atomistic MD simulations
- the accelerated dynamics approach proposed in this thesis which allows us to reach milliseconds or longer for few thousand atoms

We compare the 3 sets of calculations with each other, and critically ascertain the applicability and performance of HTST across the temperatures.

6.2 Harmonic transition state theory for vacancy migration

6.2.1 Migration energy and pathway calculation

According to TST (not necessarily harmonic TST), the rate constant for escape from a state A is given by Equation 6.1 [56]

$$\nu = \frac{1}{2}\langle \delta(x-q)|\dot{x}|\rangle_A \tag{6.1}$$

Here x is the reaction coordinate, $x = q$ gives the location of the TST dividing surface bounding state A, and $\dot{x}$ is the time-derivative of x. If one assumes that the

potential energies near the energy basin minima and near the saddle point are well described by a harmonic (i.e. second order) expansion of the energy, then the TST rate as in the above equation becomes the flux through the saddle plane and is given by

$$\nu = \nu_o \exp\left(\frac{-E}{k_B T}\right) \tag{6.2}$$

where E is the energy barrier associated with the process, T is the temperature and ν_o is the frequency prefactor. For vacancy migration, the energy barrier is the barrier associated with the motion of a vacancy from one lattice site to the next. This can be computed, at 0K, using a variety of methods to determine saddle points in N dimensional space including the nudged elastic band [16] and the string method [126].

For the problem of vacancy migration in tantalum, as modeled with the Ackland-Thetford-Finnis-Sinclair (ATFS) potential [127], the vacancy formation energy and migration are shown in Figure 6.1 as a function of the number of atoms as calculated using the software package LAMMPS. From this figure, we can see that the vacancy formation energy and migration energy are converged within reasonable values at ~ 250 atoms. This gives numerically a vacancy formation energy of 2.91 eV and a migration energy of 1.13 eV, in fair agreement with experimental measurements [125].

The number of atoms is critical because it determines if ν_o can easily be evaluated using harmonic transition state theory. Using N dimensional harmonic transition state theory, the frequency prefactor ν_o can be determined by analyzing the modes of the equilibrium and transition state as:

$$\nu_o = \frac{\Pi_{i=1}^{N} \nu_i^{ES}}{\Pi_{i=1}^{N-1} \nu_i^{TS}} \tag{6.3}$$

where ν_i^{ES} denotes the frequencies of the system in the equilibrium state and ν_i^{TS} represent the frequencies in the transition state. The reduced product over the tran-

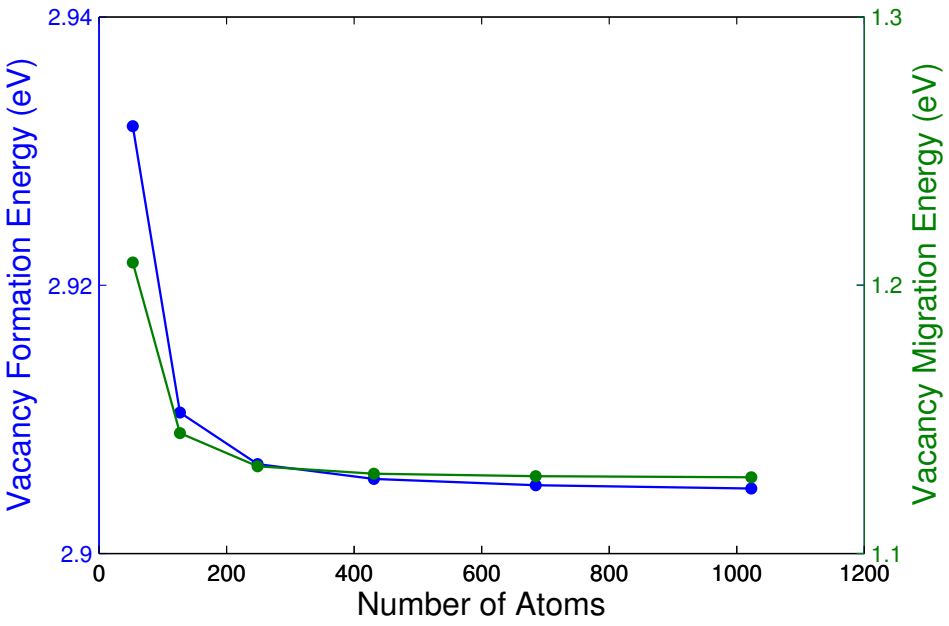

Figure 6.1: The vacancy formation energy and migration energy as a function of the number of atoms in the system.

sition state effectively removes the lowest frequency (theoretically zero or negative) of the transition state.

For the migration of vacancies as modeled by the ATFS potential, the migration barrier has a unusual shape as shown in Figure 6.2. This transition state pathway shows a very shallow minima midway through the energy pathway. To evaluate ν_o, we take the transition state as the local maxima. It is worth noting that, however, the prefactor determined in this way is not particularly sensitive to the exact location of the maxima as using a nearby state produced similar results to within 5%.

To determine the frequency prefactor ν_o, all the frequencies are determined for both the equilibrium and transition state, latter being as identified in the saddle state search. This is done by computing the Hessian matrix of each system of atoms.

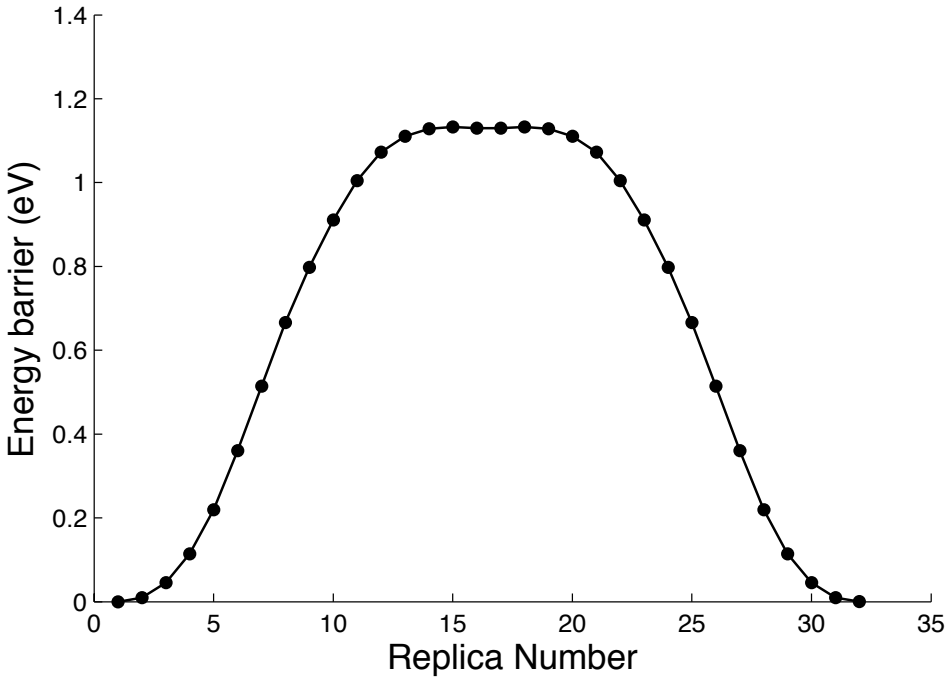

Figure 6.2: The vacancy migration energy as a function of the replica number for tantalum as modeled by the ATFS potential.

The Hessian matrix is a tangent stiffness matrix, i.e.

$$H_{ij} = \frac{\partial V}{\partial x_i \partial x_j} \tag{6.4}$$

where i and j run over all the degrees of freedom of the system, which is $3 \times n$ where n is the number of atoms and V is the potential energy of the system. The frequencies are computed from solving the eigenvalue problem associated with the free vibration of the system. This means the square of the frequencies of the system can be determined from the eigenvalues of the system

$$(\mathbf{H} - m\mathbf{I}) \cdot \mathbf{v} = 0 \tag{6.5}$$

where m are the atomic masses and I is the $N \times N$ identity matrix. However, for the free vibration problem, one will always end up with the lowest three modes, which correspond to rigid body translation, having zero frequency and must be automati-

cally removed. The frequencies needed, ν_i, can be determined from the eigenvalues of the above eigenvalue problem, λ_i, according to:

$$\nu_i = \frac{1}{2\pi}\sqrt{\lambda_i} \tag{6.6}$$

where the factor 2π converts from rad/s to Hz (cycles per second). Practically speaking, the Hessian matrix is determined from numerical differentiation of the potential energy of the system in which each atom is displaced a very small amount from its current position in all three directions. For the vacancy migration problem in Ta using the ATFS potential, we thus find that the frequency $\nu_o = 5.25 \times 10^9$ Hz.

6.2.2 Diffusion constant from HTST

Now that we have calculated all the coefficients in Equation 6.2 (i.e. the frequency prefactor and the energy barrier), we can derive an expression for the temperature dependent diffusion constant for vacancy diffusion in BCC materials (see *Kinetics of Materials* by Balluffi, Allen and Carter, section 8.2 for related discussion). In general the diffusion constant is given by Equation (6.7) below:

$$D = \frac{\mathrm{T}\langle r^2 \rangle}{6} \tag{6.7}$$

where the jump rate T equals 8ν, since each vacancy is surrounded by 8 neighboring atoms in BCC lattice. ν is the temperature dependent jump frequency we obtained in previous section. r is the jump distance and is half the body-diagonal in BCC unit cell. We thus have $\langle r^2 \rangle = 3a^2/4$, a being the lattice parameter. With this we finally obtain

$$D = \nu a^2 = \nu_0 a^2 exp^{-\frac{E}{k_B T}} \tag{6.8}$$

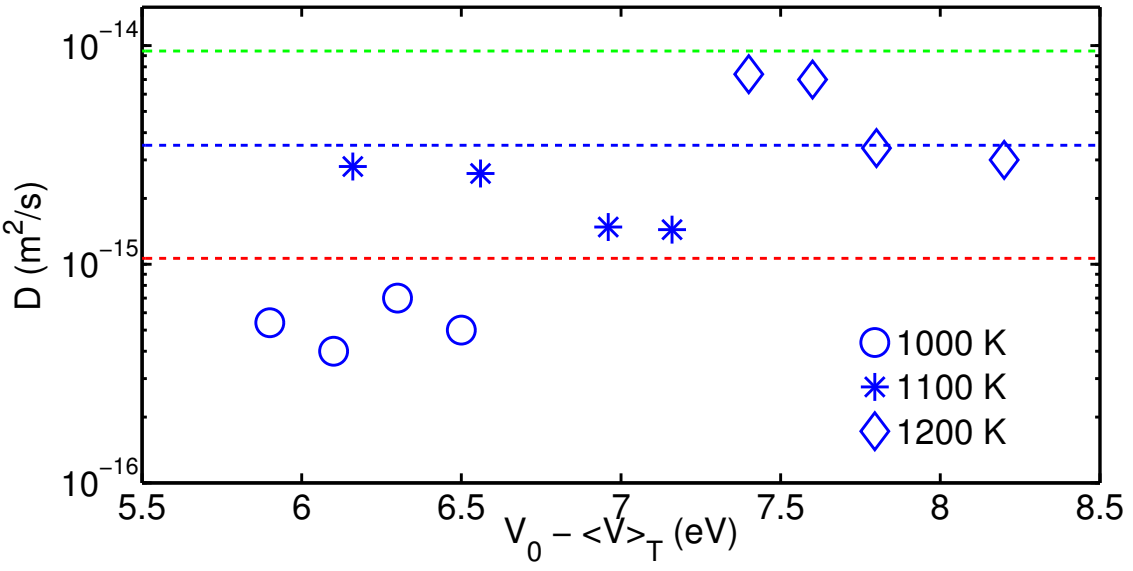

Figure 6.3: Testing robustness of the algorithm with respect to choice of V_0. $< V >_T$ denotes the mean potential energy at the particular temperature. As V_0 is varied by an eV, the diffusivity stays well within an order of magnitude. The effect of V_0 also seems to decrease with decrease in temperature. The red, blue and green lines denote respectively the diffusion constants as per HTST at 1000, 1100 and 1200 Kelvins.

6.3 Diffusion constant using our accelerated dynamics algorithm

6.3.1 Choice of the parameter V_0

In order to use the accelerated dynamics algorithm proposed in this thesis, the only free parameter that needs to be fixed is the value of the energy lid V_0 that decides the switching of the algorithm between MC and MD (see Figure 4.4).

For high speed-ups, we would ideally seek a high V_0. But that can lead to incorrect transition rates, as often we will end up missing low-lying saddle points. A low V_0 would exponentially decrease the speed-up that we gain. Another problem that could arise from low V_0 is that the rate of escape from states bounded by V_0 would be so fast, as to break down the rare event hypothesis that is one of the central tenets of our algorithm.

Before proceeding with detailed calculations of diffusion constant at various temperatures, we first check at different temperatures as to how sensitive is our algorithm to the exact choice of V_0. 249 Ta atoms (1 vacancy in a 5x5x5 supercell) were considered, interacting through the ATFS potential [127] in a NVT (constant number, volume and temperature) ensemble. Langevin thermostat was used here as well, similar to the case of iron in Chapter 4. Fully periodic boundary conditions were used. At 1000,1100 and 1200 Kelvins, we performed the simulation at 4 V_0 values each within a range of more than 1 eV variation. Figure 6.3 illustrates that the algorithm is fairly robust with respect to the choice of V_0. As V_0 is varied by as much as an eV, it can be seen that the diffusivity remains well within a fraction of an order of magnitude error. The speed-up in simulation time with relative to ordinary MD is between 5 to 3 orders of magnitude as the parameter V_0 is changed. As V_0 value is further reduced, the simulation needs to be run for much longer time to get a converged diffusion constant, since the speed-up decreases exponentially with decrease in V_0. From this figure it also appears that the robustness further improves with decrease in temperature (the scatter at 1000K is less than the other two temperatures).

This thus proves that our algorithm can obtain several orders of magnitude speed-up in simulation while still maintaining a time-scale that is accurate well within an order of magnitude.

6.3.2 Diffusion constants and critical comparison with HTST values

We now provide in Figure 6.4 the diffusion constants using (a) our accelerated algorithm, (b) brute-force MD at high temperatures, and (c) HTST across the temperatures. The activation energies through atomistic simulation and HTST are 1.30 (+/- 0.07) eV and 1.13 eV respectively, which are fairly close to each other. We now do a critical analysis of the differences between HTST diffusion constants and those

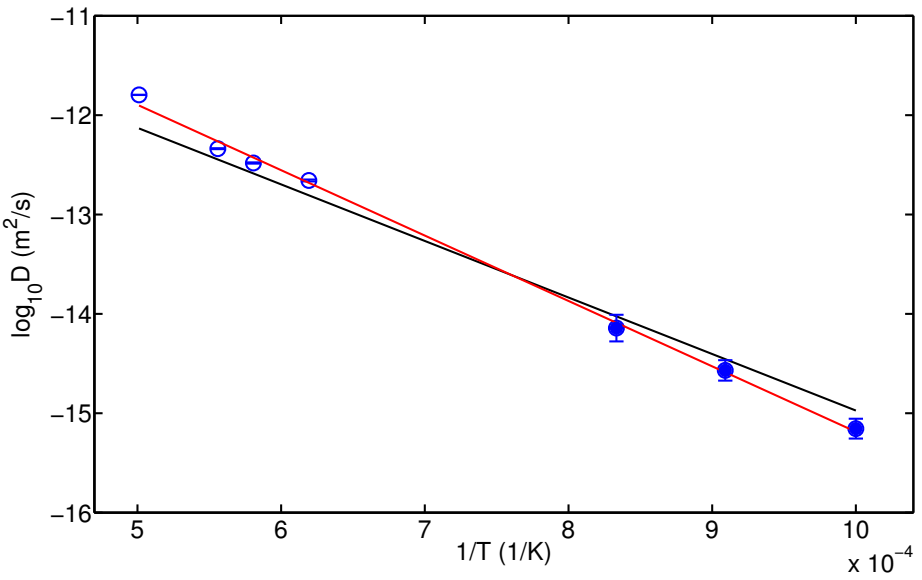

Figure 6.4: Diffusion constant versus inverse temperature using (a) brute force MD (open circles), (b) accelerated dynamics (filled circles), (c) HTST (black line). The red line denotes a best fit using Equation 6.2 to the joint MD and accelerated MD data. 95% confidence interval in the data points is illustrated.

through actual dynamics.

A key assumption in TST or HTST is the existence of a critical transition surface between two neighboring energy minima (called the *reactant* and the *product*), such that if this surface is crossed, transition from *reactant* to *product* always occurs. TST does not account for cases in which an atom that has crossed the surface from the *reactant* side, might come back to the *reactant* state instead of going to *product* state. As per this reasoning, TST would overestimate the actual rate. Given the shallow nature of the saddle surface as we show in Figure 6.2, an atom could jump back and forth quite a few times before actually making a transition, while TST would recognize each of these jumps as a separate transition, and thus TST diffusion constant would be larger than the actual diffusion constant. This is indeed the case at lower temperatures as can be seen in Figure 6.4, where the TST diffusion constant (black line) is roughly larger than the (best-fit) diffusion constant from actual dynamics (red line).

But however, we also find, as shown in Figure 6.4, that at higher temperatures the TST diffusion constant is slightly LOWER than the actual diffusion constant (i.e. measured through dynamics). To explain this, we have to take into account an additional competing effect. At higher temperatures, bounce back recrossings are not the only factor corrupting the TST values. There is an additional assumption of TST that now gets violated: As per TST, no two transitions (i.e. not just recrossings but actual transitions) are correlated. Correlated here means that the second transition happens before the system has lost memory of the first transition. As the temperature increases, the probability of two successive and correlated vacancy hops increases. This in turn affects the diffusion constant. At higher temperatures, a particle that has just hopped can have enough excess energy to make another quick hop before it settles down. Since there is no scope for such correlated jumps happening in TST per formulation, the slope of the TST Arrhenius plot stays less steep than that for the actual dynamics at higher temperatures. Figure 6.5 follows the averaged squared displacement in the system as a function of time at 1800 K, and one can clearly see such correlated hops happening.

6.4 Outlook

In this chapter we have demonstrated the applicability of our algorithm to study vacancy diffusion in BCC tantalum. We are currently looking at the problem of more than 1 vacancy in the system, as to how they interact, what are their migration pathways, and eventually what is the vacancy clustering kinetics. We are studying all these as a function of imposed strain and temperature. Many very interesting questions can be asked here. To give an example, it would be useful and interesting to check if the vacancy clustering follows an Ostwald ripening mechanism, wherein large clusters grow at the expense of smaller ones. Due to the time-scale problem, these questions have not yet seen any atomistic simulations being applied under realistic driving forces.

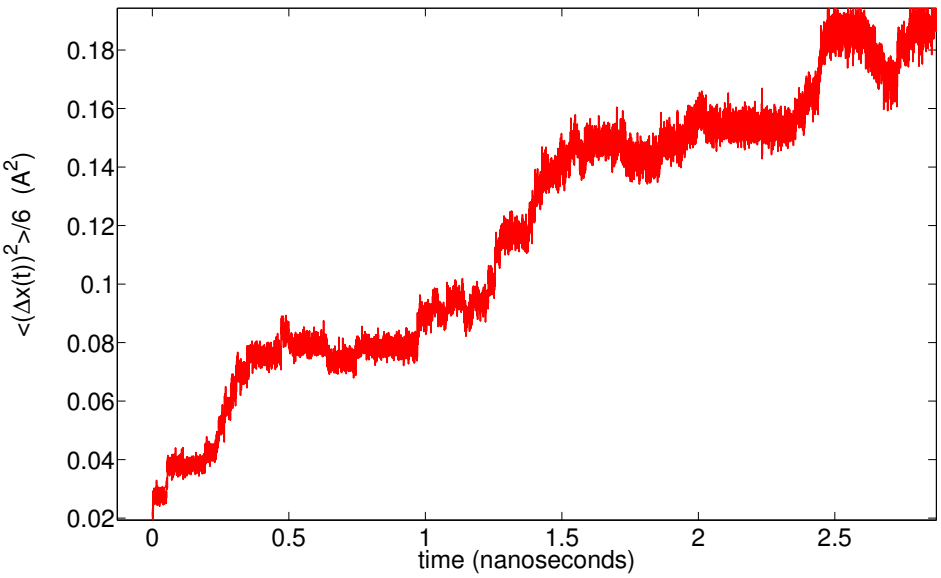

Figure 6.5: The averaged squared displacement (averaged over particles but not over time) in 5x5x5 supercell of tantalum with 1 vacancy at 1800 K. One can clearly see several vacancy hops that are separated only by a few picoseconds.

We also used 0 temperature saddle point calculations combined with HTST to calculate diffusion constants - a common strategy to model such problems. Such a saddle point approach is simple and elegant, but only when it works. It requires one to have an estimate for the initial and final configurations. Guessing the final configuration can be extremely non-trivial and misleading in complicated microstructures involving multiple vacancies, dislocations or grain boundaries. Also, similar to how HTST was found inaccurate at higher temperatures, one would expect it to be inaccurate when the strain is higher (since strain and temperature both are basically driving forces).

In contrast to HTST, one would expect our algorithm to only improve in performance as the mechanism involved become more concerted (i.e. involving not just one atom) and arise from the intrinsic anharmonicity of the potential energy surface, thus further restricting the notion of a saddle surface.

Chapter 7

Retrospect and prospects

In this thesis we looked at two crucial aspects of atomistic simulations - interatomic potentials and the time-scale problem. For both we proposed techniques that we believe extend the capabilities of current day simulations. All algorithms were well validated and applied to different materials specific problems of current interest: Mixed oxide nuclear fuels, vacancy diffusion at low temperatures in iron and tantalum, and realistic strain-rate simulations of dislocation nucleation in nanopillars.

7.1 Interatomic potentials

In Chapters 2 and 3, we developed a methodology for generating interatomic potentials that is appropriate for all interatomic separations and energy scales. The potential we have focused on in this thesis, the nuclear fuel system (U,Pu,Np)O_2, is just one example of a model material in which very relevant materials physics depends on accurate and reliable interactions over many orders of magnitude, and we have obtained the first complete description that allows for direct simulations of damage cascades due to high-energy radiation effects. The potential has been generated based on a slight revision of the ZBL universal potential to account for ionic materials with the intermediate interatomic distances fitted to a broad database of *ab initio* structural energies and available experimental data. Transferability of the potential was also checked by applying it to structures, compositions and configurations not included in the fitting. In view of these qualities, we expect it to be a very reliable

potential for studying displacement cascades in (U,Pu,Np)O_2. A natural extension of this work now involves including other minor actinides and fission products in the fitting database, so that potentials for a yet more general system can be developed. The potentials from this thesis are now being used by several groups across the world [128–130].

7.2 Algorithm for realistic time-scales

We developed and validated a hybrid stochastic and deterministic approach that allows us to achieve practical time-scales for at least several thousand atoms. The method that we develop is inherently parallel in nature, and is very well suited for use on massively parallel super computers.

The accuracy of the method for more than several thousand atoms is yet to be verified - however we must point out that the system sizes we have are already superior to what most or all accelerated dynamics methods can deal with without being overly inaccurate. Also, the algorithm in this thesis can be expected to perform very well irrespective of system size for mechanisms that involve not just one atom. This can be reasoned as follows. As the system size N increases, the probability (per unit time) of a rare event roughly gets multiplied by N. So what is a rare event in a small system eventually becomes a common event in a big system. The only way to keep the event probability constant with increasing system size is to start focusing on rarer events (e.g. multiple nearly simultaneous jumps). By focusing on multiple simultaneous jumps as the rare events, the algorithm identifies more important and more irreversible events, as system size grows. To put this another way, expect our algorithm to be *specifically* suited for predicting long-time scale dynamics of mechanisms involving concerted motions of several atoms.

We demonstrated that the algorithm is robust with respect to choice of the only free parameter and that the boosted time-scale is correct. While the algorithm can

achieve milliseconds and longer, it also has the resolution to capture fast and concerted events (like surface nucleation of a leading Shockley partial) that take less than picoseconds to happen.

To the best of our knowledge, this thesis and the related publications are the first to report molecular dynamics simulations of tensile testing at 100/s strain rate - a rate which laboratories can actually achieve. In a related problem, we also looked at the activation parameters for surface nucleation of dislocations. We found very high values of the activation entropy here, which shows that the traditional approach, wherein 0 temperature activation energies are assumed at all temperatures, can be very incorrect.

7.3 Future work

In future work, we are applying the accelerated dynamics algorithm to explore deformation mechanisms in BCC nanopillars. The specific question we are trying to answer is if the strain-rate influences a transition in deformation mechanism from deformation twinning to slip.

The last chapter of this thesis also lays the foundation for work on vacancy agglomeration in BCC tantalum. Through this we eventually want to understand the kinetics of vacancy clustering under varied temperature and strain, and what role do vacancies play in failure of these metals.

An open-source software named SISYPHUS (Stochastic Iterations to Stimulate Yield of Path Hopping over Upper States), implementing the ideas detailed in this thesis will be released shortly and made available for use by everyone (expected July 2012).

Bibliography

[1] L. Van Brutzel, A. Chartier, and J.-P. Crocombette. *Phys. Rev. B*, 78:024111, 2008.

[2] J. F. Ziegler, J. P. Biersack, and U. Littmark. Pergamon, New York, 1985.

[3] N. D. Morelon, D. Ghaleb, J.-M. Delaye, and L. Van Brutzel. *Phil. Mag.*, 83:1533, 2003.

[4] H. Y. Geng, Y. Chen, Y. Kaneta, M. Iwasawa, T. Ohnuma, and M. Kinoshita. *Phys. Rev. B*, 77:104120, 2008.

[5] K. Govers, S. Lemehov, M. Hou, and M. Verwerft. *Journal of Nuclear Materials*, 366:161 – 177, 2007.

[6] K. Govers, S. Lemehov, M. Hou, and M. Verwerft. *Journal of Nuclear Materials*, 376:66 – 77, 2008.

[7] J.C. Slater. *Phys. Rev.*, 42:33, 1932.

[8] R. Laskowski, G. K. H. Madsen, P. Blaha, and K. Schwarz. *Phys. Rev. B*, 69:140408, Apr 2004.

[9] K. T. Moore and G. van der Laan. *Rev. Mod. Phys.*, 81:235–298, Feb 2009.

[10] H. Y. Geng, Y. Chen, Y. Kaneta, and M. Kinoshita. *Phys. Rev. B*, 75:054111, Apr 2007.

[11] K. Ikushima, S. Tsutsui, Y. Haga, H. Yasuoka, R. E. Walstedt, N. M. Masaki, A. Nakamura, S. Nasu, and Y. Ōnuki. *Phys. Rev. B*, 63:104404, Feb 2001.

[12] G. Kresse and J. Furthmüller. *Phys. Rev. B*, 54:11169–11186, Oct 1996.

[13] V. I. Anisimov, J. Zaanen, and O. K. Andersen. *Phys. Rev. B*, 44:943–954, Jul 1991.

[14] S. L. Dudarev, G. A. Botton, S. Y. Savrasov, C. J. Humphreys, and A. P. Sutton. *Phys. Rev. B*, 57:1505–1509, Jan 1998.

[15] S. L. Dudarev, G. A. Botton, S. Y. Savrasov, Z. Szotek, W. M. Temmerman, and A. P. Sutton. *Phys. Stat. Sol. A*, 166:429, Jan 1999.

[16] G. Henkelman, B. P. Uberuaga, and H. Jonsson. *The Journal of Chemical Physics*, 113:9901–9904, 2000.

[17] H. Matzke. *J. Chem. Soc. Faraday Trans.*, 83:1121, 1987.

[18] J.K. Fink. *Journal of Nuclear Materials*, 279:1 – 18, 2000.

[19] J. A. Nelder and R. Mead. *The Comp. Jour.*, 7:308, 1965.

[20] J. D. Gale. *J. Chem, Soc., Trans.*, 93:629, 1997.

[21] T. Karakasidis and P. J. D. Lindan. *Journal of Physics: Condensed Matter*, 6:2965, 1994.

[22] P. Sindzingre and M. J. Gillan. *Journal of Physics C: Solid State Physics*, 21:4017, 1988.

[23] R. Devanathan, L. Van Brutzel, A. Chartier, C. Gueneau, A. Mattson, V. Tikare, T. Bartel, T. Besmann, M. Stan, and P. Van Uffelen. *Energy Environ. Sci.*, 3:1406–1426, 2010.

[24] P. Tiwary, A. van de Walle, and N. Grønbech-Jensen. *Phys. Rev. B*, 80:174302, Nov 2009.

[25] K. Kurosaki, K. Yamada, M. Uno, S. Yamanaka, K. Yamamoto, and T. Namekawa. *Journal of Nuclear Materials*, 294:160 – 167, 2001.

[26] T. Arima, S. Yamasaki, Y. Inagaki, and K. Idemitsu. *Journal of Alloys and Compounds*, 400:43 – 50, 2005.

[27] K. Kurosaki, M. Imamura, I. Sato, T. Namekawa, M. Uno, and S. Yamanaka. *Journal of Alloys and Compounds*, 387:9 – 14, 2005.

[28] A. van de Walle and G. Ceder. *Journal of Phase Equilibria*, 23:348, Nov 2002.

[29] D. A. Andersson, J. Lezama, B. P. Uberuaga, C. Deo, and S. D. Conradson. *Phys. Rev. B*, 79:024110, Jan 2009.

[30] R. Devanathan, J. Yu, and W. J. Weber. *The Journal of Chemical Physics*, 130:174502, 2009.

[31] T. Yamashita, N. Nitani, T. Tsuji, and H. Inagaki. *Journal of Nuclear Materials*, 245:72 – 78, 1997.

[32] A. van de Walle and G. Ceder. *Rev. Mod. Phys.*, 74:11–45, Jan 2002.

[33] N. L. Allan, T. H. K. Barron, and J. A. O. Bruno. *The Journal of Chemical Physics*, 105:8300–8303, 1996.

[34] A. Chartier, L. Van Brutzel, and M. Freyss. *Phys. Rev. B*, 81:174111, May 2010.

[35] H. Serizawa, , Y. Arai, , and K. Nakajima. *The Journal of Chemical Thermodynamics*, 33:615 – 628, 2001.

[36] S. J. Zhou, D. L. Preston, P. S. Lomdahl, and D. M. Beazley. *Science*, 279:1525–1527, 1998.

[37] M. Karplus and G. A. Petsko. *Nature*, 347:631–639, 1990.

[38] S. Piana and A. Laio. *J. Phys. Chem. B*, 111:4553, 2007.

[39] T. T. Lau, A. Kushima, and S. Yip. *Phys. Rev. Lett.*, 104:175501, Apr 2010.

[40] A. F. Voter, F Montalenti, and T. C. Germann. *Ann. Rev. Mater. Res.*, 32:321–346, 2002.

[41] A. F. Voter. *Phys. Rev. Lett.*, 78:3908–3911, May 1997.

[42] A Laio and M Parrinello. *Proc. Natl. Acad Sci*, 99:12562, 2002.

[43] G. T. Barkema and Normand Mousseau. *Phys. Rev. Lett.*, 77:4358–4361, Nov 1996.

[44] A. F. Voter. *Phys. Rev. B*, 57:R13985–R13988, Jun 1998.

[45] M. R. Sorensen and A. F. Voter. *The Journal of Chemical Physics*, 112:9599–9606, 2000.

[46] C.-Y. Lu, D. E. Makarov, and G. Henkelman. *The Journal of Chemical Physics*, 133:201101, 2010.

[47] D. Hamelberg, J. Mongan, and J. Andrew McCammon. *J. Chem. Phys.*, 120:11919–11929, 2004.

[48] K. E. Becker, M. H. Mignogna, and K. A. Fichthorn. *Phys. Rev. Lett.*, 102:046101, Jan 2009.

[49] S. Hara and J. Li. *Phys. Rev. B*, 82:184114, Nov 2010.

[50] K. A. Fichthorn, R. A. Miron, Y. Wang, and Y. Tiwary. *J. Phys:Condens. Matter*, 21:084212, 2009.

[51] K. E. Becker, M. H. Mignogna, and K. A. Fichthorn. *Phys. Rev. Lett.*, 102:046101, Jan 2009.

[52] R. A. Miron and K. A. Fichthorn. *J. Chem. Phy.*, 119:6210, 2003.

[53] G. Henkelman and H. Jonsson. *The Journal of Chemical Physics*, 115:9657–9666, 2001.

[54] A. Kushima, X. Lin, J. Li, J. Eapen, J. C. Mauro, X. Qian, P. Diep, and S. Yip. *The Journal of Chemical Physics*, 130:224504, 2009.

[55] B. M. Dickson, D. E. Makarov, and G. Henkelman. *The Journal of Chemical Physics*, 131:074108, 2009.

[56] A. F. Voter and J. D. Doll. *J. Chem. Phy.*, 80:5832, 1984.

[57] H. Grubmüller. *Phys. Rev. E*, 52:2893–2906, Sep 1995.

[58] M. M. Steiner, P.-A. Genilloud, and J. W. Wilkins. *Phys. Rev. B*, 57:10236–10239, May 1998.

[59] R. A. Miron and K. A. Fichthorn. *Journal of Chemical Physics*, 119:6210, 2003.

[60] M. I. Mendelev and Y. Mishin. *Phys. Rev. B*, 80:144111, Oct 2009.

[61] M. Lubbehusen and H. Mehrer. *Acta Metall. Mater.*, 38:283, 1990.

[62] H. Zheng, A. Cao, C. R. Weinberger, J. Y. Huang, K. Du, J. Wang, Y. Ma, Y. Xia, and S. X. Mao. *Nature Communications*, 1:144, 2010.

[63] A.T. Jennings, M.J. Burek, and J.R. Greer. *Phys. Rev. Lett.*, 104:135503, 2010.

[64] A. T. Jennings, J. Li, and J. R. Greer. *Acta Materialia*, 59:5627 – 5637, 2011.

[65] T. Zhu, J. Li, A. Samanta, A. Leach, and K. Gall. *Phys. Rev. Lett.*, 100:025502, 2008.

[66] P. J. Steinhardt, D. R. Nelson, and M. Ronchetti. *Phys. Rev. B*, 28:784–805, Jul 1983.

[67] J. Li. *Modelling and Simulation in Materials Science and Engineering*, 11:173, 2003.

[68] G. Grochola, S. P. Russo, and I. K. Snook. *The Journal of Chemical Physics*, 123:204719, 2005.

[69] E. Rabkin, H.-S. Nam, and D.J. Srolovitz. *Acta Materialia*, 55:2085 – 2099, 2007.

[70] M. D. Uchic, D. M. Dimiduk, J. N. Florando, and W. D. Nix. *Science*, 305:986–989, 2004.

[71] B. Wu, A. Heidelberg, and J. J. Boland. *Nature Materials*, 7:525–529, 2005.

[72] J.R. Greer, W.C. Oliver, and W.D. Nix. *Acta Materialia*, 53:1821 – 1830, 2005.

[73] J. R. Greer, D. Jang, J.-Y. Kim, and M. J. Burek. *Advanced Functional Materials*, 19:2880–2886, 2009.

[74] C. A. Volkert and E. T. Lilleodden. *Philosophical Magazine*, 86:5567–5579, 2006.

[75] Z. W. Shan, R.K. Mishra, S. A. Syed A., O. L. Warren, and A. M. Minor. *Nature materials*, 7:115–119, 2007.

[76] X. Li, Y. Wei, L. Lu, K. Lu, and H. Gao. *Nature*, 464.

[77] J.R. Greer and W.D. Nix. *Phys. Rev. B*, 73:245410, 2006.

[78] W D. Nix, J R. Greer, G Feng, and E T. Lilleodden. *Thin Solid Films*, 515:3152 – 3157, 2007.

[79] T. Zhu and J. Li. *Progress in Materials Science*, 55:710 – 757, 2010.

[80] C. Weinberger and W. Cai. *Journal of Materials Chemistry*, 22:3277–3292, 2012.

[81] V. Bulatov, F. F. Abraham, L. Kubin, B. Devincre, and S. Yip. *Nature*, 391:669 – 672, 1997.

[82] J. Marian, W. Cai, and V. V. Bulatov. *Nature*, 3:158 – 163, 1997.

[83] J. Moriarty, V. Vitek, V. Bulatov, and S. Yip. *Journal of Computer-Aided Materials Design*, 9:99–132, 2002.

[84] J. Li, K. J. Van Vliet, T. Zhu, S. Yip, and S. Suresh. *Nature*, 418:307, 2002.

[85] F. F. Abraham, R. Walkup, H. Gao, M. Duchaineau, T. Diaz De La Rubia, and M. Seager. *Proceedings of the National Academy of Sciences*, 99:5783–5787, 2002.

[86] A. J. Cao, Y. G. Wei, and S. X. Mao. *Applied Physics Letters*, 90:151909, 2007.

[87] S. Ryu, K. Kang, and W. Cai. *Proceedings of the National Academy of Sciences*, 108:5174, 2011.

[88] U. Landman, W. D. Luedtke, N. A. Burnham, and R. J. Colton. *Science*, 248:454–461, 1990.

[89] C. A. Schuh, J. K. Mason, and A. C. Lund. *Nature Materials*, 4:617, 2005.

[90] C. A. Schuh. *Materials Today*, 9:32 – 40, 2006.

[91] D. Jang and J. R. Greer. *Nature Materials*, 9, 2010.

[92] K. J. Van Vliet, J. Li, T. Zhu, S. Yip, and S. Suresh. *Phys. Rev. B*, 67:104105, 2003.

[93] M. Zhao, W. S. Slaughter, M. Li, and S. X. Mao. *Acta Materialia*, 51:4461 – 4469, 2003.

[94] J. R. Greer, C. R. Weinberger, and W. Cai. *Materials Science and Engineering: A*, 493:21 – 25, 2008.

[95] T. A. Arias and J. D. Joannopoulos. *Phys. Rev. Lett.*, 73:680–683, 1994.

[96] P. K. Sitch, R. Jones, S. Öberg, and M. I. Heggie. *Phys. Rev. B*, 52:4951–4955, 1995.

[97] C. Woodward and S. I. Rao. *Phys. Rev. Lett.*, 88:216402, 2002.

[98] C. Woodward, D. R. Trinkle, L. G. Hector, and D. L. Olmsted. *Phys. Rev. Lett.*, 100:045507, 2008.

[99] E. A. Carter. *Science*, 321:800–803, 2008.

[100] M. Fago, R. L. Hayes, E. A. Carter, and M. Ortiz. *Phys. Rev. B*, 70:100102, 2004.

[101] V. Gavini, K. Bhattacharya, and M. Ortiz. *Journal of the Mechanics and Physics of Solids*, 55:697 – 718, 2007.

[102] V. Gavini, J. Knap, K. Bhattacharya, and M. Ortiz. *Journal of the Mechanics and Physics of Solids*, 55:669 – 696, 2007.

[103] D. R. Trinkle. *Phys. Rev. B*, 78:014110, 2008.

[104] J.P. Hirthe and J. Lothe. 1982.

[105] W. Cai, A. Arsenlis, C. R. Weinberger, and V. V. Bulatov. *Journal of the Mechanics and Physics of Solids*, 54:561 – 587, 2006.

[106] C. R. Weinberger, A. T. Jennings, K. Kang, and J. R. Greer. *Journal of the Mechanics and Physics of Solids*, 60:84 – 103, 2012.

[107] S. J. Zhou, D. L. Preston, P. S. Lomdahl, and D. M. Beazley. *Science*, 279:1525–1527, 1998.

[108] J. Chang, W. Cai, V. V. Bulatov, and S. Yip. *Computational Materials Science*, 23:111 – 115, 2002.

[109] J. Diao, K. Gall, M. L. Dunn, and J. A. Zimmerman. *Acta Materialia*, 54:643 – 653, 2006.

[110] H. S. Park, K. Gall, and J. A. Zimmerman. *Journal of the Mechanics and Physics of Solids*, 54:1862 – 1881, 2006.

[111] S. M. Foiles, M. I. Baskes, and M. S. Daw. *Phys. Rev. B*, 33:7983–7991, 1986.

[112] J. F. Justo, M. Z. Bazant, E. Kaxiras, V. V. Bulatov, and S. Yip. *Phys. Rev. B*, 58:2539–2550, 1998.

[113] A. Kushima, J. Eapen, J. Li, S. Yip, and T. Zhu. *The European Physical Journal B - Condensed Matter and Complex Systems*, 82:271–293, 2011.

[114] J. Li, S. Sarkar, W. T. Cox, T. J. Lenosky, E. Bitzek, and Y. Wang. *Phys. Rev. B*, 84:054103, Aug 2011.

[115] S. Hara and J. Li. *Phys. Rev. B*, 82:184114, 2010.

[116] P. Tiwary and A. van de Walle. *Phys. Rev. B*, 84:100301, 2011.

[117] D.H. Warner and W.A. Curtin. *Acta Materialia*, 57:4267 – 4277, 2009.

[118] L. Zuo, A. H. W. Ngan, and G. P. Zheng. *Phys. Rev. Lett.*, 94:095501, 2005.

[119] L. Zuo and A. H. W. Ngan. *Philosophical Magazine Letters*, 86:355–365, 2006.

[120] J. K. Mason, A. C. Lund, and C. A. Schuh. *Phys. Rev. B*, 73:054102, 2006.

[121] J. Cai and Y. Y. Ye. *Phys. Rev. B*, 54:8398–8410, 1996.

[122] H. S. Park and J. A. Zimmerman. *Phys. Rev. B*, 72:054106, Aug 2005.

[123] J. D. Honeycutt and H C. Andersen. *The Journal of Physical Chemistry*, 91:4950–4963, 1987.

[124] A. Stukowski. *Modelling and Simulation in Materials Science and Engineering*, 18:015012, 2010.

[125] H.-E. Schaefer. *physica status solidi (a)*, 102:47–65, 1987.

[126] E. Weinan, W. Ren, and E. Vanden-Eijnden. *Phys. Rev. B*, 66:052301, Aug 2002.

[127] G. J. Ackland and R. Thetford. *Philosophical Magazine A*, 56:15–30, 1987.

[128] A.E. Thompson and C. Wolverton. *Phys. Rev. B*, 84:134111, Oct 2011.

[129] S.I. Potashnikov, A.S. Boyarchenkov, K.A. Nekrasov, and A.Ya. Kupryazhkin. *Journal of Nuclear Materials*, 419:217 – 225, 2011.

[130] A. Chernatynskiy, C. Flint, S. Sinnott, and S. Phillpot. *Journal of Materials Science*, 84:1–10, 2011.